

# POLITECNICO DI TORINO

Master's Degree in Aerospace Engineering



**Politecnico  
di Torino**

Master's Degree Thesis

## Precise orbit determination techniques for a lunar satellite navigation system

Academic Supervisor:  
**Prof. Fabio DAVIS**

Candidate:  
**Enrico Edoardo Zini**

Company Tutor:  
**Cosimo Stallo**

Company Advisor:  
**Carmino Di Lauro**

Company Advisor:  
**Nicola Angelo Rana**

**A.Y. 2020/2021**



## Abstract

The next global strategic priority in space missions is a stable access to the Moon. Over the last few years several studies and discoveries have pushed the space agencies and companies worldwide to numerous feasibility studies to realize permanent infrastructures and assets in cis-lunar environment and on its surface.

NASA's Artemis program to take humans back to the Moon in this decade is a huge driving force in the generation of an economically sustainable path for lunar exploration and resource exploitation, aiming to create a reference point to reach furthest celestial bodies of high interest like Mars.

In this framework, Thales Alenia Space is conducting the feasibility study of the Lunar Communications and Navigation Services (LCNS) within European Space Agency's (ESA) Moonlight initiative that will support Artemis space program.

The aim of the work presented in this dissertation is to implement a precise Orbit Determination (OD) algorithm to dynamically estimate the state vector of a constellation of satellites that could provide a navigation service in lunar environment. Different scenarios and phases of ESA's Positioning Navigation and Timing (PNT) implementation roadmap were simulated. A key point in the analysis is the interaction between the disparate observables that can be collected in each scenario, ranging from satellite-to-satellite cross-link signals and Deep Space Network(DSN) tracking to altimetric measures and Doppler-based range-rates. A trade-off analysis based on the increasing complexity of the proposed architectures and the respective quality of the OD algorithm was then performed.

The implementation of the algorithm and the performance evaluation has been fully carried out in MATLAB environment, while the satellites orbits and Moon's and Earth's infrastructures needed to generate the observables have been simulated with both Systems Tool Kit (STK) and MATLAB High Precision Orbit Propagator(HPOP).



# Acknowledgements

I would like to thank my company tutor and supervisors Cosimo Stallo, Carmine Di Lauro and Nicola Angelo Rana for their extensive help in the development of this vast work. In spite of the distance imposed by the restrictions of this challenging year, I cannot imagine a better support. I am very grateful as well to Thales' engineers Massimo Eleuteri and Mattia Carosi for their presence, assistance and encouragement during this extraordinary experience in Thales.

I wish to thank my academic supervisor from Politecnico di Torino, prof. Fabio Dosis, for making himself available and to oversee the thesis development with constant pieces of advice.

I will always be grateful to my family and friends for all these years of shared efforts and successes. None of this would be possible without all of you.

*“You are here to enrich the world, and you impoverish yourself if you forget the errand”*

*Woodrow Wilson*



# Table of Contents

<b>List of Tables</b>	VII
<b>List of Figures</b>	VIII
<b>Acronyms</b>	XII
<b>1 Introduction</b>	<b>1</b>
1.1 The Moon exploration . . . . .	2
1.2 The Artemis Program . . . . .	4
1.3 ESA Moonlight and the LCNS . . . . .	6
1.3.1 The PNT roadmap . . . . .	6
1.3.2 The Elliptical Lunar Frozen Orbits (ELFO) . . . . .	8
1.4 Present work purpose and outline . . . . .	9
<b>2 Orbit determination techniques</b>	<b>11</b>
2.1 A brief history . . . . .	12
2.2 Tracking systems . . . . .	13
2.3 Orbit determination algorithms . . . . .	14
2.3.1 Batched Least Squares algorithm . . . . .	16
2.3.2 Sequential estimation: the Kalman Filter . . . . .	17
2.4 The Observables . . . . .	18
2.4.1 Range . . . . .	19
2.4.2 Range-Rate . . . . .	20
2.4.3 Altimetric measurements . . . . .	20
2.4.4 Angles . . . . .	20
2.5 Observability . . . . .	22
2.6 The time synchronization problem . . . . .	22
2.7 Other tracking error sources . . . . .	24

<b>3</b>	<b>Case study: orbit determination of a lunar satellite navigation system constellation</b>	<b>25</b>
3.1	Satellite constellation . . . . .	26
3.2	Reference frame . . . . .	27
3.3	The dynamical model . . . . .	28
3.3.1	Keplerian 2 Bodies . . . . .	29
3.3.2	Real perturbed motion . . . . .	29
3.3.3	The integration method . . . . .	30
3.4	The observables . . . . .	31
3.4.1	DSN ranging . . . . .	31
3.4.2	GNSS signals . . . . .	34
3.4.3	On-board altimeter measurements . . . . .	35
3.4.4	ISL measurements . . . . .	35
3.4.5	Lunar surface beacons ranging . . . . .	37
3.4.6	Data rate . . . . .	37
3.4.7	Simulation of measurement noise . . . . .	38
3.5	The implemented BLS orbit determination algorithm . . . . .	39
3.6	The instantaneous least squares solution . . . . .	42
3.7	Errors calculation . . . . .	43
<b>4</b>	<b>Simulations results</b>	<b>45</b>
4.1	DSN-only tracking . . . . .	45
4.1.1	8-hours-a-week tracking . . . . .	46
4.1.2	4-hours-a-day tracking . . . . .	47
4.2	DSN and altimeter . . . . .	49
4.2.1	8-hours-a-week-tracking . . . . .	49
4.2.2	4-hours-a-day-tracking . . . . .	50
4.3	Lunar beacons, ISL and altimeter . . . . .	51
4.3.1	Preliminary simulations: insight into observability and noise with mixed algorithm . . . . .	51
4.3.2	Two Beacons, ISL and Altimeter . . . . .	58
4.3.3	Three Beacons, ISL and Altimeter . . . . .	67
4.4	Lunar beacons, DSN, ISL and Altimeter . . . . .	74
4.5	The use of GNSS . . . . .	82
4.5.1	GNSS and altimeter . . . . .	82
4.5.2	GNSS, DSN and Altimeter . . . . .	87
<b>5</b>	<b>Trade-off analysis</b>	<b>92</b>
5.1	DSN tracking . . . . .	93
5.2	The autonomous lunar navigation system . . . . .	94
5.3	About the use of GNSS . . . . .	96

<b>6 Summary and conclusions</b>	97
6.1 Future work and recommendations . . . . .	97
<b>A Software tools</b>	100
A.1 STK . . . . .	100
A.2 MATLAB . . . . .	101
<b>B The State Transition Matrix</b>	103
B.1 Analytical solution for the perturbed case . . . . .	103
<b>Bibliography</b>	106

# List of Tables

3.1	ELFOs keplerian elements . . . . .	27
3.2	Simulated DSN antennas sites specifications . . . . .	32
3.3	Optimized beacons' positions simulated . . . . .	37
4.1	3D position and velocity errors resume for the DSN-only scenario .	48
4.2	3D position and velocity errors resume for the DSN and altimeter scenario . . . . .	51
4.3	3D position and velocity errors comparison for different data rates for the scenario with 2 beacons, ISL and altimeter . . . . .	59
4.4	3D position and velocity errors comparison for different time spans for the scenario with 2 beacons, ISL and altimeter with perturbed ELFOs (HPOP) . . . . .	62
4.5	3D position and velocity errors comparison for different time spans and dynamical models for the scenario with 3 beacons, ISL and altimeter . . . . .	68
4.6	3D position and velocity errors comparison for different time spans and data rates for the scenario with 3 beacons, ISL, DSN and altimeter . . . . .	77
4.7	3D position and velocity errors comparison for different time spans and data rates for the scenario with 3 beacons, ISL, DSN and altimeter . . . . .	78
4.8	3D position and velocity errors for different time spans for the perturbed scenario with 3 beacons, ISL, DSN and altimeter . . . .	81
4.9	3D position and velocity errors comparison for different time spans and noise levels for the Keplerian scenario with the GNSS and altimeter. Data rate is set at 1 batch of observables per minute. . .	83
4.10	3D position and velocity errors comparison for Keplerian and per- turbed scenarios with GNSS, DSN and altimeter. Data rate is set at 1 batch of observables per minute. . . . .	91

# List of Figures

1.1	Global exploration roadmap [1]	2
1.2	Artemis roadmap to 2024 [17]	5
1.3	ESA PNT implementation roadmap	7
1.4	Orbital Elements of a simulated ELFO from [20]	8
1.5	LCNS third phase conceptual constellation from [23]	9
2.1	Estimated, reference (nominal) and true trajectory during OD process	12
2.2	VLBI principle	21
3.1	Simulated ELFOs at the initial epoch of the simulations	27
3.2	Moon Inertial Reference frame at simulation start epoch	28
3.3	Perturbed ELFOs simulated for 10 days	30
3.4	Satellite-to-Satellite LOS visibility	33
3.5	Antenna-to-Satellite LOS visibility	33
3.6	GPS satellite antenna 2D pattern from [78]	34
3.7	Satellite altimetric measure [80]	35
3.8	ISL ranging contacts	36
3.9	Satellite-to-beacons contacts	38
4.1	3D position (left) and velocity(right) error for DSN only case with 8-hours of tracking for 1 and 2 windows from top to bottom respectively	46
4.2	3D position (left) and velocity (right) error for DSN only case with 4-hours windows of tracking for 1, 2 and 3 days of time span from the top to the bottom respectively	47
4.3	Observables availability for 4-hours-a-day windows (right) and 8-hours-a-week (left)	48
4.4	3D position (left) and velocity (right) error for DSN and altimeter scenario with two 8-hours windows of tracking	50
4.5	3D position (left) and velocity (right) error for DSN and altimeter scenario with 4-hours windows of tracking for 2, 3 and 7 days of time span from the top to the bottom respectively	52

4.6	Least squares $\Lambda$ matrix conditioning (top) and observables availability (bottom) for two beacons and ISL: 1 corresponds to all 24 observables available while 0 indicates that at least one observable is not available. . . . .	53
4.7	3D position error for 3 beacons and ISL scenario in the absence of measurement noise for 2 days of simulation . . . . .	54
4.8	3D position error for 3 beacons and ISL scenario with measurement noise on range and range-rate from ISL and range-rate from beacons for 24 h of simulation . . . . .	55
4.9	3D position error for 3 beacons and ISL scenario with measurement noise on all observables for 2 days of simulation . . . . .	55
4.10	3D position error for 3 different locations of the third beacon progressively moved further from the South Pole (from the top image to the bottom) . . . . .	57
4.11	3D position error for 3 beacons and ISL scenario with long arch OD algorithm for 4 days of simulation . . . . .	58
4.12	3D position and velocity errors for Keplerian scenario with 2 beacons, ISL and altimeter, 24 hours of simulation, 1 batch of observables per minute and increasing time span from top to the bottom (30,60 and 90 minutes) . . . . .	60
4.13	3D position and velocity error for the Keplerian scenario with 2 beacons, ISL and altimeter with long arch OD algorithm for 24 hours of simulation, 1 batch of observables per second, increasing time span from top to the bottom (30, 60 and 90 minutes) . . . . .	61
4.14	Number of observables collected per epoch (Keplerian model) . . . . .	62
4.15	3D position and velocity error for the scenario with 2 beacons, ISL and altimeter with long arch OD algorithm for 24 hours of simulation, 1 batch of observables per minute and perturbed ELFOs (dynamical model known), increasing time span from top to the bottom (30, 60 and 90 minutes) . . . . .	63
4.16	3D error for 2 beacons, ISL and altimeter compared to observables availability for real perturbed case and long arch algo with 30 minutes of time span . . . . .	64
4.17	3D position error (left) and detail(right) for real perturbed scenario (limited knowledge of dynamical model) with 2 beacons, ISL and altimeter, 1 batch of observables per minute and increasing time span from top to the bottom (30, 60 and 90 minutes) . . . . .	65
4.18	3D velocity error (left) and detail(right) for real perturbed scenario (limited knowledge of dynamical model) with 2 beacons, ISL and altimeter, 1 batch of observables per minute and increasing time span from top to the bottom (30, 60 and 90 minutes) . . . . .	66

4.19	Number of observables collected per epoch (Keplerian model) . . .	67
4.20	3D position and velocity errors for the Keplerian scenario with 3 beacons, ISL and altimeter with long arch OD algorithm for 24 hours of simulation, 1 batch of observables per minute and increasing time span from top to the bottom (30, 60 and 90 minutes) . . . . .	69
4.21	3D position and velocity errors for the Keplerian scenario with 3 beacons, ISL and altimeter with long arch OD algorithm for 24 hours of simulation, 1 batch of observables per second and increasing time span from top to the bottom (30, 60 and 90 minutes) . . . . .	70
4.22	3D position and velocity errors for the perturbed scenario (dynamical model known) with 3 beacons, ISL and altimeter with long arch OD algorithm for 24 hours of simulation, 1 batch of observables per minute and increasing time span from top to the bottom (30, 60 and 90 minutes) . . . . .	71
4.23	3D position error (left) and detail(right) for real perturbed scenario (limited knowledge of dynamical model) with 3 beacons, ISL and altimeter, long arch OD algorithm, 1 batch of observables per minute and increasing time span from top to the bottom (30, 60 and 90 minutes), 24h of simulation . . . . .	72
4.24	3D velocity error (left) and detail(right) for real perturbed scenario (limited knowledge of dynamical model) with 3 beacons, ISL and altimeter, long arch OD algorithm, 1 batch of observables per minute and increasing time span from top to the bottom (30, 60 and 90 minutes), 24h of simulation . . . . .	73
4.25	Number of observables available overtime for the scenario with three beacons, ISL, DSN and altimeter (perturbed scenario) . . . . .	74
4.26	3D position and velocity error for Keplerian scenario with 3 beacons, ISL, DSN and altimeter, long arch OD algorithm, 1 batch of observables per minute and increasing time span from top to the bottom (1, 2 and 4 hours), 48h of simulation . . . . .	75
4.27	3D position and velocity error for Keplerian scenario with 3 beacons, ISL, DSN and altimeter, long arch OD algorithm, 1 batch of observables per second and increasing time span from top to the bottom (1, 2 and 4 hours), 48h of simulation . . . . .	76
4.28	3D position and velocity error for Keplerian scenario with 3 beacons, ISL, DSN and altimeter, long arch OD algorithm, 1 batch of observables per minute and increasing time span from top to the bottom (12 and 24h), 72h of simulation . . . . .	78

4.29	3D position and velocity error for Keplerian scenario with 3 beacons, ISL, DSN and altimeter, long arch OD algorithm, 1 batch of observables per second and increasing time span from top to the bottom (12 and 24h), 72h of simulation . . . . .	79
4.30	3D position and velocity error for the perturbed scenario (dynamical model known) with 3 beacons, ISL, DSN and altimeter, long arch OD algorithm, 1 batch of observables per minute and increasing time span from top to the bottom (1h,2h and 12h), 24h of simulation	80
4.31	3D position error (left) and detail (right) for the perturbed scenario (limited knowledge of dynamical model) with 3 beacons, ISL, DSN and altimeter,1 batch of observables per minute , 24h of simulation	81
4.32	Number of observables available overtime for the scenario with Earth's GNSS and the on-board altimeter . . . . .	82
4.33	3D position and velocity error for Keplerian scenario with GNSS and altimeter, long arch OD algorithm, 1 batch of observables per minute and increasing time span from top to the bottom (24, 48 and 72 hours), 8 days of simulation. Lower level of noise. . . . .	84
4.34	3D position and velocity error for Keplerian scenario with GNSS and altimeter, long arch OD algorithm, 1 batch of observables per minute and increasing time span from top to the bottom (24, 48 and 72 hours), 8 days of simulation. Higher level of noise. . . . .	85
4.35	3D position and velocity error for the perturbed scenario with GNSS and altimeter (dynamical model known), long arch OD algorithm, 1 batch of observables per minute and increasing time span from top to the bottom (12, 24 and 36 hours), 3 days of simulation. . . . .	86
4.36	Number of observables available overtime for the scenario with Earth's GNSS, DSN and the on-board altimeter . . . . .	88
4.37	3D position and velocity error for Keplerian scenario with GNSS, DSN and altimeter, long arch OD algorithm, 1 batch of observables per minute and increasing time span from top to the bottom (24, 48 and 72 hours). 8 days of simulation. . . . .	89
4.38	3D position and velocity error for perturbed scenario with GNSS, DSN and altimeter, long arch OD algorithm, 1 batch of observables per minute and increasing time span from top to the bottom (8, 12 and 24 hours). 8 days of simulation. . . . .	90
A.1	Implementation of the rise-set function of section 3.4.1 . . . . .	101
A.2	STK and MATLAB interconnections in the present work . . . . .	102



# Acronyms

AGI	Analytical Graphics Inc.
BLS	Batched Least Squares
CDSN	China Deep Space Network
CLPS	Commercial Lunar Payload Services
CNES	Centre National d'Études Spatiales
CNSA	China National Space Administration
Center Of Mass	Center Of Mass
CSA	Canadian Space Agency
CSAC	Chip Scale Atomic Clock
DORIS	Doppler Orbitography and Radiopositioning Integrated by Satellite
DSA	Deep Space Antenna
DSAC	Deep Space Atomic Clock
DSN	Deep Space Network
EKF	Extended Kalman Filter
ELFO	Elliptical Lunar Frozen Orbits
ESA	European Space Agency
ESTRACK	European Space Tracking
GNSS	Global Navigation Satellite System
GPS	Global Positioning System
HALO	Habitation and Logistic Outpost
HPOP	High Precision Orbit Propagator
IAU	International Astronomical Union
ICRF	International Celestial Reference Frame
IGS	Institut Géographique National

INPE	Instituto Nacional de Pesquisas Espaciais
ISL	Inter-Satellite Link
ISRO	Indian Space Research Organization
JAXA	Japanese Aerospace Exploration Agency
JPL	Jet Propulsion Laboratory
KARI	Korean Aerospace Research Institute
KDSA	Korea Deep Space Antenna
KPLO	Korea Pathfinder Lunar Orbiter
LCNS	Lunar Communications and Navigation Services
LOLA	Lunar Orbiter Laser Altimeter
LOS	Line-Of-Sight
LRNS	Lunar Radio Navigation System
MSFN	Manned Space Flight Network
NASA	National Aeronautics and Space Administration
NAVSTAR GPS	NAVigation, Satellite Timing And Ranging Global Positioning System
NRHO	Near-Rectilinear Halo Orbit
OD	Orbit Determination
ODE	Ordinary Differential Equations
ODTS	Orbit Determination and Time Synchronization
PNT	Positioning Navigation and Timing
PPE	Power and Propulsion Element
RKF	Runge-Kutta-Fehlberg
SANSA	South Africa National Space Agency
SLIM	Smart Lander for Investigating Moon
SLR	Satellite Laser Ranging
SLS	Space Launch System
SPODP	Single Precision Orbit Determination Program
SRP	Solar Radiation Pressure
SST	Satellite-to-Satellite Tracking

STK	Systems Tool Kit
TDRSS	Tracking and Data Relay Satellite System
UAESA	United Arab Emirates Space Agency
USN	Universal Space Network
VLBI	Very Large Baseline Interferometry
WGS	World Geodetic System

# Chapter 1

## Introduction

The next global strategic priority in space exploration is a stable and sustainable human presence on the Moon. There are currently 14 space agencies undersigning the new Global Exploration Roadmap (Figure 1.1, from [1] ), a shared vision embracing governments and private companies aiming to expand human presence in Earth orbit, to the Moon and on Mars. Dozens of technological demonstrations, unmanned scientific missions and manned landings on the Moon surface are planned for this decade and will pave the way for the new lunar economy of space exploration that is now emerging.

The recent discovery of water ice at the Moon South Pole [2] - which had been hypothesized for long [3] - provides an extremely important resource that adds up with the mineral abundance of the lunar crust. The potential of these ice reservoirs is to provide both drinking water and oxygen for breathing for astronauts continuative presence both on the surface and in orbit and also hydrogen-oxygen based fuels for power and thrust [4].

With the Lunar Gateway, an orbiting space station in cis-lunar environment, a complete communication and operation support will be given on the Moon surface, driving the deployment of further infrastructures that will allow the establishment of habitats, robots, commercial routes and transportation as the first steps towards a lunar colony. The Gateway will enable three key features in lunar surroundings [1]: reusability of vehicles thanks to refuelling and servicing in a stable orbital environment; testing of new technologies in deep space and readiness assessment; accessibility from all the space agencies and private actors thanks to the proximity of the Moon - with respect to Mars, for example.

Every technological success of the Moon campaign, will be a progress for Mars exploration. Indeed, it will be possible to demonstrate deep space habitation and

transportation, crew protocols, operational autonomy, vehicle maintenance and refuelling and infrastructure building abilities. Surface rovers capabilities and exploration strategies will also be assessed, analyzing new power generation systems like nuclear-based and sample return possibilities.

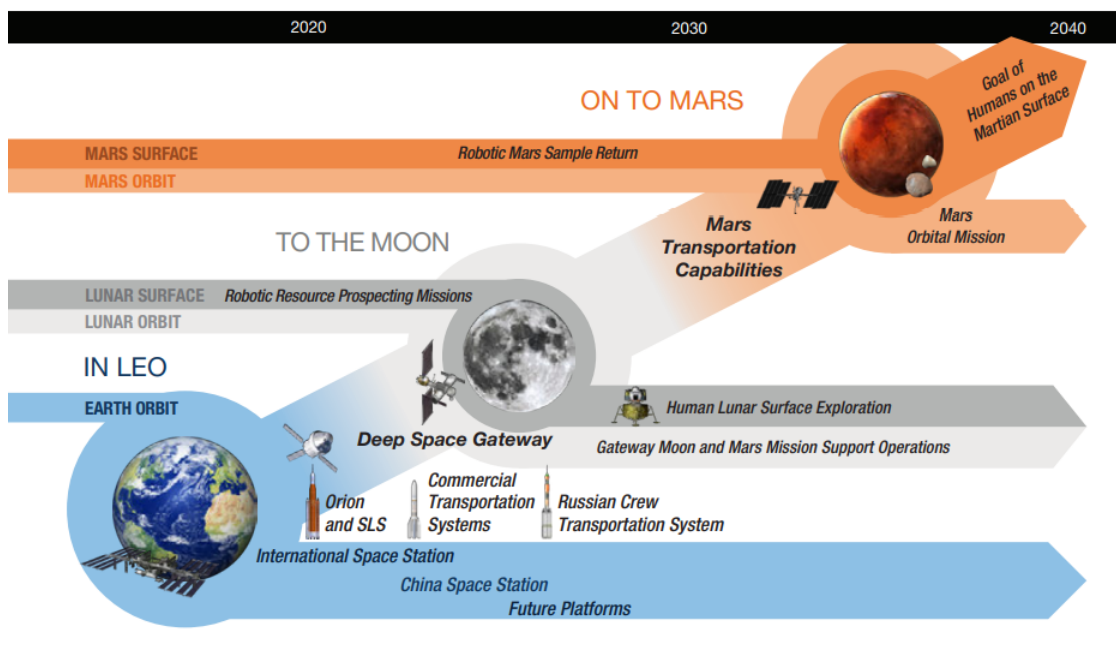


Figure 1.1: Global exploration roadmap [1]

## 1.1 The Moon exploration

At the beginning of the last century, space travel was no more than science fiction; at its end, an established achievement. The ideas and intuitions of fathers of space flight like Tsiolkovsky(1857-1935), Goddard(1882-1945) and Oberth(1894-1989) were supported by a catalyzing historical climate that started with World War II and continued with the Cold War providing dramatic fundings for the space programs[5].

The first artificial satellite, the Sputnik, was launched in 1957 and after four years Yuri Gagarin(1934-1968) gave birth to the manned space flight era. Thereafter, only 12 years later, on July 20, 1969, Neil Armstrong(1930-2012) set foot on the Moon. The Apollo program (1961-1972) and the Soviet Luna missions(1959-1976) generated a pioneering technological know-how for deep space exploration that paved the way for the modern space era that we know today.

While the Japanese Institute of Space and Astronautical Science (ISAS) had made its entrance in this framework in the early 90s, the European Space Agency's first mission to the Moon was the 2003 SMART-1, a successful technological demonstrator for new propulsion, science and communication techniques in deep space [6]. Between 2007 and 2008 the number of space agencies joining the Moon campaign increased dramatically: the Chinese Chang'e lunar program started in October 2007 with Chang'e 1, followed by the first Indian lunar probe Chandrayaan-1 in late 2008 while the Kaguya probe by the new Japanese Aerospace Exploration Agency (JAXA), formed in 2003, reached a selenocentric orbit in September 2007. One of the most successful recent lunar missions is the Lunar Reconnaissance Orbiter (LRO): launched in 2009 and still operative in an eccentric polar orbit, LRO is providing highly detailed surface mapping that has had and will continue to have a key strategic importance in future missions planning. An extremely accurate gravitational mapping of the Moon has been carried out as well thanks to the NASA's 2011 Gravity Recovery and Interior Laboratory (GRAIL) science mission.

In more recent times, Israel attempted without success their first lunar landing mission with the Baresheet spacecraft in 2019, the Indian Space Research Organization (ISRO) launched Chandrayaan-2 in the same year [7] and the China National Space Administration (CNSA) successfully returned lunar samples on Earth in late 2020 with Chang'e 5 [8].

In the next years a peak in the number of lunar missions is going to be reached, with the Artemis program and ESA Moonlight initiative - that will be discussed in the next sections - leading the campaign. The Smart Lander for Investigating Moon (SLIM) by JAXA, a demonstrative rover, is expected to launch in early 2022 followed by Roscosmos' Luna 25 mission as part of the Luna-Glob exploration program. This latter consists in a series of expeditions to permanently establish an independent and autonomous base on the Moon by the Russian government. In the same year Korea Pathfinder Lunar Orbiter (KPLO) by the Korea Aerospace Research Institute (KARI) and ISRO's Chandrayaan-3 will expand the robotic presence in lunar environment [9]. IM-2 and Mission One by the American companies Intuitive Machines and Astrobotic Technology will be among the firsts private partners to join the Moon campaign. The United Arab Emirates Space Agency (UAESA) will participate with the Emirates Lunar Mission on board a Falcon 9 rocket as well [10].

From 2023 on several others private partners and space agencies plan to take part: the Turkish Space Agency which has been advancing its know-how in the last few years announced a Moon mission by 2023 [11]; Brazil's Garat ea-L probe

by Airvantis and INPE<sup>1</sup> will be insert in selenocentric orbit by 2023 as well [12]; Australia Lunar Exploration Mission will provide nanosatellites for NASA's Artemis; China Chang'e program will explore the Moon South Pole with rovers until the 2026 crew landing; Roscosmos is likely to conduct a crewed lunar flyby by 2029 with the Orel spacecraft [13]; South Africa National Space Agency (SANSA) plans to join with an orbiter by 2030[14].

A complete list of past, current and future planned lunar mission both by commercial and institutional partners can be found in [15].

## 1.2 The Artemis Program

Named after Apollo's sister, Artemis is NASA's space program to create a stable and sustainable human presence on the Moon and will serve as a testbed for future Mars exploration.

The Lunar Gateway, the space station that is likely to orbit Lagrange L1 point<sup>2</sup> in a Near-Rectilinear Halo Orbit (NRHO), will be crucial from the early stages of Artemis, providing a reliable and multipurpose infrastructure for science researches, Moon landing, in-orbit operations and re-entry to Earth. The Power and Propulsion Element(PPE) and the Habitation and Logistic Outpost(HALO) will be assembled on Earth and launched by 2023, while the rest of the station will be integrated in orbit thanks to a quick and robust supply chain increasingly involving private companies. Indeed, NASA's Commercial Lunar Payload Services (CLPS) partnership with the private sector is a major catalyst in the development of a new Moon economy which will greatly benefit from the exploitation of in situ resources. On the other hand, ESA, JAXA and the Canadian Space Agency (CSA) will be the main intergovernmental contributors to the Gateway, while the Russian Space Agency (Roscosmos) has expressed interest in participating to the space station realization [17].

The Space Launch System (SLS) rocket, the launcher designed for Artemis, currently in its final development stage will be the most powerful ever built with more

---

<sup>1</sup>Instituto Nacional de Pesquisas Espaciais, the civilian research institute for aerospace activities.

<sup>2</sup>The Lagrange points, or libration points, are stationary points in the gravitational field potential of a system composed of two large bodies. They are located in particular regions where the gravitational force of the bodies and the centrifugal force balance each other [16]. They are of high interest, requiring few station keeping maneuvers and thus being fuel efficient long time stable orbits.

than 16 MN of thrust in the vacuum and will be able to feature the Orion spacecraft on top. These latter will be the exploration vehicle used in the manned mission that will carry a crew of up to 6 astronauts in cis-lunar environment. Orion's first crewed flight to the Moon is currently planned for 2024 with Artemis II mission. In Figure 1.2 below NASA's roadmap to 2024 with the cornerstones of the program is reported.

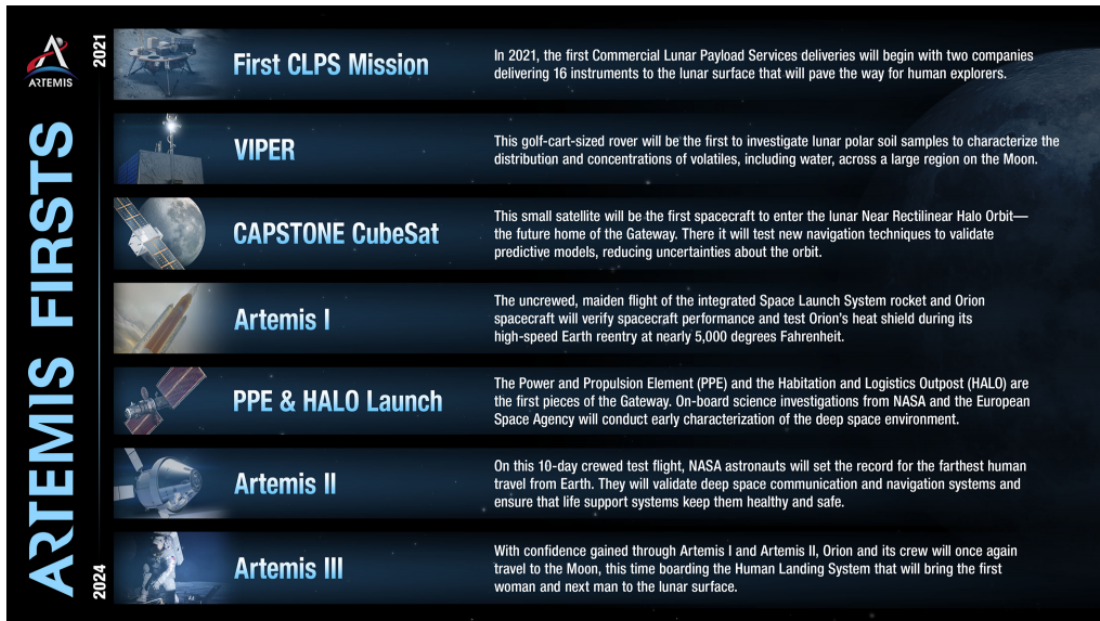


Figure 1.2: Artemis roadmap to 2024 [17]

Artemis I, the first mission featuring the new integrated SLS and Orion module, will also exploit excess volume on the SLS to transport to lunar environment a batch of 13 CubeSats that will conduct science experiments and technological demonstrations to support the successive phases of the program.

A scalable architecture is of fundamental interest in the Artemis program to create an unprecedented know-how on deep space infrastructures preparing for Mars exploration. A permanent base will be developed at the South Pole to support surface operations and logistics. The choice of this region is driven by scientific and logistic implications: a key trait of the landing site for example is the high percentage of time in Sun lit conditions, since the solar radiation will be, at least in the first phases, the most significant power source available on the surface; it is also important both for astronauts and infrastructures to have a limited range of temperatures to deal with to reduce design complexities that would arise with

long eclipse periods. As anticipated, the water ice found at the South Pole is also an important resource for the establishment of a functional base camp and this region has a continuative line of sight to Earth as well which will be necessary at least until an advanced lunar autonomous architecture will fully be operative. A safe landing and roving site in the nearby also has to be available to ensure limited risks and effective exploration capabilities [17].

From a scientific return perspective, Artemis will align its goals with the scientific community studies firstly through orbiting payloads, then on the surface through robotic expeditions and finally with an astronaut operated laboratory in the base camp near the South Pole. The main objectives here include chemical composition studies, planetary science, researches on solar system evolution, space weather experiments, tests on human surviving capabilities in deep space, universe observation from vantage location.

### 1.3 ESA Moonlight and the LCNS

Regardless of the ever increasing number of missions targeting lunar orbits, there is currently no such thing as a dedicated navigation and telecommunication system to satisfy all missions needs, especially for small satellites and future lunar surface users; this is highly inefficient and limiting since it implies that each mission must rely on a different ad hoc developed solution.

The ESA's Moonlight initiative aim is to provide a common Lunar Communication and Navigation System that will support the ongoing and planned missions of all the Artemis partners and other private spacecrafts. The LCNS will be made up of a constellation which is still to be defined and Moon's surface infrastructures and will result from a trade-off between communication needs, like constantly linking the lunar far side to Earth, and precise navigation needs that are currently being investigated in terms of accuracy, latency and surface coverage. This system will allow the astronauts to virtually land in any location and to move around maintaining a connection with Earth's ground control and other lunar users. Having a unique service provider will also reduce design complexity and allow lighter spacecrafts [18], thus increased cargo capability or science payload volume. Such a system will be of fundamental importance in successful landing operations that require high fidelity Guidance Navigation and Control (GNC) systems [4].

#### 1.3.1 The PNT roadmap

Within Moonlight initiative, the Positioning, Navigation and Timing (PNT) service is expected to follow an implementation roadmap depicted by ESA in [4] and

reported in Figure 1.3. The most noteworthy aspect, as anticipated, is the system scalability. The earliest expeditions will need relatively low PNT accuracy and availability, mainly targeting Moon centered orbits or libration points. Navigation support will also be required during Earth-Moon transfer orbits. This initial mission phase, expected to last until around 2025, will try to exploit GNSS signals from Earth’s constellations through high sensitivity receivers that are going to be tested in the Lunar Pathfinder missions planned for 2023. ESA argues that the side lobes of the antenna radiation pattern of GNSS satellites can be employed for PNT even at Moon’s distance [19]. The receiver on-board Lunar Pathfinder will assess the effectiveness of this technology with a high gain antenna to receive both Galileo and GPS . This solution, if feasible, would allow massive cost reduction and a fast-delivery asset for lunar PNT.

The successive phase will provide an augmentation system to enhance GNSS based navigation with more ranging signals, establishing the Lunar Radio Navigation System. The aim of the LRNS is to focus the PNT improvements on the Moon South Pole to allow first landings and ascending operations and ensure a good coverage for surface operations in that region. This will be done through a dedicated constellation of three to four satellites and eventually surface beacons.

From 2035 onwards, a fully autonomous PNT Lunar System is targeted. A complete coverage of the Moon’s surface and high PNT performances are expected to be reached with additional orbiting satellites and ranging beacons. Realizing an independent system will ensure reliability, redundancy and robustness and relax mission constraints concerning navigation and communication capabilities.

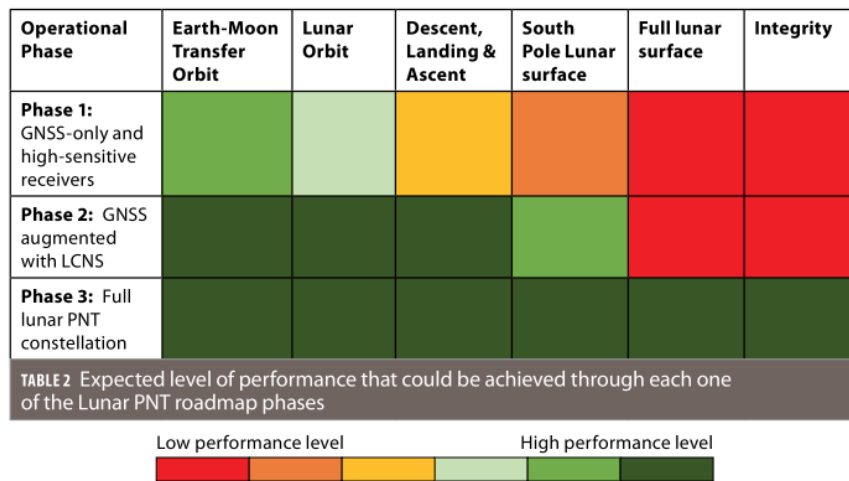


Figure 1.3: ESA PNT implementation roadmap

### 1.3.2 The Elliptical Lunar Frozen Orbits (ELFO)

To design a dedicated constellation for LCNS for PVT and communications, it is required an optimization in the satellites' orbits choice to both guarantee coverage of surface regions of major mission interest and minimize the fuel consumption needed for station keeping to extend the constellation life. The consistency of this properties overtime is also a driver parameter. The main perturbations influencing lunar environment are Sun's and Earth's third bodies accelerations, Moon's gravitational field asymmetries and solar radiation pressure. The most effective solution was primarily proposed in [20] and further elaborated in [21] and consists of a constellation of Elliptical Lunar Frozen Orbits (ELFO). These orbits exhibit more than 10 years of stability thanks to a pinpoint selection of their fundamental parameters, particularly eccentricity, semi-major axis, inclination and argument of periselene. The process of parameter selection is detailed in [22].

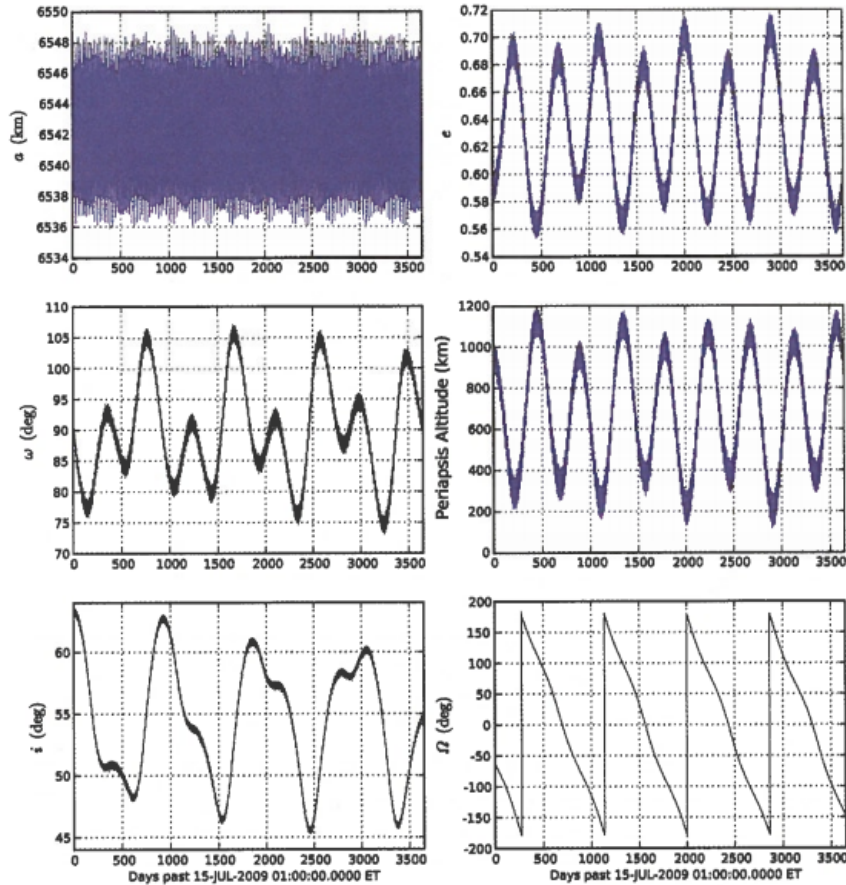
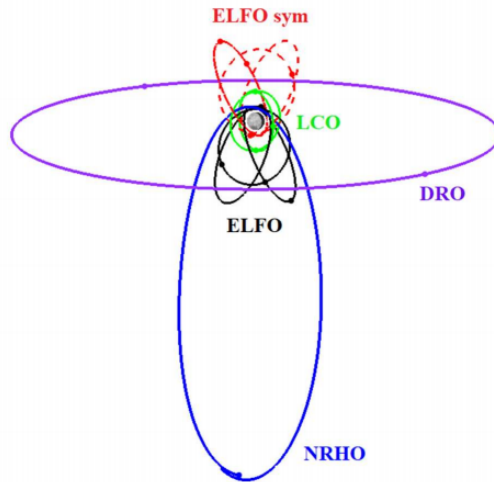


Figure 1.4: Orbital Elements of a simulated ELFO from [20]

In Figure 1.4 the orbital elements variation of a simulated ELFO from [20] are shown. Although deviations from the mean reference are allowed, there's no secular effect causing drift and only periodic acceptable oscillations occur. In Figure 3.3 and 3.1 the simulated ELFOs for the present work studies are illustrated together with their parameters indicated in table 3.1. The constancy of these orbits ensures continuative long-term South Pole coverage at minimum delta-V. It would also be possible to create a "Northern" ELFO constellation, i.e, with the periselene above the Moon South Pole thus spending most time over the North Pole, as suggested in [4] in the third phase of the PNT roadmap to achieve a complete coverage of the surface, a better Geometric Dilution Of Precision (GDOP) and improve service availability.

In Figure 1.5 below an ideal LCNS constellation from [23] is reported. Both Southern and Northern ELFO can be seen as well with a NRHO that could host the Lunar Gateway as discussed in section 1.2. Other trajectories of high interest are the Distant Retrograde Orbits (DRO) that, although appearing to orbit the Moon in a retrograde way, they actually orbit the Earth and are perturbed by Moon's third body acceleration.



**Figure 1.5:** LCNS third phase conceptual constellation from [23]

## 1.4 Present work purpose and outline

Since the benefits of a dedicated lunar communication and navigation service are unquestionable, a critical aspect to be dealt with is the choice of the best algorithm

to be implemented in order to perform orbit determination of the satellites that will compose the lunar navigation system. The aim of the present work is to implement a precise OD algorithm for a possible satellite navigation constellation and evaluate its performances when expanding the PNT architectures proposed in the aforementioned ESA's roadmap. Particular attention will be given to the wide variety of observables, their modelization, measurement noise, availability and interaction when increasing system complexity.

In the following chapter the generalized OD problem is presented. After giving some historical background and exposing modern tracking systems, some mathematical background is given within the OD algorithms context. After that, observables and the observability issue are presented, as well as the time synchronization problem and tracking error sources.

In chapter 3 the case study is presented: the orbit determination of the satellites of the lunar navigation system. This chapter is fully dedicated to illustrate the models, geometries and algorithms considered and to explicit all the hypothesis and assumptions that were made in this work and are necessary to demonstrate and comprehend the results of the successive chapter.

Chapter 4 presents all the simulation results with an increasing architecture complexity, starting from DSN-only tracking then up to cross-linking measurements, surface beacons ranging and altimetric data.

Chapter 5 is aimed to point-out the benefits and drawbacks of the different architectures, trying to assess whether a specific scenario OD improvements are worth the increased complexity.

The last chapter ties up the whole work, summarizes the main and fundamental results and gives recommendations for further studies.

Appendix A provides additional insight into the software tools used in the present work (STK and MATLAB) and their role in the simulation of the scenarios and in the design of the OD algorithm. Appendix B goes into more detail about the state transition matrix and illustrates a possible approach for its calculation when dealing with perturbed models which generally requires a severe computational effort.

## Chapter 2

# Orbit determination techniques

"Satellite orbit determination (OD) can be described as the method of determining the position and velocity (i.e., the state vector, state, or ephemeris) of an orbiting object such as an interplanetary spacecraft or an Earth orbiting satellite".[24] The basic principle is the correction of an a-priori state estimate through a finite set of observables collected at the present epoch or through a batch of measurements collected at different epochs and mapped back to the state estimation epoch. A reference trajectory is generated from the a-priori state and updated through the algorithm which processes the observables (Fig.2.1 , from [25]). The solution of the OD algorithm is the "best estimate" of the state vector, meaning that it is the result of a statistical optimization, as it will be discussed later.

Both one-way and two-way techniques are used today to track orbiting objects: the first method consists in the transmission of a signal which is received by another instrument capable of using it to calculate range and range-rate between the transmitter and the receiver; in two-way ranging the signal is transmitted back to the initial source after the reception and then used to calculate the observables.

A key point in the OD process is the accurate description of the force field acting on the spacecraft, which is composed by a highly nonlinear set of equations whose complexity must be generally traded-off for numerical stability, computational time and effort, performing solution techniques and overall OD algorithm accuracy. The uncertainties in the dynamical model of the spacecraft motion are the main limiting factor in the orbit determination process: the complete set of perturbing external forces is never known exactly and some of the parameters involved in the description of this force field (e.g. spherical harmonics coefficients of the gravity

potential field) must be often estimated alongside the state vectors. The detailed description of the physics behind the satellites motion in cis-lunar environment is beyond the purpose of this dissertation, however a brief summary of the considered forces will be given in the next chapter in the case study scenario description. Other sources of error in the OD solution are systematic and random errors in the instrumentation that lead to incorrect observations and numerical approximations and instability both in the integration processes and in computer round-offs.

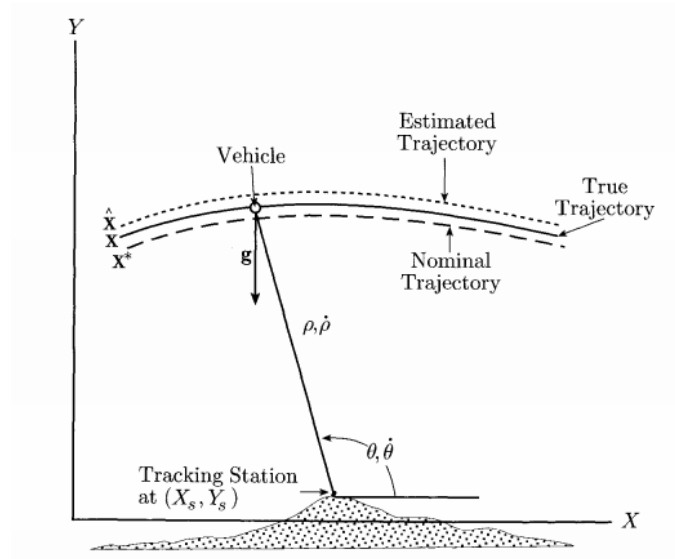


**Figure 2.1:** Estimated, reference (nominal) and true trajectory during OD process

The following sections will deal with some historical background on orbit determination, the state-of-the-art tracking systems and algorithms, the most commonly used measurements in the OD process and the observability problem.

## 2.1 A brief history

Although astronomical observations evidence can be dated as back as the second millennium Before Christ in ancient Egypt, when theories on the creation and motion of the Sun and stars and of the whole sky were developed, the modern scientific method based on observations, experiments and iterative thinking started being consistently used from the 16th century A.D. At the time, scientists like Copernicus(1473-1543), Kepler(1571-1630), Galileo(1564-1642), Tycho Brahe(1546-1601) and later Isaac Newton(1643-1727), developed both important mathematical tools and astronomical observations that posed the basis for the modern orbit

determination techniques and orbital mechanics in general.

Even with the more advanced theories, instruments, mathematical tools and physical insights introduced with Lambert(1728-1777), Euler(1707-1783), Lagrange(1736-1813) and Laplace(1749-1827) in the 18th century though, the orbit determination was a deterministic process back then. Indeed, a minimum set of parameters to estimate that uniquely determine a celestial body's orbit<sup>1</sup> was selected and a number of independent observations equal to the unknowns was gathered and used to solve for the body state vector. It is only with Gauss(1777-1855) and Legendre(1752-1833) and the development of the Least Squares Method that the modern orbit determination was born. [26]

The idea behind modern orbit determination techniques is the use of large amounts of tracking data, generally much larger than the number of unknowns to be estimated and the inclusion of errors propagation theory in the algorithms. The Least Squares Method was a fundamental step in the OD methods evolution because it allowed to mathematically solve these over-determined problems and consider the errors on each measure through a weighting matrix.

Although this method was known since Gauss, who used it to predict Ceres' orbit, it was not until 1950s, when the first space programs were born, that the modern trajectory prediction theories were extensively developed. During the 1960s and 1970s the technological advance made in the optical measurement systems and in radio frequency instruments led to an ever increasing performance in satellite tracking, which, combined with the progress of computing technologies and mathematical force models allowed precise satellite orbit determination to be carried out consistently. [25]

## **2.2 Tracking systems**

Modern tracking systems can be both ground-based or spaceborne. The Doppler Orbitography and Radiopositioning Integrated by Satellite (DORIS) is an example of the former ones. DORIS is a one-way tracking system developed by the Centre National d'Études Spatiales (CNES) and the Institut Géographique National (IGN) and operative since 1990. It is composed of about 60 ground stations equipped with a ranging beacon transmitting in two frequencies and used as geographic references by the orbit determination software. Some of the beacons also have time monitoring capabilities being linked to precise atomic clocks. [27] Another widely

---

<sup>1</sup>E.g., the position and velocity in an inertial reference frame or the orbital parameters

used technique is the Satellite Laser Ranging (SLR), which exploits retroreflectors equipped on satellites to calculate their range from several laser stations. SLR systems can nowadays achieve precision in the range of one centimeter using tens of evenly distributed ground stations. [28]. Other noticeable examples are NASA's Deep Space Network (DSN), and the European Space Tracking (ESTRACK). These networks consist in several stations around the world providing a link between Earth orbiting or deep space (DSN and DSA) satellites and the missions control centers. As it is part of the present case study simulated environment, more details on the DSN configuration will be given in the next chapter.

Spaceborne tracking systems exploit ranging from satellites instead of ground stations. The GNSS is the most prominent example, with several operative constellations like Galileo, GPS, GLONASS, BeiDou providing positioning and time-transfer services. NASA's Tracking and Data Relay Satellite System (TDRSS), a constellation of geosynchronous satellites for tracking and communication support [29], is another example of spaceborne system. At March 2019, TDRSS was composed of ten operative spacecrafts [30]. All these systems rely on complex ground control for satellites monitoring, checking for signal integrity, clocks synchronization, constellation health status and trajectory corrections: e.g. GPS ground segment is composed of a master control station, an alternate master control station, eleven command and control antennas and sixteen monitoring sites. [31]

## **2.3 Orbit determination algorithms**

Orbit determination techniques can be divided into batch and sequential estimation processors: the former consists in processing a batch of observations from different epochs to update the state estimation at a given time and it is based on the Gauss least squares approach; the latter, more suitable for real-time OD applications, updates the state at each epoch using only the measurements relative to that epoch. The two methods, in the absence of process noise would mathematically be equivalent [25], producing the same solution with the same observations. Both classes of algorithms have proved to be reliable and accurate and the choice of the one to implement depends on several factors like mission architecture, available resources, computational burden that can be sustained, state update time intervals required, precision, numerical stability and other considerations vastly discussed in [28]. Whatever the algorithm used for the OD is, the fundamental information that is used to estimate the trajectory is the difference between the modeled observations and the real measurements from the sensors. This knowledge translates into an insight of the deviation of the real orbit from the reference estimated one.

The position and velocity of a satellite form its state vector, hence defined as:

$$X = \begin{bmatrix} x \\ y \\ z \\ V_x \\ V_y \\ V_z \end{bmatrix} = \begin{bmatrix} \dot{x} \\ \dot{y} \\ \dot{z} \\ \dot{x} \\ \dot{y} \\ \dot{z} \end{bmatrix} \quad (2.3.1)$$

Generally, other parameters concerning force and measurement models need to be included in the estimation and are added to the state vector but they can be treated in a unified way and no distinction between trajectory and parameters estimation has to be made [28].

In the general case, a set of non-linear differential equations governs the evolution of the state vector over time. The following procedure is derived from [25]. One can write:

$$\dot{X} = F(X, t) \quad X(t_i) = X_i \quad (2.3.2)$$

with  $X(t_i)$  being the state vector at time  $t_i$ . As anticipated, an observation model must be introduced, which is also made of highly non linear equations in the state vector and time variables, denoted with  $G(X, t)$ . The real observables will differ from the calculated ones for a measurement error vector  $\epsilon$ , thus:

$$Y = G(X, t) + \epsilon \quad (2.3.3)$$

$Y$  being the vector comprising all the real observables gathered at time  $t$ .

If the a-priori knowledge (initial guess) of the trajectory is denoted with  $X^*$ , the two following quantities can be defined:

$$x(t) = X(t) - X^*(t) \quad y(t) = Y(t) - Y^*(t) \quad (2.3.4)$$

where  $x$  and  $y$  are, respectively, the state and observations deviation vectors. Expanding (2.3.2) and (2.3.3) in a Taylor's series about the reference trajectory  $X^*$  yields:

$$\dot{x}(t) = A(t)x(t) \quad \text{and} \quad y = Hx + \epsilon \quad (2.3.5)$$

where

$$A(t) = \left[ \frac{\partial F(t)}{\partial X(t)} \right]^* \quad (2.3.6)$$

$$H(t) = \left[ \frac{\partial G(t)}{\partial X(t)} \right]^* \quad (2.3.7)$$

are matrices containing the partial derivatives of, respectively, the dynamical and the observations model with respect to the state vector components, evaluated on the reference trajectory  $X^*$ . Equation (2.3.5) represents the linearized estimation problem, which is now formulated in a way that allows the use of powerful mathematical tools like Gauss' method.

### 2.3.1 Batched Least Squares algorithm

The idea behind the least squares approach is to minimize the squared sum of the residuals considered in the following performance index:

$$J(x) = \frac{1}{2} \epsilon^T \epsilon$$

where  $\epsilon = y - Hx$  from eq. (2.3.5). Thus:

$$J(x) = \frac{1}{2} \epsilon^T \epsilon = \frac{1}{2} (y - Hx)^T (y - Hx) \quad (2.3.8)$$

In [25] it is further demonstrated that deriving  $J(x)$  to find its minimum, ultimately leads to the normal equations:

$$(H^T H)x = H^T y \quad (2.3.9)$$

From which:

$$x = (H^T H)^{-1} H^T y \quad (2.3.10)$$

Therefore, the new estimate for the state vector can be derived from equation (2.3.4):

$$X = X^* + x \quad (2.3.11)$$

The procedure described up to here only involves using a set of observables from a single epoch, which is the traditional least squares method. In order to use a batch of data from different epochs to improve the estimate, it is necessary to introduce the state transition matrix  $\Phi$ . This matrix is used to map the deviations in the state vector from one epoch to another and it is defined as:

$$\Phi(t, t_0) = \left[ \frac{\partial X(t)}{\partial X_0} \right] \quad (2.3.12)$$

where  $X_0 = X(t_0)$ . If one wants to estimate the state vector at time  $t_0$  using also observables gathered at time  $t_i$ , the  $H_i$  matrix calculated at time  $t_i$  must be mapped back to epoch  $t_0$  through  $\Phi$ :

$$H_i = \widetilde{H}_i \Phi(t_i, t_0) \quad (2.3.13)$$

and then, before solving the normal equations, one can simply accumulate the  $H_i$  matrices of the  $l$  different epochs from which observables are gathered as follows:

$$H^T H = \sum_{i=1}^l H_i^T H_i = \sum_{i=1}^l [\widetilde{H}_i \Phi(t_i, t_0)]^T \widetilde{H}_i \Phi(t_i, t_0) \quad (2.3.14)$$

Assuming that the observation errors  $\epsilon$  can be modelled as white noise, it is possible to introduce a weighting matrix  $W$  to consider the relative statistical importance of each observation type in the least squares solution, given that each measurements will be affected by different errors entity. Denoting the standard deviation of each measurement-type noise as  $\sigma_m$ , the weighing matrix will simply be  $W = \text{diag}(\sigma_m)$ . The normal equations (2.3.9) are modified as follows [32]:

$$H^T W H x = H^T W y \quad (2.3.15)$$

and (2.3.14) is modified accordingly, assuming the weights are constant overtime. Generally,  $H^T W H$  is denoted as  $\Lambda$ , the so-called information matrix, whereas  $H^T W y$  is simply indicated as  $N$ :

$$\Lambda x = N \quad (2.3.16)$$

Lastly, the state transition matrix  $\Phi$  must be solved for at each observation epoch and its components integration constitutes the heavy computational burden of the algorithm, consisting in 36 (6x6 elements) non-linear differential equation for a single satellite with the 6x1 state vector defined as in (2.3.1) coupled with the equations of motion. In the most general case, the equation to be solved is:

$$\dot{\Phi} = A(t)\Phi \quad (2.3.17)$$

with  $A$  defined in (2.3.6).

Although several analytical methods have been proposed to avoid the integration of  $\Phi$  as in [33],[34] and [35], these are only suitable for the keplerian unperturbed scenario or to consider a very limited number of spherical harmonics in the gravitational field potential. Further details on  $\Phi$  are given in appendix B.

### 2.3.2 Sequential estimation: the Kalman Filter

As anticipated, the least squares approach is not suitable for near-real-time applications due to its need of a time span for gathering the observables. Moreover, this approach requires the propagation of the state vector for the whole time span, which makes it highly sensitive to dynamical model errors. Several articles and books have been published exploring the mathematical nature and the different formulations of the sequential estimation algorithm, generally referred to as the Kalman filter,

including [36], [37] and [38]. Since the implemented algorithm for the LRNS is a batched least squares estimator as discussed in the following chapter, only little insight into the Extended Kalman Filter (EKF) technique is given hereafter.

With the weighting matrix  $W$  defined as in the previous paragraph, the inverse of the information matrix  $\Lambda$  is defined as the covariance matrix  $P$ :

$$P = \Lambda^{-1} \quad (2.3.18)$$

This matrix is directly correlated to the estimation error associated with  $x$ : considering only the position components in the state vector, the covariance matrix describes an ellipsoid of probability density around the expected value of the state vector, with the eigenvalues being the maximum deviations and the eigenvectors the orientation of the ellipsoid axes [39]. EKF is the formulation of the Kalman filter optimized for non-linear problems like the OD. Its main difference is the update of the reference trajectory after each observation processing, which implies reinitializing the dynamics differential equations at each new epoch. After the integration of the equation of motion and the state transition matrix, this latter is used to update the covariance  $P$  matrix at epoch  $t_i$ :

$$\bar{P}_i = \Phi(t_i, t_{i-1})P_{i-1}\Phi^T(t_i, t_{i-1}) \quad (2.3.19)$$

Then  $y$  and  $H$  are calculated as in (2.3.4) and (2.3.7) respectively and these informations are used to calculate the Kalman filter gain  $K_i$ :

$$K_i = \bar{P}_i \widetilde{H}_i^T (\widetilde{H}_i \bar{P}_i \widetilde{H}_i^T + W^{-1})^{-1} \quad (2.3.20)$$

Finally, the Kalman gain is used for the measurement and reference orbit update:

$$x_i = K_i y_i \quad X_i^* = X_i^* + x \quad P_i = (I - K_i \widetilde{H}_i) \bar{P}_i \quad (2.3.21)$$

Several studies were conducted on the effectiveness of the EKF for a wide variety of observables, including GPS signals [40], gravity gradients measured through a gravimeter [41] and for angles-only based OD [42], showing the feasibility and flexibility of the filter.

## 2.4 The Observables

"Orbit determination requires as input measurements that are related to the satellite's position or velocity. These data are collected by a satellite tracking system that measures the properties of electromagnetic wave propagation between the transmitter and the receiver. The transmitter as well as the receiver may either be

a ground station or a satellite" [28]. The choice of the observables to be used is a fundamental step in the design of a precise OD algorithm and must be traded-off with the system complexity, technology, costs and the mission constraints. The best theoretical solution usually does not coincide with the real scenario, which enhances the need of an accurate modelling of both the system dynamic and of the observables themselves that has to be compared with the ones generated on-board from the estimated reference trajectory.

An overview of the common observables used in the OD algorithms is hereafter presented and will serve as theoretical reference for the actually used measurement types for the case study, which will be discussed in the next chapter.

### 2.4.1 Range

One of the most used observables is the instantaneous range. This is defined as the magnitude of the relative position vector between a satellite and an instrument capable of performing this measure, which could be placed on another satellite, on a beacon or on any other element of both ground or space segment.

If  $(X, Y, Z)$  represents a generic reference frame<sup>2</sup>, and  $r_1, r_2$  are the position vector of the two elements involved in the measure, the ideal range is calculated as:

$$\rho = [(r_1 - r_2) \cdot (r_1 - r_2)]^{\frac{1}{2}} = [(X_1 - X_2)^2 + (Y_1 - Y_2)^2 + (Z_1 - Z_2)^2]^{\frac{1}{2}} \quad (2.4.1)$$

This definition though ignores some issues, including the finite speed of light and the instrumental errors.

Range-based measurements are in fact obtained through the concept of time-of-flight. Considering a one-way ranging measurement, that is, a signal is transmitted from a source to a receiver which directly uses this information without sending a signal back to the source like in two-way ranging, the time-of-flight can be related to the measured range as follows [25]:

$$\tilde{\rho} = c(T_R - T_T) + c(a_R - a_T) + c(b_R - b_T)(T - T_0) + \varepsilon \quad (2.4.2)$$

Where  $T_R$  and  $T_T$  are respectively the receiving and transmitting time<sup>3</sup>,  $a_R$  and  $a_T$  are constant offsets of the clocks from true time,  $b_R$  and  $b_T$  are the linear clock drifts with the time  $T$  with respect to a reference time  $T_0$  and  $\varepsilon$  represents all of the other errors.<sup>4</sup> Since the geometric true range  $\rho$  is only represented by the term

---

<sup>2</sup>The range is invariant under reference frame rotation being defined as a relative measure.

<sup>3</sup>Measured respectively in the receiver and transmitter time scale

<sup>4</sup>These may include second order drift components, stochastic errors and other unmodeled components.

$c(T_R - T_T)$ , the measured  $\tilde{\rho}$  is generally referred to as "pseudo-range". This is a more general definition also involving the clock modelling problem.

### 2.4.2 Range-Rate

The time variation of the range measurements can be used as an observable in the OD problem, conveying information about the relative velocity of the tracked object. It can mathematically calculated as:

$$\dot{\rho} = \frac{[(X_1 - X_2)(\dot{X}_1 - \dot{X}_2) + (Y_1 - Y_2)(\dot{Y}_1 - \dot{Y}_2) + (Z_1 - Z_2)(\dot{Z}_1 - \dot{Z}_2)]}{\rho} \quad (2.4.3)$$

Basically, this equation implies that the derivative of the range gives information about the relative velocity component along the relative position direction. An analogue description of the propagation and instrumental error as for the range can be introduced here.

In practice, the observable is generated through the Doppler-shift measurement of the radio signal sent to or from the spacecraft transponder.

### 2.4.3 Altimetric measurements

Another observable source is the on-board altimeter. This instrument emits an impulse, typically in the satellite nadir direction, which is then reflected by the surface of the orbited planet towards the satellite. The knowledge of the pulse emission and return times allows the processor to calculate the round-trip distance  $\rho$ , from which the altitude, simply calculated as:

$$h = \frac{\rho_{\text{round-trip}}}{2} \quad (2.4.4)$$

Where it can be shown that this definition yields results accurate to sub-millimeter level [25] regardless of the fact that the satellite has moved from the original emission position during the round-trip time.

### 2.4.4 Angles

Right ascension and declination data can be used for satellite tracking purposes. When it comes to measuring angles and angle-rates the Very Large Baseline Interferometry (VLBI) is the state-of-the-art technology, being much more effective than ranging and Doppler based observables [43][44].

This technique was originally born for radio astronomy purposes to overcome the limit of the maximum size of the antennas dishes diameter. In fact, once the wavelength is fixed, the angular resolution of the telescope only depends on the dish diameter. Linking antennas thousands of kilometers apart results in an extremely high sensitivity to the radio signals received from space, which is comparable to the one that would be obtained with an antenna whose dish diameter is equal to the LOS distance between the two antennas. Exploiting several stations around the globe it is possible to increase these performances even more, compensating for atmospheric delays and station clock offsets and instrumental group delays [43].

Considering the situation in Fig.2.2, it is clear that once the positions of the antennas are fixed in a chosen reference frame (thus the baseline length and orientation are known), it is possible to derive an angular measure of the source from the time-of-arrival difference between the two stations. This technique has successfully

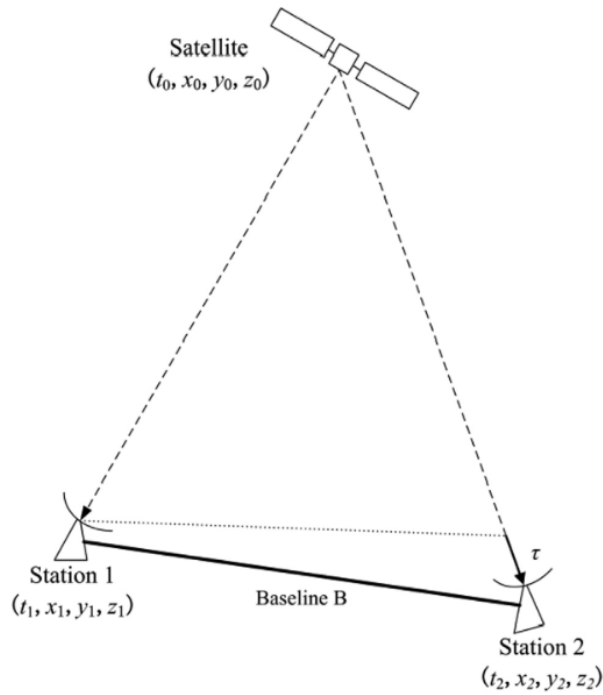


**Figure 2.2:** VLBI principle

been applied to several lunar and deep space satellite tracking operations including ESA's Smart-1 and Huygens probes, NASA's Mars Exploration Rover B and Cassini spacecraft [45].

## 2.5 Observability

As in [25], "The property of observability refers to the ability to apply an estimator to a particular system and obtain a unique estimate for all components of the state vector.". In the orbit determination context, if the problem is well-defined and the tracking sources are chosen accordingly, the state vector will be observable. Unobservability may arise both due to simplified dynamical models or ill-suited observables. An example of the former case can be found in [32] where two satellites using only ISL attempt to track each others. In the Keplerian two-body problem they are unable to fully determine their state vectors because the symmetry of the gravitational field: any couple of orbits generated from the real ones through a rotation of the orbital planes about the central body center of mass, i.e., varying the right ascension of the ascending node, would generate identical tracking data. Instead, the state vectors are fully observable on real perturbed halo orbits using only Satellite-to-Satellite Tracking (SST) data thanks to the asymmetries in the force field caused by the potential spherical harmonics and third body influence that make those trajectories unique. This concept is further explored in [46] and [47] for angles-only navigation using relative orbital elements.

From a mathematical point of view, the problem is not properly defined, hence the state is not observable, if the state-observations relation matrix  $H$  is rank deficient, having at least two linearly dependent rows. This causes the information matrix  $\Lambda$  to lose its positive definiteness thus leading to a non-unique least squares solution. Numerically, the state can be considered observable if  $cond(\Lambda) < 10^{16}$  [32]. Therefore, conducting an observability test can give insight into the effectiveness of the problem formulation and the validity of the observations choice.

## 2.6 The time synchronization problem

In 2.4.1 the satellite clocks offset problem was introduced through the concept of "pseudo-range". Once a time reference system is chosen, it is necessary to monitor the clock drifts of all the segments involved in the OD process and account for them in the state estimation. Satellite on-board clocks will always diverge from the station reference by some quantity, regardless of their precision: this is mainly due to their intrinsic stability, which is far more limited than that of the atomic ground-based clocks, but will also depend on other factors like relativistic effects. The use of one-way tracking techniques for deep space navigation is not feasible today because of these consistent drifts, which is the reason why technologies like

Deep Space Atomic Clocks (DSAC) and Chip Scale Atomic Clocks (CSAC) <sup>5</sup> are currently under massive studies and testing. Two-way ranging is conventionally used instead to eliminate the introduction of asynchronous clocks but it requires a dedicated ground network (like the DSN) to perform the Orbit Determination and Time Synchronization (ODTS), which is both cost and time consuming and may not always be available considering the ever increasing number of deep space missions.

Time synchronization is either performed through clock updating or as data post-processing [48]. The former case, used, for instance, to keep the GPS constellation time synchronized, consists in a correction sent to the satellite oscillator with respect to a certain ground-based time, while the latter involves removing deterministic frequency drifts and bias errors in the measurements associated to the incorrect time tags [49] and it is typically used for science data.

General relativity effects also come into place in the ODTS problem: a satellite orbiting a central body will have its on-board clock ticking faster or slower, depending on its altitude, with respect to an identical clock on the surface of the central body [50]. For instance, GPS satellites oscillators are set to a ticking frequency slightly lower than the 10.23 MHz nominal to account for this effect (around 10.229999999543 MHz) [25].

For the purpose of this work, the time synchronization problem was not taken into account considering the following assumptions:

- The clocks of the surface beacons are kept synchronized from Earth's ground stations
- Dual one-way ranging for ISL contacts is used, obtaining clock-free measurements. Indeed, several studies on precise orbit determination for GNSS constellations deal with this technology and point out its feasibility for this purpose, such as [51],[52] and [53]
- DSN stations perform two-way ranging with the satellites, eliminating the introduction of a clock error

In spite of the complexity of such a system, it was chosen to focus the study on the influence of different observables and mission architectures and scenarios on the orbit determination algorithm, leaving to further researches and work the implementation of a detailed time synchronization strategy.

---

<sup>5</sup>CSAC interest aroused parallel to the advanced satellite miniaturization, especially with CubeSats technology and their vast diffusion.

## **2.7 Other tracking error sources**

As anticipated, tracking data suffer from clock desynchronization and instabilities. The tracking equipment is also affected by random and systematic errors that arise from design trade-offs and physical limitations. The former errors are generally due to thermal noise, with a magnitude dependent on the equipment operating temperature [54] and can be modeled as white noise, while the latter are caused by instrumental delays and antenna multipath [43]. An accurate calibration of the tracking instruments [55] is important to assess biases entity and the expected noise levels of the measurements. This information can be used in the observations weighting process to exploit better data during the OD.

Imperfections in the satellite payload design contribute to tracking errors as well both with nominal distortions (i.e., acceptable deviations from design reference) and anomalous signal deformations [56], especially when the ISL contacts are used as ranging sources.

Inaccurate modelling of the tracking geometry, such as ground stations positions or Earth and Moon absolute and relative orientations due to precession and nutation motions, are also to be considered. For instance, in order to use VLBI techniques with the DSN/ESTRACK antennas, the baseline  $B$  vector as in Figure 2.2 must be precisely known. This vector though is not stationary and changes overtime by few centimeters per year because of Earth's crust movements and must therefore be continuously calculated and updated.

Furthermore, Earth's - or other central bodies' - atmosphere causes additional time offsets due to the refraction the signals experience travelling through a medium. On Earth, ionosphere and troposphere are the main causes of signals delay and they require precise modelling or the use of multiple frequencies or combination of observables to compensate for the errors that the dispersive propagation delay would introduce. Since these effect are strongly dependent on atmospheric conditions, they are very variable, with drifts that can reach up to an order of magnitude from the mean[43].

## Chapter 3

# Case study: orbit determination of a lunar satellite navigation system constellation

When it comes to lunar and deep space missions, the state-of-the art ODTS is still ground-based. As explained in chapter 1, infrastructures on the lunar surface are likely to become a reality in the next years and once present, they will be able to provide navigation and communication support, possibly leading to an autonomous network. Until then however, Earth-based ground tracking will be critical.

In the past decades, several OD techniques and tracking data have been used for lunar missions. In the early stages of lunar exploration the Rangers missions, that were meant to provide a full coverage of the Moon surface with high resolution images, were tracked with the DSN using L-band range-rates and angle measurements (these latter only in the first stages of the mission). The software used was the Single Precision Orbit Determination Program (SPODP), based on the Gauss' least squares method [57]. Later, the Apollo missions combined two-way and three-way Doppler and two-way range tracking with angular measurements primarily using the Manned Space Flight Network (MSFN), a set of tracking stations built for Gemini, Apollo and other manned missions which then merged into the DSN and the TDRSS [58]. These missions were among the firsts to use the Kalman filter technique to determine their trajectory and navigate.

In more recent times, the Lunar Reconnaissance Orbiter has mainly been tracked

since 2009 through NASA’s White Sands facility and the commercial Universal Space Network (USN) handling two-way Doppler and range measurements; LRO however is also equipped with the Lunar Orbiter Laser Altimeter (LOLA), which is able to provide altimetric data with a precision up to 10 cm, adding an important observable to the least squares based OD algorithm used by the GEODYN software selected for the mission [59]. The GRAIL spacecrafts were tracked using both two-way S-band Doppler and range data and one-way X-band Doppler with the DSN processed with the Jet Propulsion Laboratory (JPL) Monte software that used an EKF[60][61].

Planning for the next generation of Moon exploration, Korea Pathfinder Lunar Orbiter, scheduled for launch in 2022, is thought to use DSN and Korea Deep Space Antenna (KDSA) to provide two-way ranging measurements processed with an EKF [62], while the Chinese Chang’e-6 mission, planned for 2024, will likely exploit both the China Deep Space Network (CDSN) for range, range-rate and VLBI data, and image-based methods relying on precise Moon surface maps [63] [64]. Alongside, ESA’s plan consistency to use GNSS signals for lunar orbiters and for the Gateway navigation, as discussed in chapter 1, will be tested within the Lunar Pathfinder mission that will carry a highly sensitive receiver on-board. In the meantime, NASA will use the Cis-lunar Autonomous Positioning System Technology Operations and Navigation Experiment (CAPSTONE) 12U CubeSat to verify the stability of the planned Gateway NRHO [65] and test the effectiveness of the autonomous relative navigation through ranging measurements from the LRO [66] as based on [32] and [67].

In the next sections, a detailed overview of the simulated environment will be given, firstly describing the lunar navigation constellation hypothesized and the Moon inertial reference frame used, then analyzing the dynamical models, the observables considered and the algorithms used. This chapter is intended to exhaustively illustrate the procedures followed for the simulations, the scenarios, the hypothesis and the assumptions made that ultimately led to the results that will be displayed in the next chapter.

### **3.1 Satellite constellation**

An intern study was conducted by Thales on the advantages and drawbacks of several satellites configurations including Walker, ELFO and Halo constellations. Though both of these two latter have shown to be effective, ELFOs have been the subject of many internal ESA and industrial studies [4] and are, at present, the most likely to be used for a lunar navigation system. Therefore, the constellation

chosen for the simulation consists of four satellites in three ELFOs (fig.3.1).

The keplerian elements of the simulated satellites orbits are the following:

Param.	1	2	3	4
SMA(km)	9169.5	9172.4	9172.4	9149.6
i(°)	66.3	57.9	57.9	56.1
e	0.76	0.76	0.76	0.76
Arg.Per.(°)	88.9	97	97	84.1
RAAN(°)	89	335	335	208.37
TA(°)	350	360	328	352

**Table 3.1:** ELFOs keplerian elements

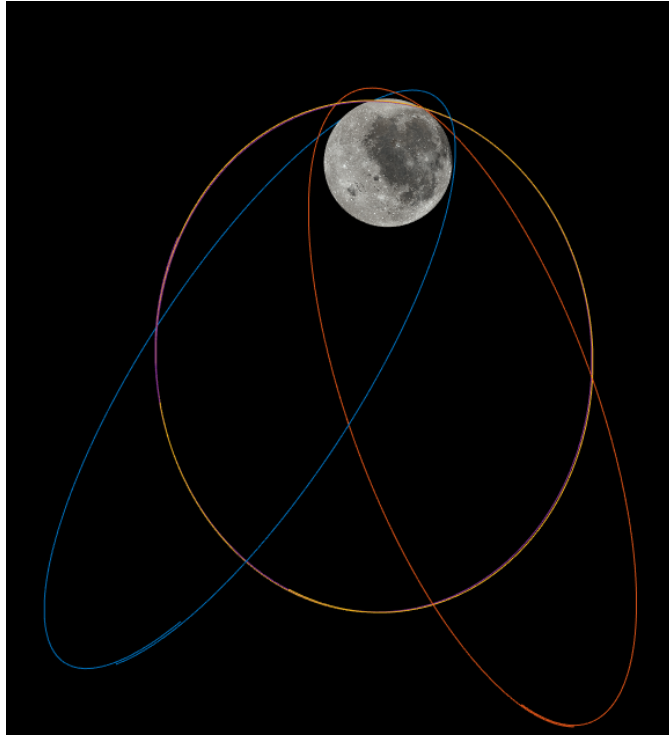


**Figure 3.1:** Simulated ELFOs at the initial epoch of the simulations

## 3.2 Reference frame

The reference frame used to describe the state vectors and the dynamics of the simulation is the Moon Inertial from AGI-STK. The Z-axis of this frame is the

International Astronomical Union (IAU) 2003 Z axis defined for the Moon through a constant rotation from the International Celestial Reference Frame (ICRF) [68]. The Inertial X-axis is along the direction of the cross-product of ICRF and IAU2003 Z-axes, evaluated at J2000 epoch. The Y-axis is accordingly to generate a right-handed coordinate system [69] (Fig.3.2) .

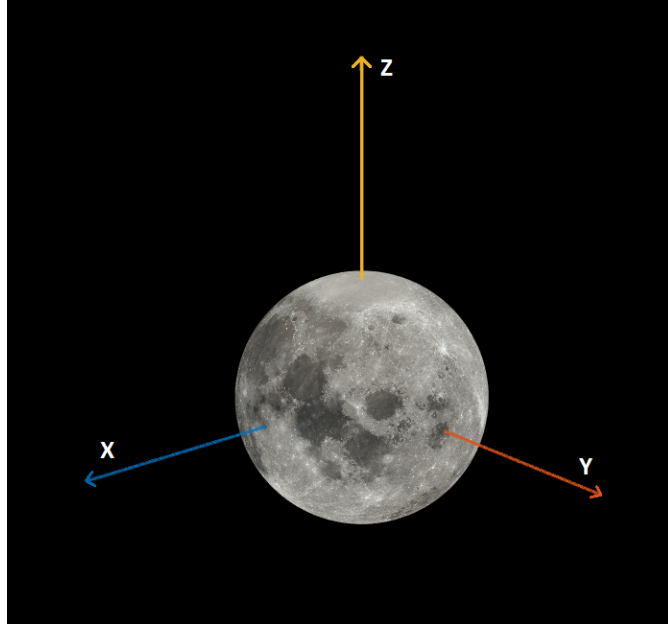


**Figure 3.2:** Moon Inertial Reference frame at simulation start epoch

### 3.3 The dynamical model

The lunar navigation constellation was simulated through STK. Both a pure Keplerian model and a perturbed one were used for the simulations, the former to assess preliminary performances and evaluate critical issues in the OD solution, like observability and noise-related effects, whereas the latter was used to analyze the OD performances in a more realistic environment. Some simulations were conducted assuming the dynamical model to be known (both Keplerian or perturbed) in order to assess the effect of noise and initial guess on the OD solution and to fine-tune some of the parameters and logic of the algorithm. Other simulations for real perturbed ELFOs assumed limited knowledge of the dynamical model and used a keplerian 2-body propagator with only third bodies and solar radiation pressure perturbation, without taking into account Moon's gravity field potential expansion in spherical harmonics.

### 3.3.1 Keplerian 2 Bodies

In this scenario, the orbits of the four satellites are periodic and constant overtime. The only acceleration experienced by the satellites is due to the lunar gravitational influence, with the Moon considered as a point mass and reduced to its Center of Mass(CoM). Each satellite follow an elliptical trajectory (fig.3.1) which model, recalling the state vector definition in (2.3.1) and the notation of (2.3.2), is simply:

$$\dot{X} = F(X, t) = \begin{bmatrix} V_x \\ V_y \\ V_z \\ -\mu \frac{x}{r^3} \\ -\mu \frac{y}{r^3} \\ -\mu \frac{z}{r^3} \end{bmatrix} \quad (3.3.1)$$

where  $r = \sqrt{x^2 + y^2 + z^2}$  is the instantaneous radius of the orbit, i.e. the distance of the satellite from Moon CoM at epoch t.

### 3.3.2 Real perturbed motion

The realistic perturbed ELFOs were generated through STK High Precision Orbit Propagator (HPOP) in the Moon Inertial reference frame. The following components of the total acceleration experienced by each satellite are taken into account:

- Moon point mass acceleration (Keplerian acceleration)
- Moon gravitational field potential asymmetries through spherical harmonics expansion up to 48x48 (degree x order) with coefficients from LP150Q JPL's model
- Earth and Sun third body perturbation (considered as point masses)
- Solar Radiation Pressure (SRP) with shadowing coefficient for eclipse

The perturbed orbits (fig.3.3) are no longer periodic but they exhibit a quite stable behaviour after a month of operations, showing their intrinsic stability, which is the main reason behind their choice for continuous South Pole coverage as discussed in Chapter 1.

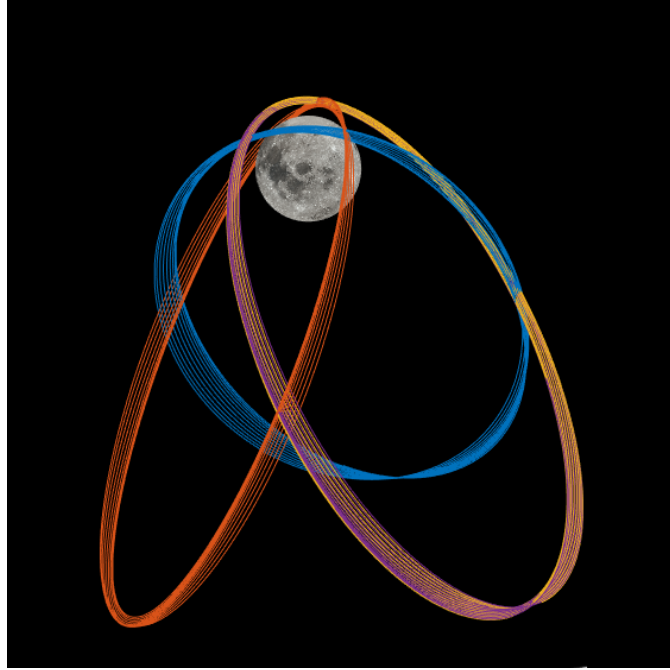


**Figure 3.3:** Perturbed ELFOs simulated for 10 days

### 3.3.3 The integration method

In both the Keplerian and the real perturbed cases, the Equations of Motion (EoM) and the state transition matrix were integrated through a Runge-Kutta-Fehlberg (RKF) method of order 7 with an error estimation of order 8 (RKF78). The integration routine is prompted with the Ordinary Differential Equations (ODE) to solve and their initial conditions, as well with integration times and a collection of setting parameters including fundamental physical constants of the Sun, Earth and Moon, LP150Q gravity model coefficients and the rotation matrix between Moon Inertial and Moon J2000 reference frames, this latter conveniently used to calculate some perturbation forces that will be later transformed into Moon Inertial. An integration tolerance of  $10^{-12}$  was selected after some preliminary tests as a trade-off between computational effort (i.e., simulation time) and divergence from true trajectory after long periods of observations gathering. The analysis presented in [70] was also considered as a reference for the tolerance choice. As expected, the major deviations from true trajectory due to integration limited precision were found in the perturbed case after 1 or 2 days of orbit prediction, which were necessary in few scenarios when limited observables were available to have an acceptable OD solution.

## 3.4 The observables

The line of work followed is the scaling of possible lunar navigation satellites orbit determination scenarios following ESA's roadmap. Whether or not GNSS signals could be used as fundamental observables or for augmentation, will be the object of upcoming missions; nevertheless, it was decided to simulate those signals as a source of observables for OD to achieve insights into the topic. Instead, DSN and/or ESTRACK antennas are most likely to be used for the initial phases of the Artemis program as they extensively proved to be feasible for such scenarios. These networks will also be the primary source of observables during the Trans-Lunar Injection (TLI). Furthermore, the spacecrafts will be equipped with a radar altimeter that could significantly improve OD performances as LRO's LOLA. In a more advanced mission phase the satellites will be able to communicate with each other providing additional range and range-rate data. The most pioneering architecture will make use of radio beacons on the surface of the Moon, which will likely be located near the South Pole, supplying the OD algorithm with very accurate tracking data of the satellites in view. Since the possibility of having a radio ranging source onboard the Lunar Gateway is yet to be confirmed, this observable source was not included in any scenario.

Hereafter, the assumptions and proceeding used to generate the different observables are presented with a particular focus on the determination of their availability overtime. In the last sub-sections the data rate hypothesized and the approach used for the simulation of measurement noise are explained.

### 3.4.1 DSN ranging

The first and most simple case considered is the one in which the only observables gathered are range and range-rate from the DSN antennas. Although ESTRACK stations are expected to be used as well for a lunar navigation system, only three DSN sites were used for the simulation, supposing the geometry of the OD problem would be similar in both cases thanks to the very large distance between the Moon and the Earth and the uniform antennas distribution. The DSN stations considered are reported in Table 3.2<sup>1</sup>:

As it can be noticed, the three deep space communication complexes are evenly spaced around the globe with roughly a 120° longitude separation in order to provide continuous communications at any time in any direction of space.

---

<sup>1</sup>Latitudes and longitudes are given with respect to the World Geodetic System of 1984 (WGS84)

N°	ID	Dish diameter	Location	Coordinates (Lat, Long)
1	DSS24	34m	Goldstone	35.20°, 243.70°
2	DSS34	34m	Camberra	-35.23°, 148.58°
3	DSS54	34m	Madrid	40.25°, 355.44°

**Table 3.2:** Simulated DSN antennas sites specifications

The scheduling of the tracking periods available for each satellite per week is complex and is currently generated a year in advance with allocations to the minute [71]. A conservative 8-hour-long single pass a week of tracking was preliminary considered to evaluate the DSN performances and then extended to 4 hours a day of double tracking passes based on previous missions [72] [73] [74], planned future orbiters [62] and DSN scheduling engine currently developed by NASA [75].

During these tracking periods the observables had to be furthermore filtered to consider three main effects:

- Earth Rotation, periodically changing the antennas in view from the Moon
- Moon occultation, precluding the radio link availability to the satellites crossing the lunar far side
- Minimum elevation angle above DSN antennas' horizon

In order to do this, two functions were defined. The first one is based on [76] (Figure 3.4) and is thought to be used to calculate the satellite-to-satellite visibility along the line of sight. Since the proceeding is purely geometric, and the distance between Earth and the Moon is much greater than the respective radii, this function was used to calculate satellite-to-Earth LOS visibility with respect to Moon occultation, considering Earth as a point mass (as it was another satellite) and the mean radius of the Moon equals to 1738km from STK. Earth position was calculated propagating the relative ephemerides from HPOP in the Moon Inertial reference frame. As in [76] the "Rise-set function" evaluates the following expression:

$$R = (\vec{r}_1 \cdot \vec{r}_2)^2 - r_2^2 r_1^2 + S^2(r_2^2 + r_1^2) - 2S^2(\vec{r}_1 \cdot \vec{r}_2) \quad (3.4.1)$$

The sign of R determines the visibility:

- $R < 0 \implies$  direct LOS communication
- $R > 0 \implies$  non-visibility

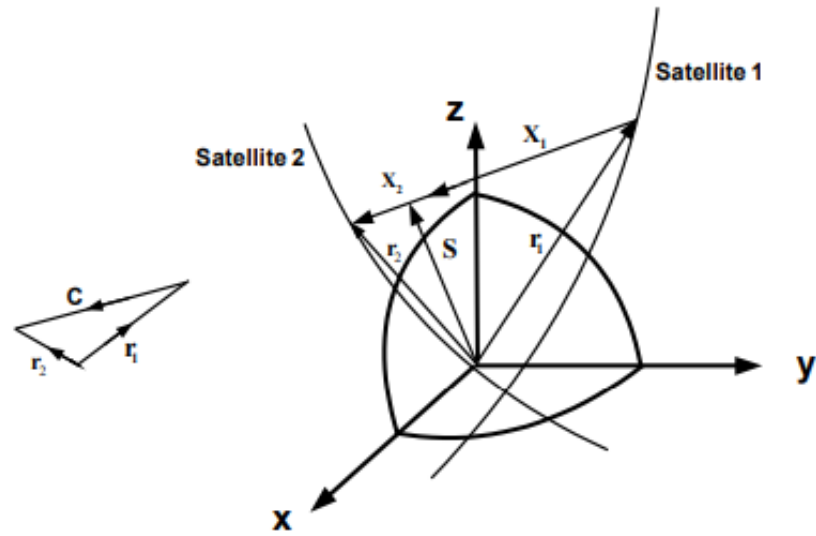


**Figure 3.4:** Satellite-to-Satellite LOS visibility

The second function calculates the elevation angle of the satellite with respect to the DSN antennas' horizon (Fig.xx). When the satellites dive under the horizon the observables are no longer available. The proceeding here is again purely geometric and the visibility criterion can be written as follows [77]:

$$\frac{(\Delta r \cdot r_s^0)}{\|\Delta r\|} \geq \sin\theta_0 \quad (3.4.2)$$

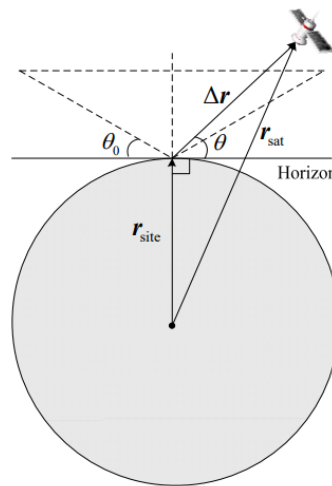


**Figure 3.5:** Antenna-to-Satellite LOS visibility

### 3.4.2 GNSS signals

If Lunar Pathfinder mission will be successful, GNSS signals could be used for navigation purposes in lunar orbit. Further technological demonstrations though will be required to assess the feasibility of this method even on the Moon's surface, where those signals are more likely to eventually serve as an augmentation system supporting the main observables from other sources because of the high positioning precision required for surface operations.

The possibility of exploiting GNSS signals comes from the pattern exhibited by the antennas of the satellites of those constellations [19]. Beside the main transmission lobe, which is clearly nadir pointing, the side lobes are always transmitting at some off-boresight angle (Figure 3.6, from [78]). Clearly, if the feasibility will be demonstrated, a fast-delivery navigation asset will be available for the Artemis program, which is the reason why it has been pointed out as a paramount resource for the Moon campaign since long [79].

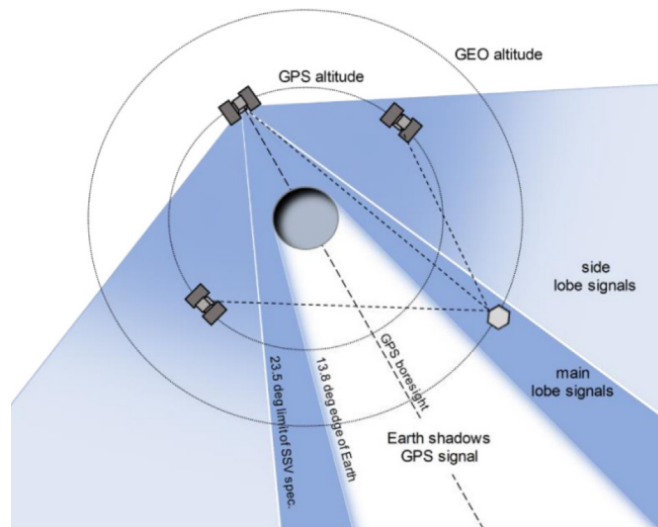


**Figure 3.6:** GPS satellite antenna 2D pattern from [78]

Since a precise modeling of the side-lobes was out of the scope of this work and it constitutes a massive topic for further studies, these assumptions were made:

- The GNSS signals were simulated as a single link for each lunar satellite with a point source placed in Earth's center of mass.
- Only range data can be inferred by these links (no range-rate)

### 3.4.3 On-board altimeter measurements

Each satellite of the lunar navigation system will almost certainly be equipped with an altimeter, whose measurements, together with a detailed map of the lunar surface, could be used as observables in the OD filter.

For the purpose of this preliminary study, a simplified altimeter model (Fig.3.7) was designed considering the Moon as perfectly spherical. This way, the single observations can be directly calculated from the norm of the position vector of each satellite and the radius of the Moon, thus giving a radial coordinate information. No informations on the latitude and longitude of the satellites can be inferred through this model because of the previous assumptions. As will be further explained, noise was added to simulate a more realistic environment, thus giving some insight into the effect of possible uncertainties in the morphological lunar surface model and instrument precision.

Altimetric measurements are assumed to be always available once the satellites are in lunar orbit hence no observation removal had to be performed since all the simulations do not involve the TLI phase.

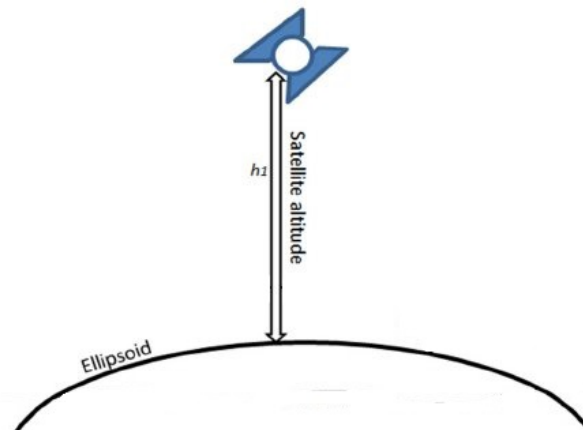


Figure 3.7: Satellite altimetric measure [80]

### 3.4.4 ISL measurements

The possibility of using cross-linking for navigation purposes has become a topic of high interest in the past recent years thanks to the improved autonomy it offers to the constellations in terms of both ODTS and as service channel for other purposes (e.g. distributing software updates for the spacecrafts in short periods [81]). An

inter-satellite link allows, for example, the indirect tracking of a spacecraft not visible from a ground station through ranging from a satellite in view of the station and relative positioning techniques. Moreover, as anticipated in section 2.5 from [32], an OD solution with ISL only has demonstrated to be effective for autonomous navigation in libration points exploiting the gravitational field asymmetries that generate unique orbits.

In the simulated environment of the present work, two dual one-way ISL ranging contacts were set to be available for each satellite when LOS visibility was not precluded by Moon occultation. The availability condition was calculated through the same rise-set function presented in 3.4.1 . A previous intern study by Thales preliminary investigated the comparison of cross-plane and in-plane ISL contacts geometries, showing better performances for the former case. Having three orbits and four satellites, the choice derived from this analysis was to link the two satellites in the same orbit with the two on the other planes to achieve the best geometry. A visualization of these contacts is given in Figure 3.7 with MATLAB:

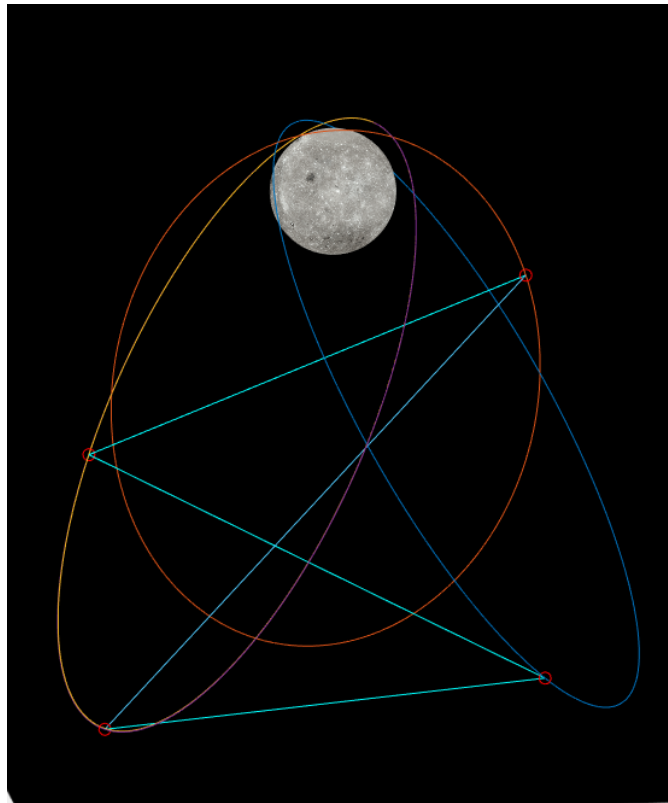


**Figure 3.8:** ISL ranging contacts

### 3.4.5 Lunar surface beacons ranging

A fully autonomous navigation system in the cis-lunar environment, namely a system which does not require ground support for the OD process, would require at least one beacon on the lunar surface. Actually, as will be clear from the simulation results in the next chapter, using only ISL and altimetric measurements other than beacon ranging requires 3 beacons to have a fully observable state vector at any epoch. This is mainly due to the poor geometry of the architecture which is limited by the need of having all the beacons positioned in the South Pole area.

An intern optimization study of three beacons positions was conducted prior to this work leading to the locations reported below in table 3.2, expressed in a Moon fixed frame which axes coincide with the Moon Inertial frame axes at the initial time of the simulation, which was set to 31 Aug 2020 11:00:00 UTC<sup>2</sup>:

N°	Latitude	Longitude
1	-88.91°	335.35°
2	-88.66°	295.96°
3	-88.75°	300.26°

**Table 3.3:** Optimized beacons' positions simulated

The ranging contacts with the beacon sites for each satellite are shown in Figure 3.8 below (from STK). The availability of the contacts was assessed through the procedure of Figure 3.5 used for DSN as well. In actual fact, the purely geometric considerations of (3.4.2) are immediately valid for this case, while for the DSN-based observables, re-elaboration had to be done since all the vectors are expressed in Moon Inertial while Figure 3.5 supposes to have them expressed in a reference frame fixed on the body where the antennas are located.

### 3.4.6 Data rate

At this stage of the ESA Moonlight initiative, technical specifications down to the data rate capability of the satellites are yet to be determined. This will clearly have an impact on both the OD performances and the computational effort of the on-board computers. Two data rates for the tracking informations were considered: 1 observable gathered per second or 1 observable gathered per minute. As will be further explained in the next chapter, while some scenarios don't benefit from a data rate as high as 1 observable per second, some others clearly show a performance

---

<sup>2</sup>I.e., Universal Time Coordinated

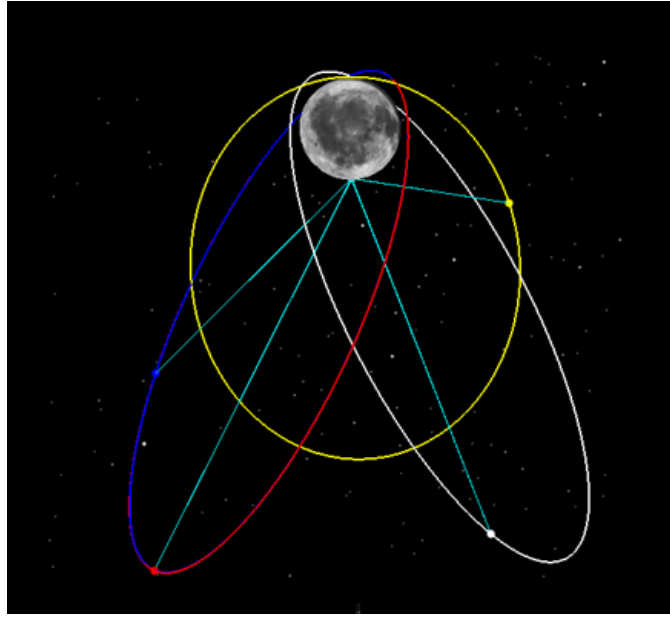


**Figure 3.9:** Satellite-to-beacons contacts

increase which has to be accounted for in a trade-off analysis considering the large amount of data that has to be stored with high data rates before computing the solution.

### 3.4.7 Simulation of measurement noise

The initial phase of this work dealt with perfect measurements. While this is helpful to preliminary evaluate observability and tune some algorithm settings like convergence criteria, some scenarios showed extreme influence even to limited measurement noise. This is the case when using only beacons as fixed point in the OD solution and noise is added on range measurements. While in the following chapter a detailed analysis of this phenomenon is carried out, the simulation of measurements noise is hereafter shown.

In order to stick with the formulation of the normal equations given in (2.3.15), it was assumed that the observation errors were independent and could be modeled as white noise. No biases like stations' location uncertainties were introduced in this preliminary analysis. MATLAB "Randn" function was used to generate the noise added to the observables at each epoch. This built-in feature produces normally distributed random numbers with mean zero and variance and standard deviation equal to one[82]. For the purpose of this work, the different standard deviations were introduced pre-multiplying the randn function output by a constant  $\sigma_{noise}$

value that was chosen for each observation type according to literature as [43],[28] and [25]. The weighting matrix in (2.3.15) becomes:

$$W = \begin{bmatrix} \frac{1}{\sigma_1^2} & & \\ & \ddots & \\ & & \frac{1}{\sigma_n^2} \end{bmatrix} \quad (3.4.3)$$

### 3.5 The implemented BLS orbit determination algorithm

Two algorithms based on the least squares approach were used in the simulations. The first one, hereafter presented, was the best performing after the introduction of measurement noise while the second, although showing very promising results for the advanced autonomous architectures with many observables available, did not deal well with observation noise and was not suitable for scenarios with limited observables.

This algorithm is based on the procedure described in the previous chapter from [25] with the addition of Orbit Prediction (OP) arches between two consecutive state estimates. For the initial guess, 3D errors of 180 meters for position and 1 meter per second for velocity were hypothesized, being the expected accuracy of the state vector knowledge at the lunar orbit insertion epoch. Several time spans to collect observables before computing the OD solution were considered and compared to understand advantages and drawbacks of long arches lengths.

The orbit prediction arch after the state estimation is as long as the time span of observables gathering and the more accurate the dynamical model is, the better the performance of this prediction are in terms of deviations from true trajectory. Clearly, the state estimate must be accurate enough as well for this technique to allow precise OP and the arches length should be limited in order to have a better initial guess for the next OD arch: in fact, not only the orbit is predicted until the following initial arch epoch, but the same reference trajectory is used in the first iteration of that arch before the first state deviation  $x$  correction. Therefore, the OP phase properties both influence the current OD arch performances (strongly) and the following arch ones (relatively).

The purpose of the orbit prediction is to lighten the computational load on the processor that will eventually execute the OD algorithm while still maintaining precision, providing a fast and reliable solution that will eventually be used by the

lunar users to determine their own position, which is the ultimate goal of a lunar navigation system.

Concerning the stopping condition for the BLS algorithm, two convergence criteria were found to be suitable and were applied simultaneously. The first one is based on the Root-Mean-Square (RMS) variation, the second on the state deviation vector norm.

The RMS of the observation residuals is defined as:

$$RMS = \left[ \frac{\sum_{i=1}^l \epsilon_i^T \epsilon_i}{m} \right]^{0.5} \quad (3.5.1)$$

where  $\epsilon_i$  is the observation residual at epoch  $i$  as defined in (2.3.5) and  $m$  is the total number of observables gathered in the considered arch.

More precisely, the RMS as defined in (3.5.1) is named unweighted RMS, as opposed to the weighted RMS which considers each measurement weight, substituting  $\epsilon_i^T \epsilon_i$  with  $\epsilon_i^T W \epsilon_i$  in the numerator. If the BLS is converging to a solution, the RMS converges as well either to 0 for unweighted RMS or to 1 for the weighted case. [83]. The fractional change between the RMS values of successive iteration can thus be used as a convergence condition. The implemented algorithm uses the unweighted RMS as first convergence criterion and poses the RMS variation threshold at 0.03, a trade-off value between the number of iterations and the OD solution precision that was found to be feasible for the present BLS after some preliminary trials and considerations.

The second convergence condition is based on the norm of the state deviation vector  $\|x\|$ . If the BLS processor is converging, the norm of this vector, ultimate solution of the algorithm, would tend to zero, meaning no further corrections have to be applied to the estimate. A threshold of  $10^{-8}$  was set to  $\|x\|$  as stopping condition.

Since the two criteria both check for convergence but differently and since each of them would be satisfying in itself, it was decided to impose them simultaneously to look for the least iterations number. In every considered scenario, algorithm convergence occurred within 4 iterations.

In order to preliminary assess the correct processing of the algorithm two tests were conducted. Firstly, an initial guess equal to the true trajectory was used to initialize the algorithm and perfect observables were given to the processor. As expected, a single iteration was performed leading to a null state deviation vector, since no correction had to be made on the initial guess. Another test was performed

as suggested in [55], prompting the algorithm with single inaccurate components of the initializing reference trajectory. The BLS processor correctly returned an  $x$  value with corrections only on single mistaken components. The algorithm logic flow is as hereafter presented:

---

**Algorithm 1** BLS algorithm logic flow.

---

```

1: Initialize variables
2: ▷ i=1                                     ▷ Counter is reset
3: ▷  $t_{i-1} = t_0$                            ▷ Time is set to initial epoch
4: ▷  $X^*(t_{i-1}) = X_0^*$                        ▷ Reference orbit is set to initial guess state vector
5: ▷  $\Phi(t_{i-1}, t_i) = \Phi(t_0, t_0) = I$      ▷ State transition matrix is set to identity
6: ▷  $\Lambda = 0, N = 0$                          ▷ Normal equation matrices are reset
7: Integrate equation of motion and  $\Phi$  from  $t_{i-1}$  to  $t_i$ 
8: ▷  $X^*(t_i) \leftarrow \dot{X}^* = F(X^*(t), t)$    ▷ With EoM initial condition  $X^*(t_{i-1})$ 
9: ▷  $\Phi(t_i, t_0) \leftarrow \dot{\Phi}(t, t_0) = A(t)\Phi(t, t_0)$    ▷ With initial condition  $\Phi(t_{i-1}, t_0)$ 
10: Accumulate current observables
11: ▷  $y_i = Y_i - G(X_i^*, t_i)$                  ▷ Observation deviation vector
12: ▷  $\bar{H}_i = [\partial G(X, t_i) / \partial X]^*$        ▷ State-observable relation matrix at epoch  $t_i$ 
13: ▷  $H_i = \bar{H}_i \Phi(t_i, t_0)$                  ▷ Mapping back H to  $t_0$ 
14: ▷  $\Lambda = \Lambda + H_i^T W_i H_i$            ▷  $\Lambda$  update
15: ▷  $N = N + H_i^T W_i y_i$                    ▷ N update
16: if  $t_i < t_{final}$  then
17:      $i = i + 1$                                ▷ Check for maximum batch length
18:     Back to 10                                 ▷ Extend the batch of observables
19: else if  $t_i \geq t_{final}$  then
20:      $x \leftarrow \Lambda x = N$                  ▷ Solve normal equations
21:      $X^*(t_0) = X^*(t_0) + x$                  ▷ Update reference trajectory
22: end if
23: Check convergence criteria
24: if  $dRMS > threshold$  or  $\|x\| > threshold$  then
25:     Back to 1                                 ▷ Restart process with new initial guess
26: else if Convergence criteria are met then
27:     Integrate state vector from  $t_0$  to  $t_{final}$    ▷ Orbit prediction
28:      $t_0 \leftarrow t_{final} + 1$              ▷ Initialize new OD arch
29:     Back to 1
30: end if

```

---

### 3.6 The instantaneous least squares solution

A general rule of thumb when dealing with batched least squares algorithm would tell that the more data are available, the more precise the OD solution would be. While this is generally the case thanks to both a better normal equations conditioning and an averaging of measurements noise effects overtime, the longer the time span to collect observables, the less precise the propagation through the dynamical model would be as discussed in the previous section. For this reason, when a sufficient number of observables is available, it is theoretically possible to use the standard least squares approach as a sequential estimator.

First of all, for the present case study, the state vector comprises 24 components (6 per satellite), therefore at least 24 observables are needed to calculate an instantaneous solution. In the next chapter, the scenarios where this was the case are specified. In actual fact, due to the constellation geometry, the moments when sufficient observables are available are anyways limited - with a single scenario exception - to the time spans when the satellites are all in view of the surface beacons and of each other. As a matter of fact, considering a mission architecture composed of 4 satellites using ISL and lunar beacons to determine their position, this is intuitively true: when a satellite has no longer direct LOS communication with beacons and other spacecrafts, trying to determine its position instantaneously is clearly impossible.

It would actually be possible to use the minimum norm criterion [25] to give an estimation of the state vector with less than 24 measurements imposing the minimization of  $x$  under the constraint (2.3.4), i.e.,  $\epsilon = 0$  and that would yield:

$$x = H^T(HH^T)^{-1}y \quad (3.6.1)$$

with the same notation as in the previous chapter. This problem is generally ill-conditioned though and does not result in a feasible OD solution.

The BLS algorithm can thus be modified simply checking for the number of observables at each epoch and solving instantaneously if there are at least 24 measurements or collecting batches of data and solve as the previous algorithm when observables are lacking. Attention was paid to the superposition of these two procedures, because the BLS requires to have a sufficient large batch of data and must not be interrupted before this minimum time span to solve with instantaneous algorithm even if after some epoch a larger set of observables was again available.

As anticipated, this algorithm was used in the first stages of the work but soon discarded due to extreme sensitivity to measurement noise effects. This will be

made more clear in the next chapter exposing the results. In further sections this algorithm will also be referred to as the "mixed algorithm", since it alternates instantaneous OD solutions and batched ones, while the former algorithm, the batched least squares, will be also referred to as the "long-arch algorithm". The algorithm logic flow is presented in the next page.

### 3.7 Errors calculation

When it comes to orbit determination performances, several strategies can be followed to assess the rightness of the implemented algorithms. For instance, the covariance matrix  $P$  as defined in (2.3.18) is generally used to evaluate the effectiveness of the least squares fit. While this is a standard procedure, the most important aspect of the solution to be evaluated is, in the end, the 3D error:

$$err_{3D} = \sqrt{(x - x_{true})^2 + (y - y_{true})^2 + (z - z_{true})^2} \quad (3.7.1)$$

where  $[x, y, z]$  is the position vector of one satellite as calculated through the OD algorithm and  $[x_{true} y_{true} z_{true}]$  is its true position vector.

This is a general performance parameter whose definition as expressed above would still be valid once the clock error is introduced, since it is just a geometric difference. For this reason, it is the performance indicator used in this work to assess the quality of the orbit determination.

The final service purpose of a lunar navigation system will be to support the navigation in lunar environment. While the 3D error is revelatory of the OD performances, it does not give insight into the final user PNT accuracy. Since the clock error was not taken into consideration into this work and too many assumptions would have had to be made to calculate an equivalent Signal In Space Error (SISE) with some significance, it was decided not to use this metric in the performance evaluation. In the interest of providing fuller information, the SISE is defined in [84] as the instantaneous difference in time and position between the true satellite state and the calculated one from the broadcasted navigation message, projected onto the user-satellite direction. As it is a key performance indicator of all navigation systems [85], further studies will have to analyze the problem in detail for the specific lunar satellite navigation constellation case.

---

**Algorithm 2** Instantaneous least squares logic flow.

---

```

1: Initialize variables
2: ▷ i=1                                     ▷ Counter is reset
3: ▷  $t_{i-1} = t_0$                            ▷ Time is set to initial epoch
4: ▷  $X^*(t_{i-1}) = X_0^*$                        ▷ Reference orbit is set to initial guess state vector
5: ▷  $\Phi(t_{i-1}, t_i) = \Phi(t_0, t_0) = I$      ▷ State transition matrix is set to identity
6: ▷  $\Lambda = 0, N = 0$                        ▷ Normal equation matrices are reset
7: Integrate equation of motion and  $\Phi$  from  $t_{i-1}$  to  $t_i$ 
8: ▷  $X^*(t_i) \leftarrow \dot{X}^* = F(X^*(t), t)$    ▷ With EoM initial condition  $X^*(t_{i-1})$ 
9: ▷  $\Phi(t_i, t_0) \leftarrow \dot{\Phi}(t, t_0) = A(t)\Phi(t, t_0)$    ▷ With initial condition  $\Phi(t_{i-1}, t_0)$ 
10: Accumulate current observables
11: ▷  $y_i = Y_i - G(X_i^*, t_i)$                  ▷ Observation deviation vector
12: ▷  $\tilde{H}_i = [\partial G(X, t_i)/\partial X]^*$        ▷ State-observable relation matrix at epoch  $t_i$ 
13: if obs≤24 then
14:   ▷  $H_i = \tilde{H}_i\Phi(t_i, t_0)$                  ▷ Mapping back H to  $t_0$ 
15:   ▷  $\Lambda = \Lambda + H_i^T W_i H_i$            ▷  $\Lambda$  update
16:   ▷  $N = N + H_i^T W_i y_i$                    ▷ N update
17:   if  $t_i < t_{final}$  then
18:      $i = i + 1$                                ▷ Check for maximum batch length
19:     Back to 10                                 ▷ Extend the batch of observables
20:   else if  $t_i \geq t_{final}$  then
21:      $x \leftarrow \Lambda x = N$                  ▷ Solve normal equations
22:      $X^*(t_0) = X^*(t_0) + x$                  ▷ Update reference trajectory
23:   end if
24: else if obs≥24 then
25:   ▷  $\Lambda = H_i^T W_i H_i$                    ▷ No mapping back is required here
26:   ▷  $N = H_i^T W_i y_i$ 
27:    $x \leftarrow \Lambda x = N$                  ▷ Solve normal equations
28:    $X^*(t_i) = X^*(t_i) + x$                  ▷ Update reference trajectory
29: end if
30: Check convergence criteria
31: if  $dRMS > threshold$  or  $\|x\| > threshold$  then
32:   Back to 1                                     ▷ Restart process with new initial guess
33: else if Convergence criteria are met then
34:   if obs≤24 then
35:     Integrate state vector from  $t_0$  to  $t_{final}$    ▷ Orbit prediction
36:      $t_0 \leftarrow t_{final} + 1$              ▷ Initialize new OD arch
37:     Back to 1
38:   else if obs≥24 then
39:      $t_0 \leftarrow t_{final} + 1$            ▷ If the solution is instantaneous just read the next
    observation
40:     Back to 1
41:   end if
42: end if

```

---

# Chapter 4

## Simulations results

The results of the simulated architectures are presented hereafter following from the aforementioned assumptions and hypothesis made and the constellation geometry and OD algorithm selected for the case study. The different mission scenarios are presented with an increasing level of complexity and autonomy. Data rates and different measurements accumulating times are compared, as well as observables availability and keplerian and perturbed models.

As expressed in section 3.7, the 3D error is the key performance parameter chosen, so most of the graphics in this chapter will display its trend for both position and velocity.

### 4.1 DSN-only tracking

In this first mission scenario the simulated DSN antennas of Table 3.2 are used as the only ranging source available. The measurement noise standard deviation used for the simulations are  $\sigma_{range} = 0.6m$ ,  $\sigma_{range-rate} = 0.03mm/s$ . A detailed explanation of all other assumptions and models is made in chapter 3 and particularly in section 3.4.1 where the reference for noise levels is reported as well.

For the 8-hours-a-week tracking window two time span cases for the OD algorithm were contemplated: in the first one, one single window of tracking was considered and the state estimate propagated for 4 days, while in the second case, two 8-hours windows from consecutive weeks were used to solve for the initial constellation state which was then propagated till the last time of observation. For the 4-hours-a-day windows instead, time spans of one to three days were considered with a total 6 days of simulations. The simulated ELFOs are Keplerian unperturbed.

### 4.1.1 8-hours-a-week tracking

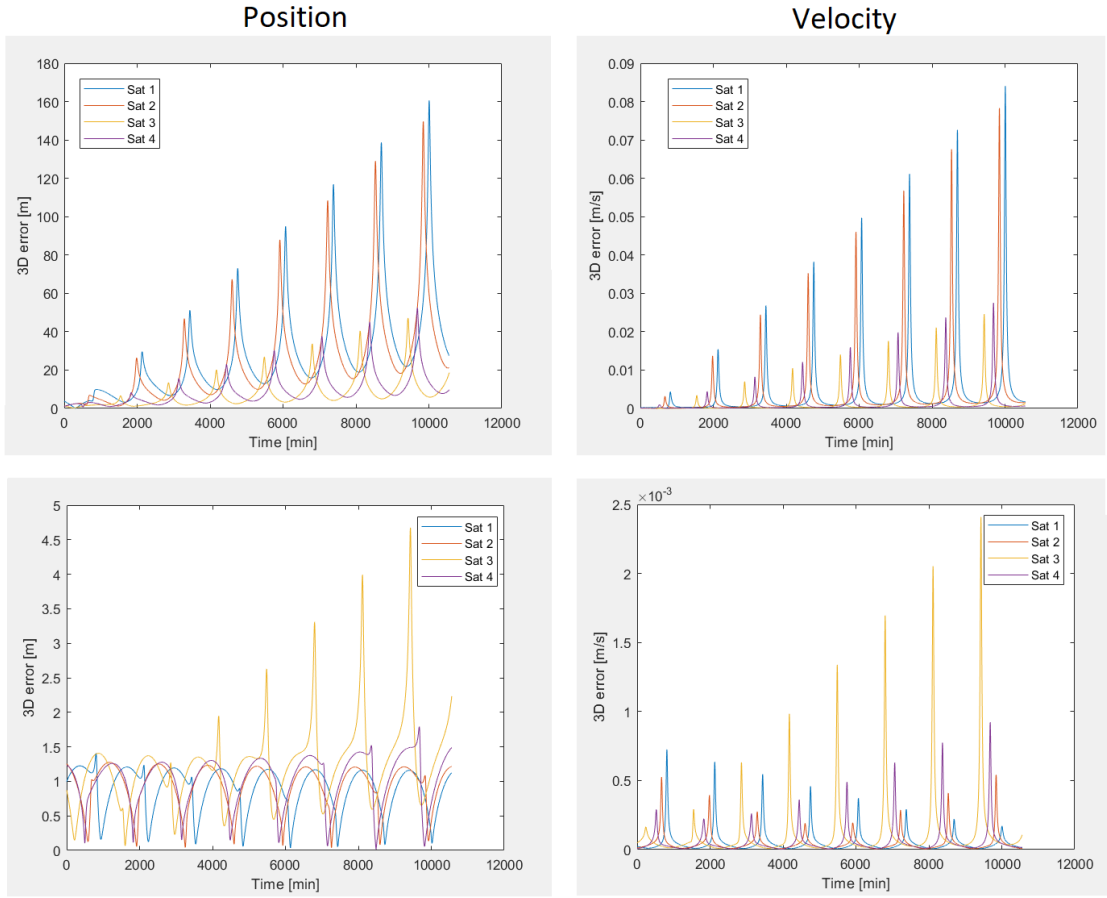


**Figure 4.1:** 3D position (left) and velocity(right) error for DSN only case with 8-hours of tracking for 1 and 2 windows from top to bottom respectively

As the graphs above illustrate, a single 8-hour tracking window does not yield an accurate initial state estimate, with the successive orbit prediction phase progressively diverging from the real one. Using two tracking windows dramatically increase the performance of the OD algorithms: a sufficient time span allows the geometry of the orbit to change enough to provide diversified measurements that translate into a better conditioned least squares problem. In spite of the consistent error in the initial guess, in the Keplerian problem the divergence of the reference trajectory from true trajectory does not cause the algorithm to fail even after a week of orbit prediction. This may be due to the periodicity that the reference trajectory has in the keplerian problem, resulting in a closed trajectory. As later demonstrated, prediction arches this long are not feasible in the real perturbed case.

### 4.1.2 4-hours-a-day tracking

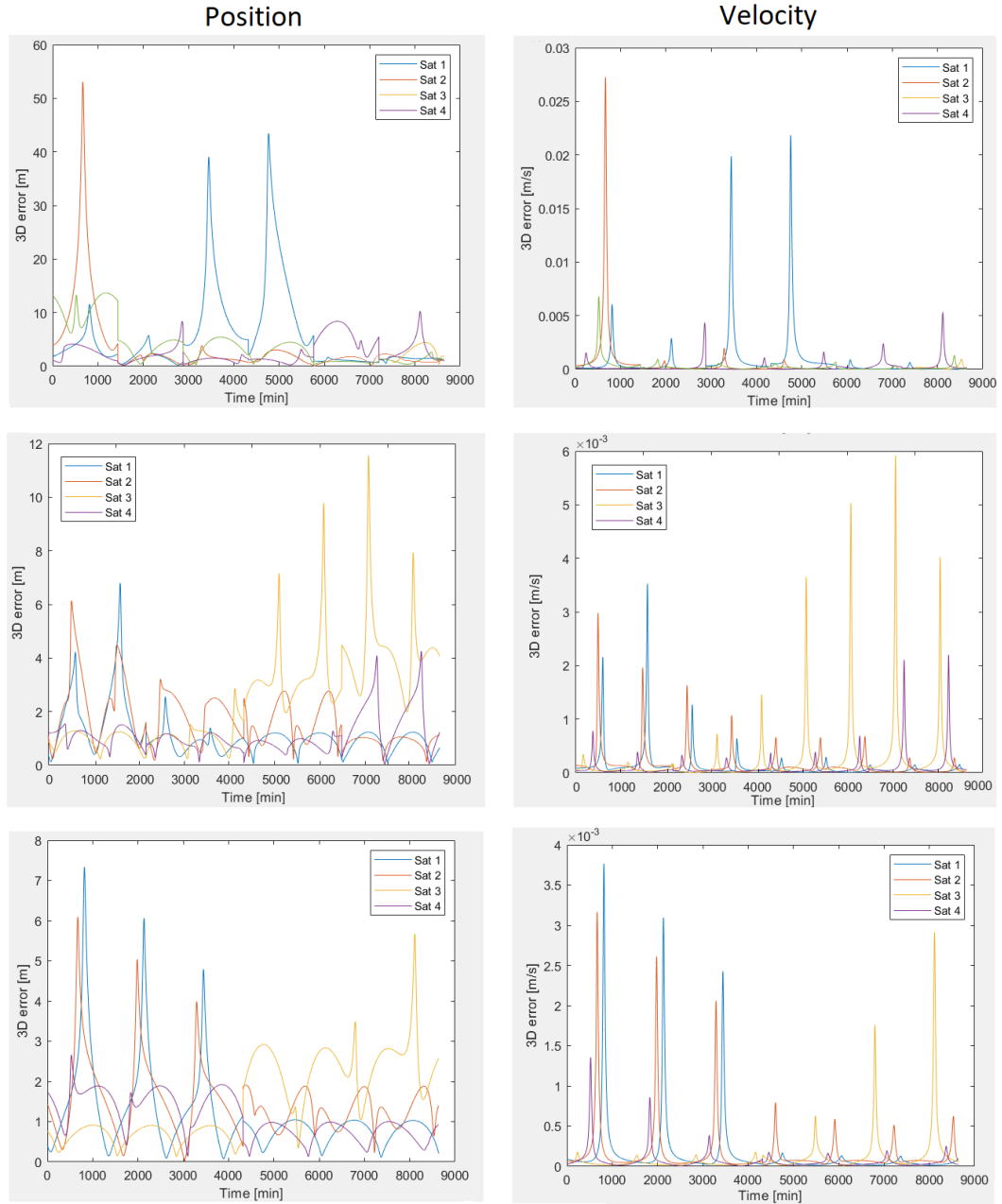


**Figure 4.2:** 3D position (left) and velocity (right) error for DSN only case with 4-hours windows of tracking for 1, 2 and 3 days of time span from the top to the bottom respectively

As Figure 4.2 demonstrate, in the Keplerian problem, DSN-only tracking shows good results both in terms of position and velocity estimate when more than a single window is used. The more the tracking windows, the better the state estimation and successive orbit prediction. Nevertheless, a common trend both in the 4-hours and 8-hours windows can be seen: while some trajectories tend to get closer to the real orbits, others tend to diverge the further the orbit prediction extends. This is both true for positions and velocity.

A comparison of the observables availability between the 4-hours and 8-hours windows cases is shown in Figure 4.3 below for a 7 days exemplary period. The maximum number of measurements available simultaneously is 16, meaning that the geometry of the problem allows two separate DSN antennas to be in view of the lunar navigation satellites at the same time.

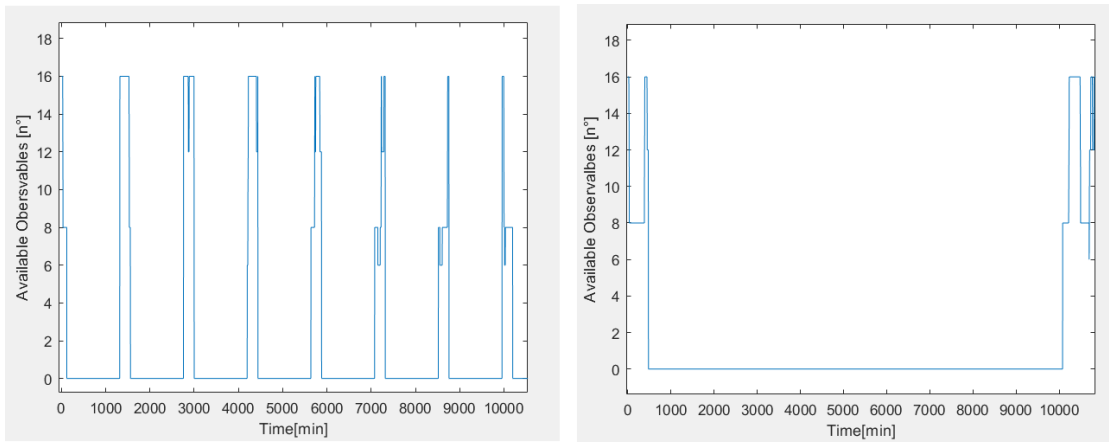


**Figure 4.3:** Observables availability for 4-hours-a-day windows (right) and 8-hours-a-week (left)

3D error		Position [m]		Velocity [mm/s]	
Windows	Time Span	Mean	Max	Mean	Max
8 Hours	1 day	20.25	160.62	2.41	85.2
	7 days	1.03	4.68	0.09	2.4
4 Hours	1 day	7.35	53.95	0.78	27.5
	2 days	2.12	11.56	0.18	5.9
	3 days	1.31	7.34	0.13	3.8

**Table 4.1:** 3D position and velocity errors resume for the DSN-only scenario

Table 4.1 above resumes the 3D errors for this scenario. The mean and maximum

errors are intended as for the overall constellation, meaning that the former is the arithmetic mean of the single error means of each satellite, while the latter is simply the largest error that occurs in the whole OD solution. This definitions will be used for all the results of the following sections.

An important aspect to point out is that the apparent contradiction of having a much greater error in the 1-day 8-hours tracking window with respect to the 1-day 4-hours, is due to the fact that after the first day of orbit prediction, in the former case no additional observables are gathered since there is only one tracking window per week, so the error keeps raising in the next days, while in the latter case, as the successive day starts, 4 more hours of measurements from DSN are available and update the state estimate.

## 4.2 DSN and altimeter

The lunar navigation satellites will have an on-board altimeter as anticipated in section 3.4.2. No availability issues arise for these additional measurements, as they are supposed to be always obtainable. Therefore, the number of maximum observables simultaneously available increases to 20: 16 from the DSN and 4 from the on-board altimeters. At the same time, even when the DSN is not supporting the tracking, the altimeters can collect measurements to be used when the DSN is once more available, thus the minimum number of observables at any time, is 4.

The same noise level as the previous scenario are used, with the addition of the altimeter measurement noise level set to  $\sigma_{range} = 0.1m$  as for LRO's LOLA [59].

As in the DSN-only architecture, the two different tracking windows of 8 and 4 hours were considered to give a comparison. This time though, because of the poor results obtained with the DSN for a single 8-hour tracking window, this case was discarded. Instead, two 8-hours windows in consecutive weeks were simulated to solve for the initial state and the result propagated for 5 days. For the 4-hours-a-day windows, 2 days, 3 days and 7 days of time span were considered for comparison.

The simulated ELFOs are keplerian unperturbed as in the previous scenario.

### 4.2.1 8-hours-a-week-tracking

From Figure 4.4 below it is clear that the addition of the altimeter yields very accurate results both in position and velocity estimation and successive orbit prediction, even with only two 8-hours tracking windows. The drawback though is

that at least 1 week of measurements is required to get this results, which may not be suitable for the lunar navigation system satellites if more frequent trajectory updates have to be made to plan for maneuvers, support of critical operations and manned missions.

Both position and velocity exhibit periodic oscillations, possibly indicating an accurate semi-major axis estimate, thanks to the radial information provided by the altimeter, and a slight eccentricity deviation, or a mean anomaly constant offset which brings the calculated trajectory closer to the real one every time the aposelene is reached. In fact, the oscillations period is roughly the same of the period of the ELFOs, which is around 24h.

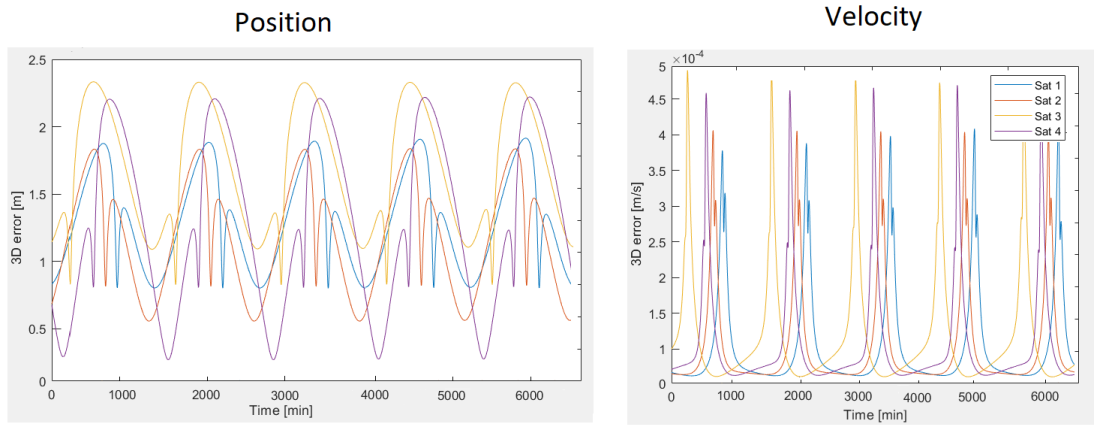


**Figure 4.4:** 3D position (left) and velocity (right) error for DSN and altimeter scenario with two 8-hours windows of tracking

### 4.2.2 4-hours-a-day-tracking

In Figure 4.5 below, a similar trend to the DSN-only case is exhibited. As in the 8-hours tracking windows though, with 4-hours windows the tendency to diverge is no longer present. Again, the more the time span, the better the results. For the 7 days time span, similar results to the 8-hours case are reached though gathering much more observables, meaning there is no advantage in having such frequent tracking when solving for the initial state only after one whole week. Instead, the positive aspect of the 4-hours windows is that accurate orbit update can be made as frequently as every 3 days.

The same oscillation pattern of Figure 4.4 can be seen in 4.5 in the bottom

left image, indicating the consistency of the geometric considerations aforementioned after the same time span even with more tracking windows.

In Table 4.2 the summary of the mean and maximum constellation 3D errors is reported.

3D error		Position [m]		Velocity [mm/s]	
Windows	Time Span	Mean	Max	Mean	Max
8 Hours	7 days	1.38	2.35	0.11	0.5
4 Hours	2 days	3.32	18.69	0.21	2.05
	3 days	2.99	7.44	0.18	1.21
	7 days	1.39	2.39	0.11	0.49

**Table 4.2:** 3D position and velocity errors resume for the DSN and altimeter scenario

### 4.3 Lunar beacons, ISL and altimeter

Going towards a dedicated Lunar PNT system, as in ESA’s roadmap, will require a decrease in Earth-based support and an increase in the number of observables directly available in lunar environment. As mentioned in chapter 1, using ISL will be necessary to have sufficient measurements for orbit determination purposes. Moreover, the beacons placed on the Moon’s surface will provide a fixed reference in the OD algorithm thanks to constant and accurate knowledge of their position.

#### 4.3.1 Preliminary simulations: insight into observability and noise with mixed algorithm

Several key informations were deduced from the preliminary simulations for the architecture with beacons and ISL. The first insight was about observability: while two beacons and two ISL contacts per satellite are theoretically sufficient to allow the use of the instantaneous LS algorithm presented in section 3.6, providing 24 observables when all the spacecrafts are in view of each other and of the beacons, the state vector was found to be unobservable with this architecture. Indeed, even without observation noise, the algorithm would not yield accurate results and had to be adjusted to handle a non-positive definite  $\Lambda$  matrix<sup>1</sup>. The algorithm also

---

<sup>1</sup>The implemented least squares algorithm uses the Cholesky decomposition of the positive definite  $\Lambda$  matrix to obtain a numerically efficient result, but this is only possible when the

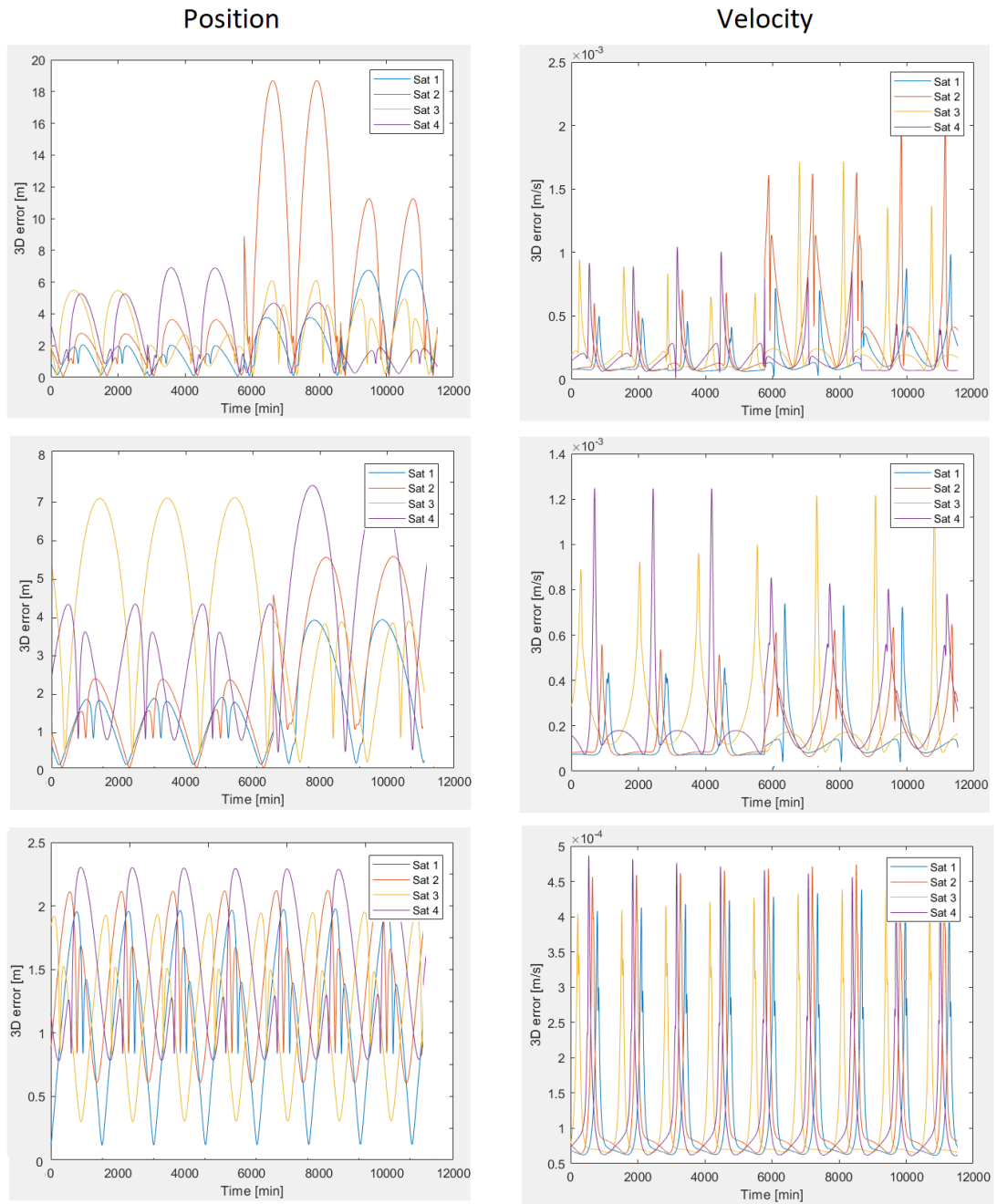


**Figure 4.5:** 3D position (left) and velocity (right) error for DSN and altimeter scenario with 4-hours windows of tracking for 2, 3 and 7 days of time span from the top to the bottom respectively

displayed a strong influence on the initial guess under these conditions, particularly when increasing the error on the velocity.

Figure 4.6 below shows the conditioning number trend of  $\Lambda$  for two days of simulation of the above mentioned 2 beacons and ISL architecture, and compares it with the availability of the whole set of observables: value 0 means it is not possible to calculate the position instantaneously, value 1 means that all 24 measurements are available and the state deviation is computed with only the observables collected at that epoch. It is clear that the least squares problem is much worse conditioned when all satellites are in view of the beacons and of each other. While this may come unexpectedly at first glance, it is actually coherent with the unobservability of the state vector:  $H$  being not full rank makes  $\Lambda$  non positive definite and thus ill conditioned for solving the least squares linearized system; instead, collecting measurements for long periods improves observability and continues to allow orbit determination exploiting ISL to provide a relative measurements when one satellite is no longer in view of the beacons. As a reminder, it was pointed out in section 2.5 that, numerically, the state can be considered observable if  $cond(\Lambda) < 10^{16}$ .

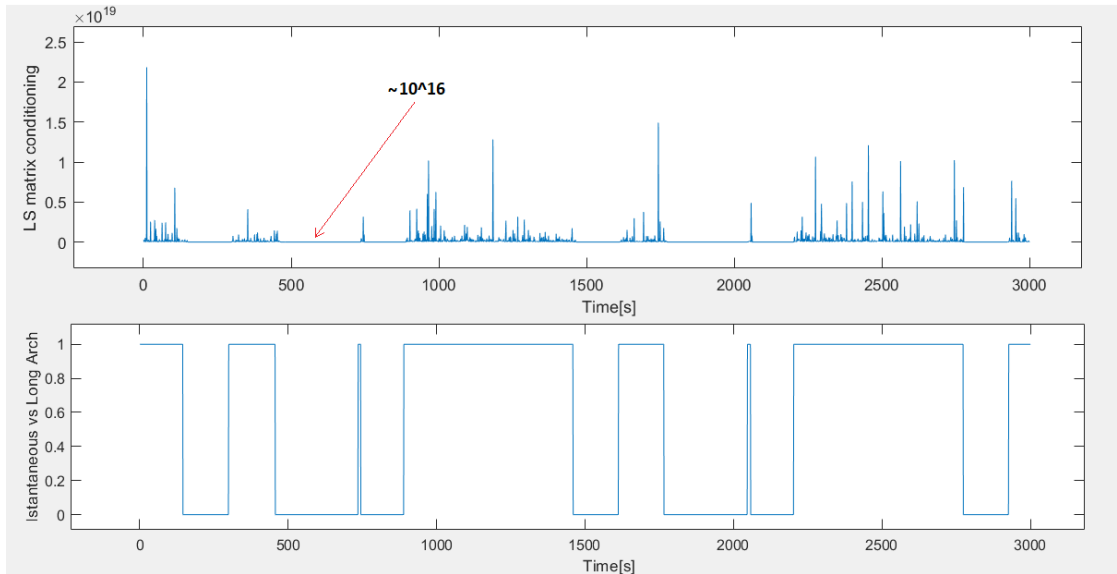


**Figure 4.6:** Least squares  $\Lambda$  matrix conditioning (top) and observables availability (bottom) for two beacons and ISL: 1 corresponds to all 24 observables available while 0 indicates that at least one observable is not available.

These preliminary results pointed out the necessity of having more observables, either with the addition of a ranging beacon or with altimetric measurements. Initially, the former approach was considered, leading to the second important

insight into these beacons and ISL architectures: the influence of measurement noise on the instantaneous algorithm.

As soon as a third beacon was added, the observability problem was solved: the least squares matrix conditioning lowered to  $10^9$ ,  $H$  matrix was full rank and  $\Lambda$  became positive definite. The number of maximum measurements available in this scenario is 32, that are the same 24 from previous case plus 8 more corresponding to range and range rate from the third beacon to each of the four satellites (4x2). In the absence of measurements noise, the results of the OD algorithm for the keplerian unperturbed case were promising as shown in Figure 4.7 below, with sub-millimeter accuracy in position for the instantaneous OD and few-meters level when using the batched least squares.

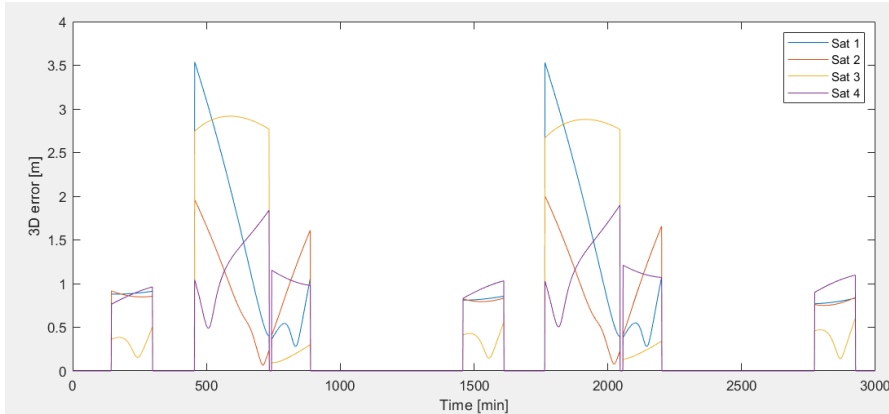


**Figure 4.7:** 3D position error for 3 beacons and ISL scenario in the absence of measurement noise for 2 days of simulation

Clearly, this simulation was only conducted to test the validity of the algorithm, to verify the correctness of the formulation of the problem in terms of observability and the conditioning number of the LS matrix to be expected.

The addition of measurement noise on beacon ranging was found to be critical. While range and range-rate data from ISL and range-rate from beacons did not have a big impact on the OD solution, except for showing some oscillations in the 3D error in position when calculating the solution instantaneously, as Figure 4.8 illustrates, a massive 3D error during these same instantaneous OD arches was found when measurement noise was added to the range data from the beacons. This latter is shown in Figure 4.9 where the green line indicates the instantaneous OD arches, corresponding to the epochs when all the 32 observables were available.

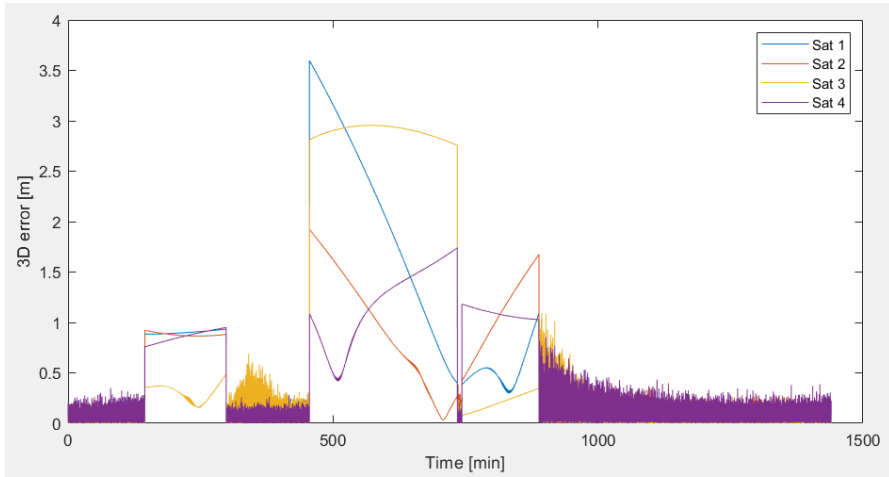


**Figure 4.8:** 3D position error for 3 beacons and ISL scenario with measurement noise on range and range-rate from ISL and range-rate from beacons for 24 h of simulation

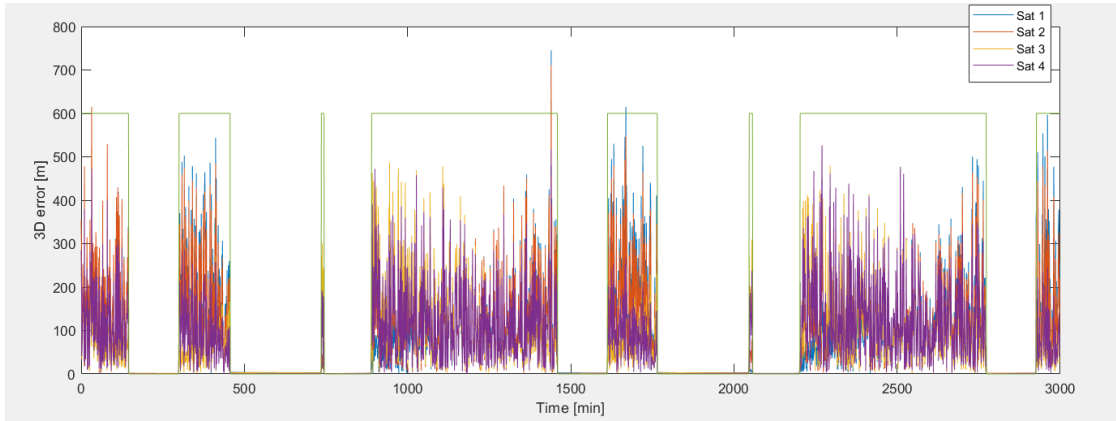


**Figure 4.9:** 3D position error for 3 beacons and ISL scenario with measurement noise on all observables for 2 days of simulation

Both Figure 4.9 and 4.8 indicate that the oscillations are due to the noise on the range data from the beacons. This can both be interpreted numerically and geometrically. From a mathematical point of view, it all comes down to the conditioning number of  $\Lambda$ . In spite of the fact that  $10^9$  is much lower than the observability threshold  $10^{16}$ , it still indicates an ill conditioned least squares problem. In fact, being the dynamical model known for the Keplerian case, perfect measurements without noise, being the problem correctly formulated and the state vector observable, as expected lead to extremely accurate results when all satellites are in view of the beacons as in Figure 4.7, and the only deviations

from true trajectories are entirely due to computational instabilities. When measurement noise is added though, the right-hand side of (2.3.15) is modified with  $10^{-2}$  meters of perturbation. In fact, the levels of noise preliminary introduced were  $\sigma_{range-ISL} = 5cm$ ,  $\sigma_{range-rate-ISL} = 0.03mm/s$ ,  $\sigma_{range-beacons} = 5cm$  and  $\sigma_{range-rate-beacons} = 0.03mm/s$ . Though being an optimistic amplitude of noise, a  $10^{-2}$  perturbation is amplified through a  $10^9$  conditioning and increases to the hundreds meters of error displaced in Figure 4.9. This is a well-known behavior of ill conditioned linear systems in the form of (2.3.16) as in [86].

From a geometrical perspective, as [87] points out for the GNSS case, when a poor geometry is encountered, in order to improve the precision and the reliability of OD the solution it is necessary to track the satellites for a certain period, allowing the trajectories to change enough for the receiving stations to collect diversified data. In the present scenario, when all the four satellites are passing over the South Pole and are in view of the beacons, the geometry is quite poor: this is both because the satellites are at their closest point and because the beacons are located near each other due to mission drivers and logistic. Indeed, since the initial phases of the Artemis program and of ESA's Moonlight initiative will focus on the lunar South Pole, it is highly unlikely that due to costs and complexity, at least at the beginning, surface beacons could be placed far from this region. The proximity of the beacons to each other and the low angular velocity of the satellites passing over the South Pole at their aposelene tend to produce very similar observation equations [88] that have to be diversified with sufficiently long periods of measurements collecting.

All these considerations are supported by additional simulations that have been conducted virtually placing the third beacon far from the Moon's South Pole. As expected, the further the location was chosen, the better the OD results. This is shown in Figure 4.10 below where the 3D error in position is reported for three scenarios where the beacon was progressively moved further from the others. A constellation average 3D error of 25m was found at best for the instantaneous OD algorithm.

Since the mixed algorithm proved to be unsuitable for this scenario, some simulations were conducted with the long arch one to assess the influence of the aforementioned factors (i.e., poor geometry, conditioning, noise) when using batches of data collected at different epochs. The results of Figure 4.11 indicate that although eliminating the oscillations of the mixed algorithm, during the transit above the South Pole of all satellites (indicated with the green horizontal line at constant value equal to 1), the low angular velocity and the measurement noise still have a big impact on the quality of the OD solution.

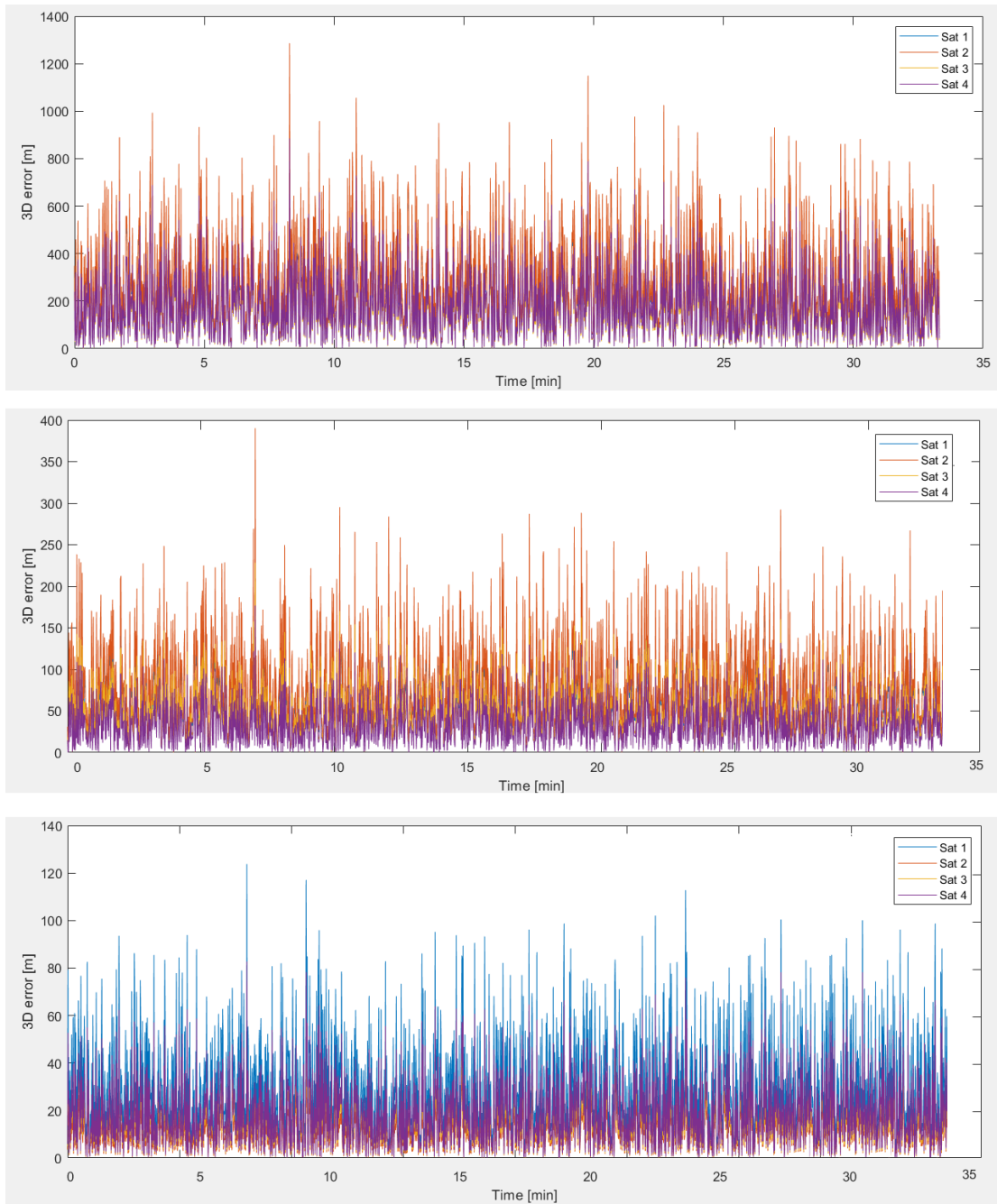


**Figure 4.10:** 3D position error for 3 different locations of the third beacon progressively moved further from the South Pole (from the top image to the bottom)

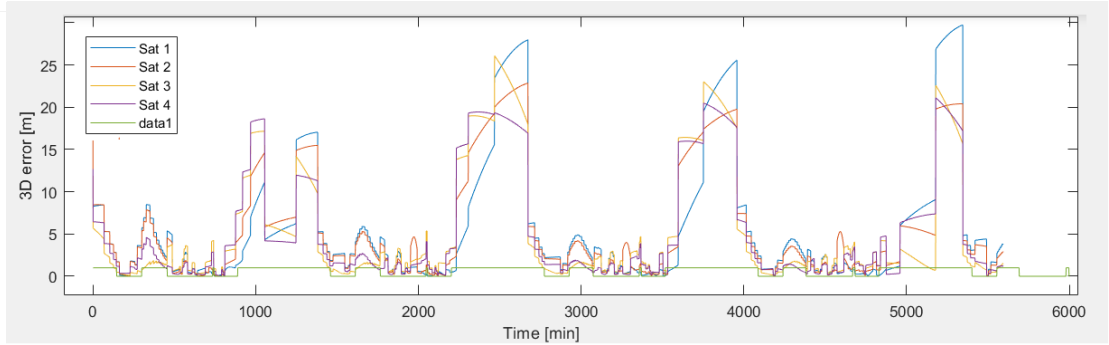


**Figure 4.11:** 3D position error for 3 beacons and ISL scenario with long arch OD algorithm for 4 days of simulation

The conclusion of this preliminary analysis is thus twofold: firstly, adding a third beacon makes the state vector fully observable, but the mixed algorithm solution, which would be efficient for near real-time orbit update, suffers from measurement noise due to the ill conditioned  $\Lambda$  matrix; on the other hand, the batched long arch algorithm is still greatly influenced by poor geometry as Figure 4.11 demonstrates. Since, as mentioned before, it is unlikely to expect the beacons to be placed further, this results led to the necessity of adding a diversified observable, rather than an additional beacon, that is the altimeter, as for section 4.2.

Before proceeding to the next scenario, it is also worth to point out that some trials were made regarding the solution methods of the linear least squares system of (2.3.16) exploiting the positive definiteness of the information matrix  $\Lambda$ . Particularly, the preconditioned conjugate gradient method was implemented with the incomplete Cholesky decomposition for the preconditioner, following the procedure of [89]. Since it did not yield more accurate results, a proposed approach for further studies is to use the Tikhonov-Phillips regularization illustrated in [88].

### 4.3.2 Two Beacons, ISL and Altimeter

The addition of altimetric measurements led to very positive results. Either with two or three beacons, these are the first scenarios that were also tested with real perturbed simulated ELFOs. Different time spans were considered, as well as different data rates for the Keplerian case.

Figure 4.12 reports the 3D error in position and velocity for the Keplerian scenario with 2 beacons, ISL contacts and the altimeter for a data rate of 1 batch of observables gathered per minute from each ranging source for 24h of simulation.

Even with time spans as short as 30 minutes, a constellation mean 3D error of 3m is reached. With 60 minutes the error is halved and slightly decreases as the duration of the arch gets longer. The level of noise introduced here is the same as in previous sections for both beacons and altimeter.

While increasing the data rate for the DSN-only and DSN and altimeter scenarios did not lead to more accurate results, in the present case it does have a significant impact, with a higher data rate improving the performances of the OD algorithm considerably. This is justifiable considering that from the DSN antenna perspective, appreciable geometric changes in the satellite trajectories occur after much longer time periods than from the surface beacons point of view, because of the around 30 times greater distance that the former ranging source have from the lunar orbiters compared to the latter. This means that batches of observables collected at consecutive seconds will not provide useful informations and significantly lower data rates can be used.

In the Table 4.3 below a comparison of the performances for the two data rates in terms of 3D mean and maximum error is reported, showing the improvement in performances aforementioned. The trend of the 3D errors in position and velocity for the higher data rate is reported in Figure 4.13 for completeness.

3D error		Position [m]		Velocity [mm/s]	
Data Rate	Time Span	Mean	Max	Mean	Max
1 batch/minute	30 min	3.16	10.64	0.27	2.12
	60 min	2.13	7.47	0.18	1.50
	90 min	1.88	6.00	0.15	1.29
1 batch/second	30 min	0.43	6.53	0.12	5.81
	60 min	0.38	1.06	0.09	0.33
	90 min	0.28	0.89	0.08	0.44

**Table 4.3:** 3D position and velocity errors comparison for different data rates for the scenario with 2 beacons, ISL and altimeter

Even if the performance improvement is tangible, a data rate as low as one batch of observables per minute still yields good results, which is to be considered in the trade-off analysis as an important feature since lower rates would significantly reduce processing effort and memory requirements.

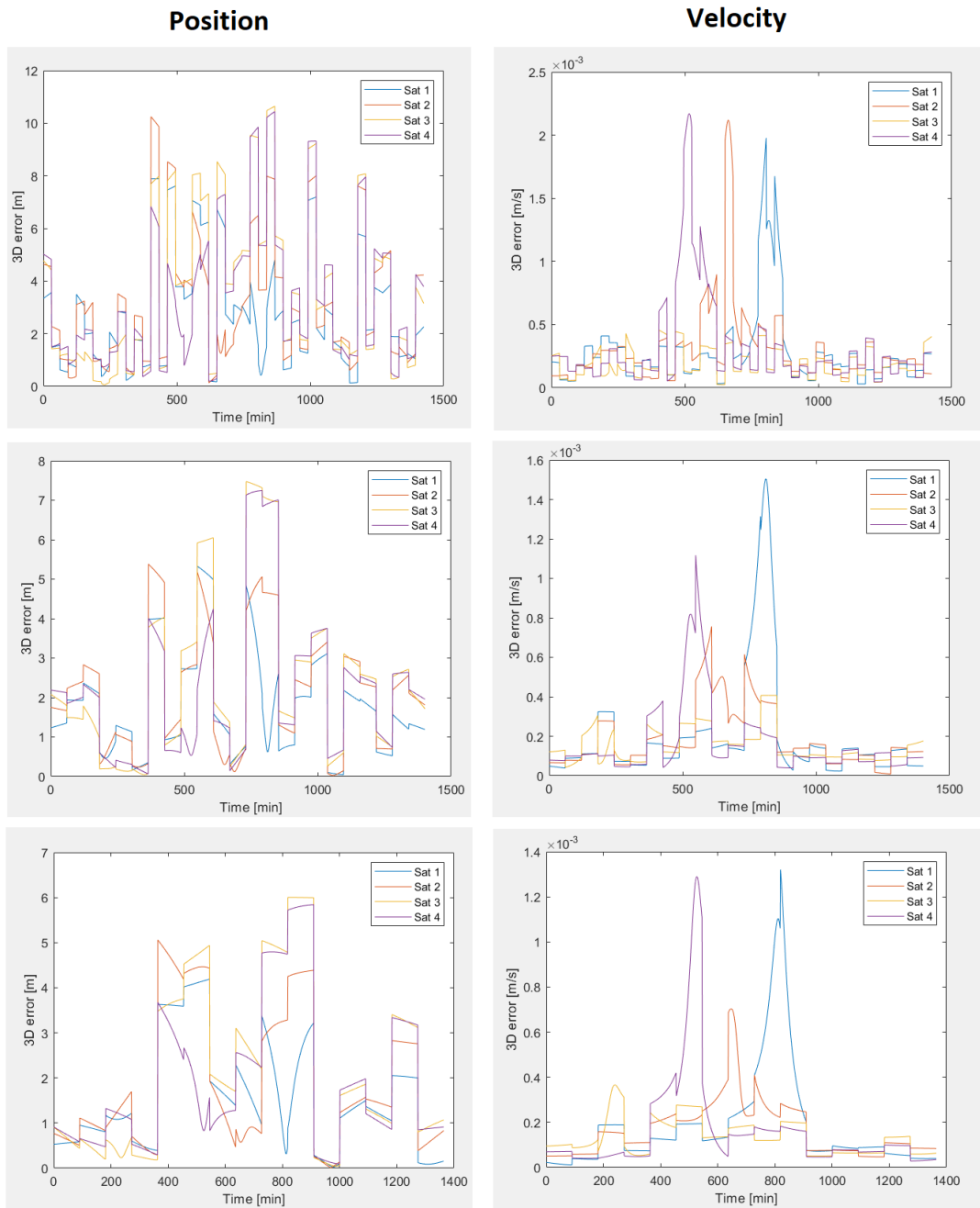


**Figure 4.12:** 3D position and velocity errors for Keplerian scenario with 2 beacons, ISL and altimeter, 24 hours of simulation, 1 batch of observables per minute and increasing time span from top to the bottom (30,60 and 90 minutes)

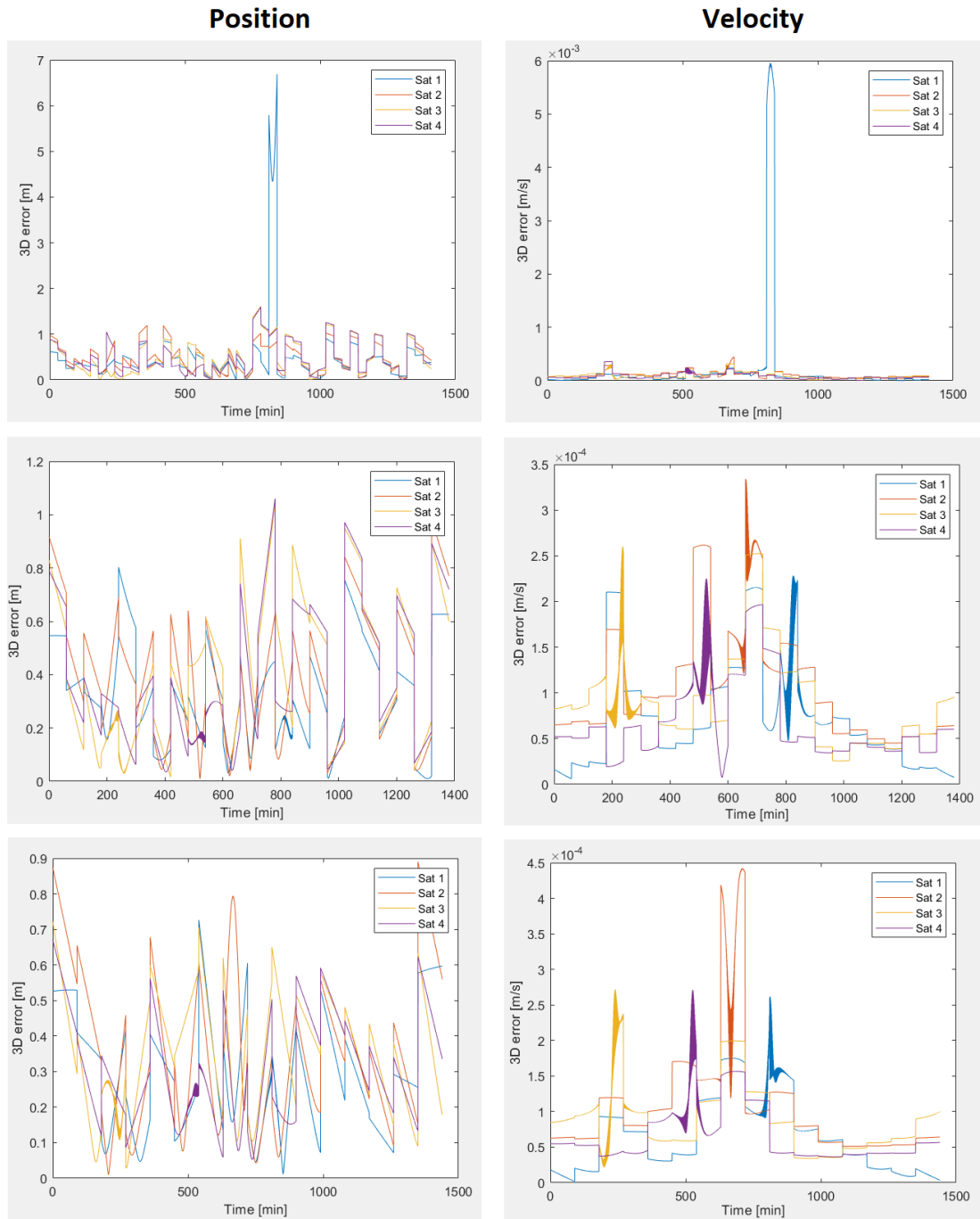


**Figure 4.13:** 3D position and velocity error for the Keplerian scenario with 2 beacons, ISL and altimeter with long arch OD algorithm for 24 hours of simulation, 1 batch of observables per second, increasing time span from top to the bottom (30, 60 and 90 minutes)

For completeness, Figure 4.14 reports the variation in the number of observables collected at each epoch overtime. The maximum is 28, being 24 from the previous scenario with two beacons plus 4 altimetric measurements. The minimum number is 20, corresponding to a satellite losing LOS communication with the others (2 ISL contacts, from which 4 measurements) and with the beacons (4 among range and range-rates measurements) when passing over the North Pole at its periselene.

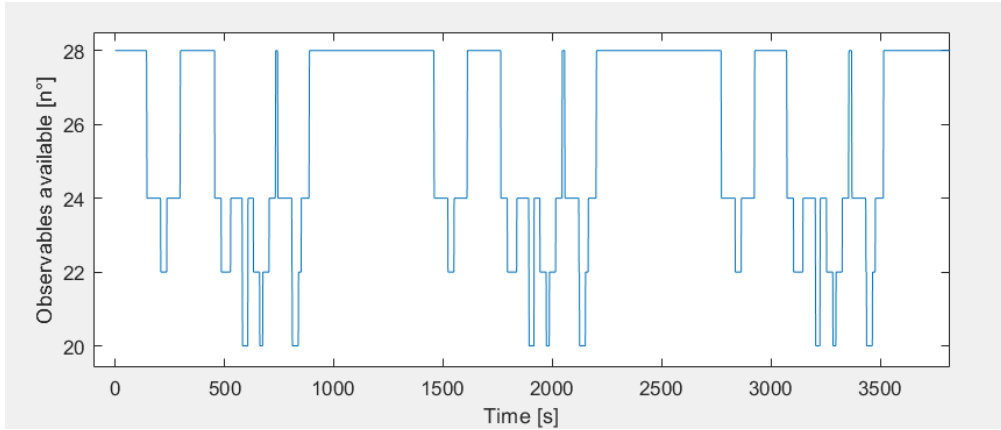


**Figure 4.14:** Number of observables collected per epoch (Keplerian model)

A further confirm of the mitigation of noise and observability for this architecture where the dynamic model is known comes from the real perturbed scenario when the ELFOs were simulated as described in 3.3.2. Figure 4.15 illustrates the 3D error in position and velocity obtained using Moon HPOP in the long arch algorithm. With prediction arches as short as the one considered for this case, no divergence in the algorithm occur even when using the perturbed model, which generally causes the trajectories to drift strongly depending on their initial Keplerian parameters, leading estimated and real orbits to diverge quickly. This last simulation was conducted with a data rate of 1 batch of observables per minute.

Table 4.4 below resumes the 3D errors for this latter case.

3D error		Position [m]		Velocity [mm/s]	
Data Rate	Time Span	Mean	Max	Mean	Max
1 batch/minute	30 min	3.89	11.4	0.39	2.71
	60 min	3.01	8.63	0.34	1.91
	90 min	1.88	7.59	0.29	1.52

**Table 4.4:** 3D position and velocity errors comparison for different time spans for the scenario with 2 beacons, ISL and altimeter with perturbed ELFOs (HPOP)

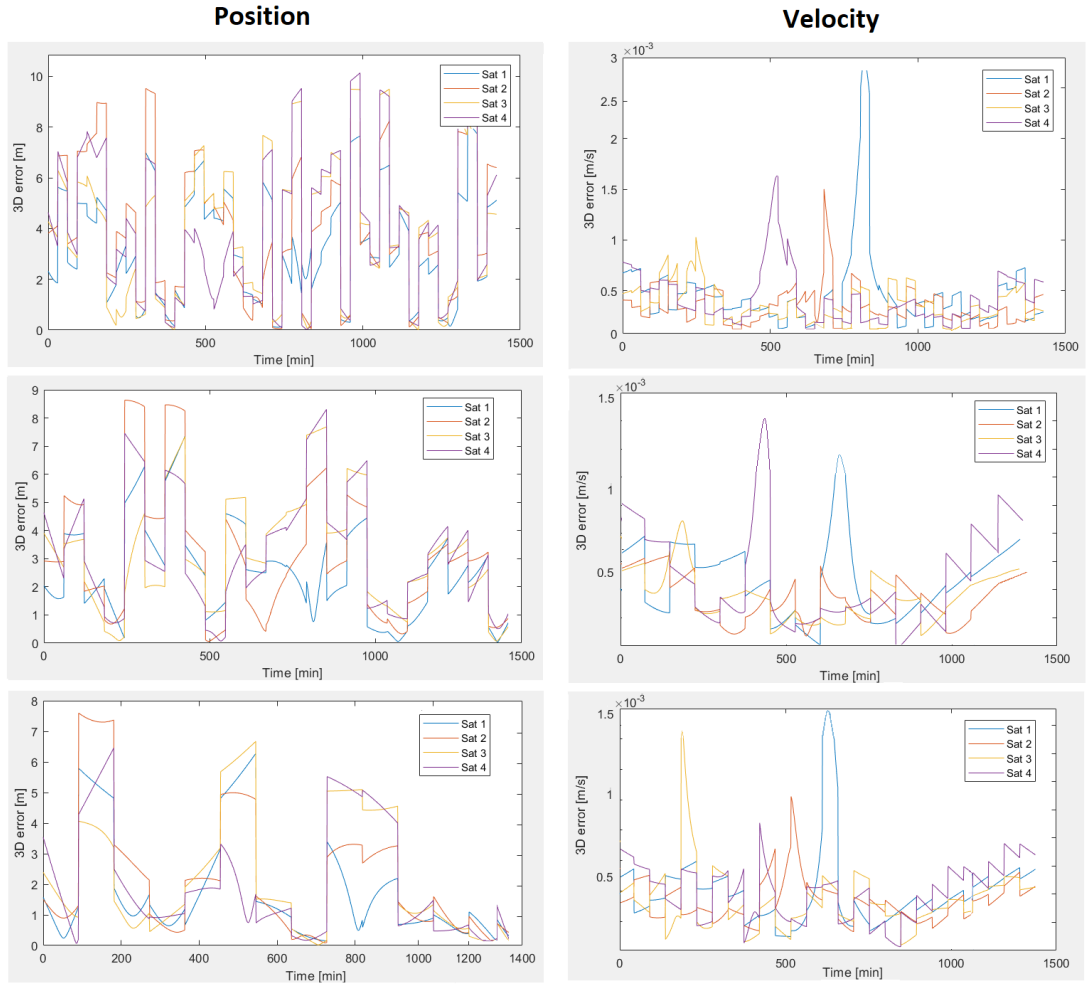


**Figure 4.15:** 3D position and velocity error for the scenario with 2 beacons, ISL and altimeter with long arch OD algorithm for 24 hours of simulation, 1 batch of observables per minute and perturbed ELFOs (dynamical model known), increasing time span from top to the bottom (30, 60 and 90 minutes)

In the previous simulations, the exact dynamical model was assumed to be known both with the Keplerian case and with the perturbed ELFOs. In fact, for this latter case, the complete model with 48x48 gravitational field potential spherical harmonics, SRP and third body perturbations, was used to propagate the the state vector and the state transition matrix inside the logic of the OD algorithm. This gave room to a deep analysis into the impact of measurement noise, initial guesses, observability, data rates and time spans. An additional step was using a simplified dynamical model in the algorithm to deal with the real perturbed ELFOs: as

anticipated in section 3.3, only third bodies perturbations and SRP were taken into account hypothesizing that those were accurately well modellable, while spherical harmonics were ignored, considering only Moon's point mass acceleration. This is a reasonable assumption, and it is still conservative considering that complete and highly precise models for lunar gravity field are known, as the one in HPOP, though it has to be underlined that the ELFOs considered were simulated through HPOP and do not come from real ephemerides. Figure 4.17 reports the 3D error in position for this scenario with time spans of 30,60 and 120 minutes. The graphs on the left represent the whole error trend overtime, while the ones on the right are details from the simulation periods when all satellites were in view of the beacons. The same logic is followed for the 3D error in velocity illustrated in Figure 4.18

In Figure 4.16 below the number of observables available as in 4.14 is reported for comparison with the 3D position error for the 30 minutes case. What is clear from this result is that as long as many observables are available, in spite of the fact that the algorithm is using an approximated and conservative dynamical model, the results are quite good. This leads to possible improvements as the algorithm could be modified to handle the outages of the satellites overflying the North Pole as further explained in chapter 6.

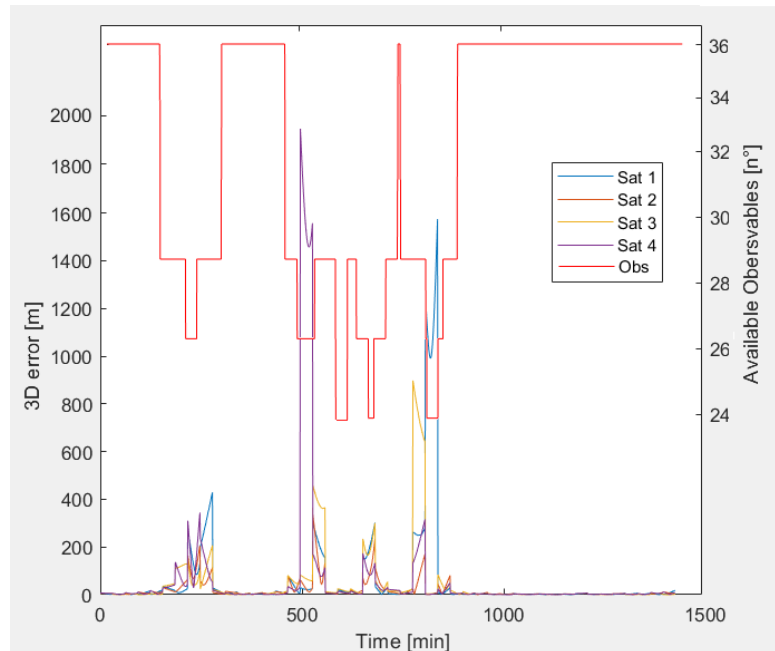


**Figure 4.16:** 3D error for 2 beacons, ISL and altimeter compared to observables availability for real perturbed case and long arch algo with 30 minutes of time span

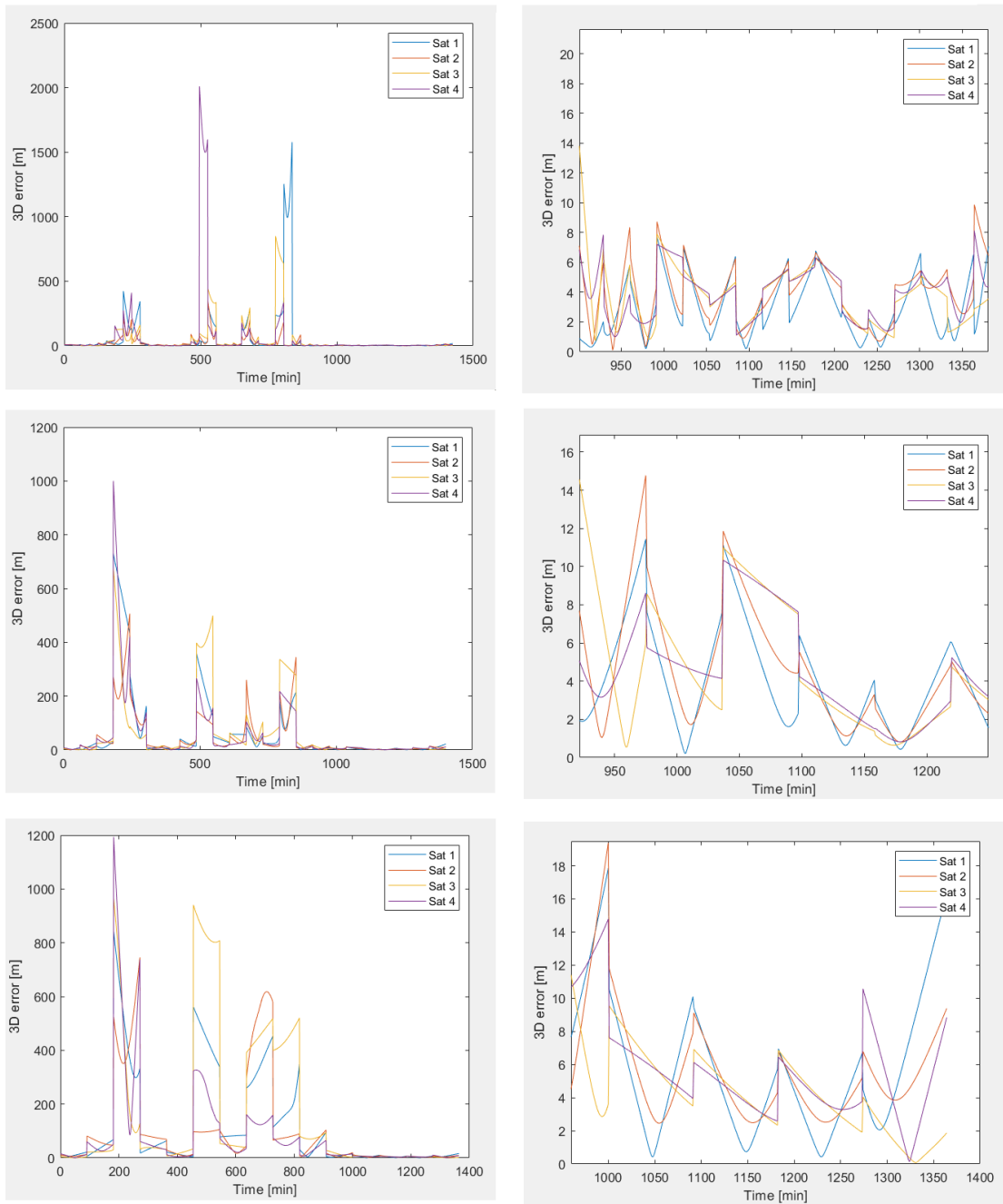


**Figure 4.17:** 3D position error (left) and detail(right) for real perturbed scenario (limited knowledge of dynamical model) with 2 beacons, ISL and altimeter, 1 batch of observables per minute and increasing time span from top to the bottom (30, 60 and 90 minutes)

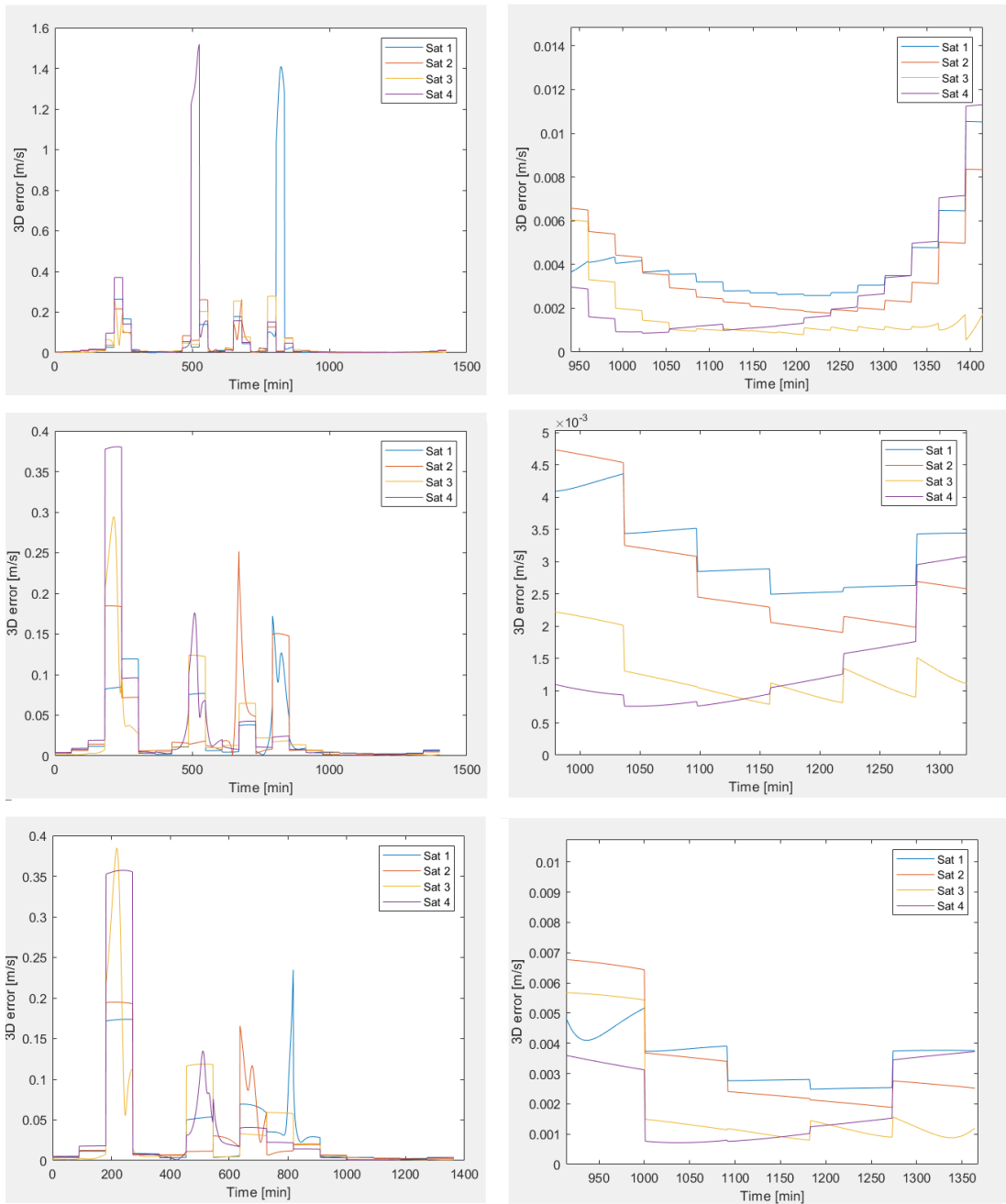


**Figure 4.18:** 3D velocity error (left) and detail(right) for real perturbed scenario (limited knowledge of dynamical model) with 2 beacons, ISL and altimeter, 1 batch of observables per minute and increasing time span from top to the bottom (30, 60 and 90 minutes)

### 4.3.3 Three Beacons, ISL and Altimeter

As it will be clear from the results of these simulations, when the altimeter is added, the effect of noise on the OD is already sufficiently mitigated with 2 beacons and though providing a slight improvement in the 3D error, the addition of a third beacon is not justified considering the increase in the complexity of the system architecture. This will be further analyzed in the next chapter. As for the previous section, Figure 4.19 below illustrates the variation in the number of observables collected per epoch overtime in the Keplerian case for completeness. This time, 36 observables are available at maximum (24 (6x4) from the beacons, 8 (2x4) from ISL and 4 from the altimeters) while at minimum 26 sources are always available, again corresponding to a satellite passing over the lunar North Pole and losing LOS communication with the 3 beacons ( from which 6 measurements ) and with the other satellites ( 4 ISL measurements ).

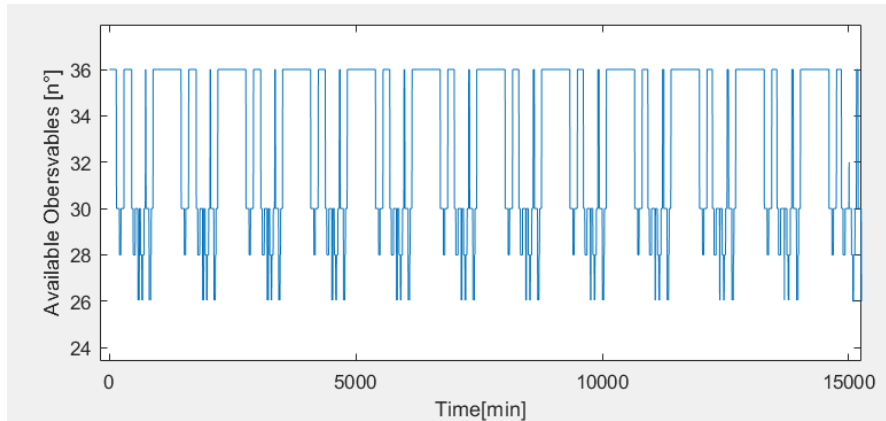


**Figure 4.19:** Number of observables collected per epoch (Keplerian model)

The next pages will illustrate with the same logic of the previous section the 3D error in position and velocity. Firstly, Figure 4.20 will report the results for the Keplerian ELFOs with a data rate of 1 batch per minute. After that, Figure 4.21 will compare the precedent results introducing a higher data rate of 1 batch per second and following that, Figure 4.22 will illustrate the error for the perturbed scenario when using Moon HPOP for the dynamical model in the OD algorithm.

Table 4.5 below resumes and compares quantitatively the 3D errors for the three aforementioned scenarios where the dynamical model is known and the effects of noise and initial guess only are studied. The results confirm the conclusions of the previous section: the addition of the altimeter manages to handle the measurement noise pretty well and the initial guess error as well even with the perturbed model

that could cause divergence. The good performances in this latter case are mainly thanks to the limited time spans considered. The clear improvements in the OD solution and following orbit prediction for the higher data rate are also confirmed.

3D error			Position [m]		Velocity [mm/s]	
Model	Data Rate	Time Span	Mean	Max	Mean	Max
Keplerian	1 batch/minute	30 min	2.82	12.4	0.3	2.41
		60 min	1.72	5.1	0.15	0.72
		90 min	1.32	4.65	0.21	1.05
	1 batch/second	30 min	0.38	6.44	0.15	5.83
		60 min	0.25	1.12	0.12	0.39
		90 min	0.22	0.94	0.09	0.46
Perturbed	1 batch/minute	30 min	2.82	11.7	0.33	1.31
		60 min	1.81	7.30	0.31	1.19
		90 min	2.38	6.43	0.27	0.91

**Table 4.5:** 3D position and velocity errors comparison for different time spans and dynamical models for the scenario with 3 beacons, ISL and altimeter

Following that, the analysis of the 3D error for the scenario where limited knowledge of the dynamical model is available (no spherical harmonics coefficients in the gravity field description) is reported in Figure 4.23 and 4.24, showing consistent results with the corresponding case of the previous section: very good performances are obtained when all satellites are in view of the beacons and many observables are available, regardless of the conservative model used for orbit prediction. Again, this is mainly thanks to the limited time spans used that prevented the predicted orbits to diverge consistently from the real ones. Indeed, for both the present and the previous scenario with two beacons, 60 minutes looks to be an optimal duration of the time span both for collecting observables and for the orbit prediction phase when the initial state vector calculated with the batches of observables collected during the time span, is propagated. Longer time spans both exhibit higher peaks of errors when the constellation undergoes poor observability and higher mean 3D errors when many observables are available as well. Conversely, shorter time spans lead to improved performances in the mean error with good observability but exhibit higher peaks error of around 2 to 2.5 kilometers.

For the 60 minutes time span, although the peak error is still as high as 1 kilometers, the mean error when the satellites are all in view of the beacons is around 3.5 meters (Figure 4.23), which is good both being a 3D error (so not the SISE as seen by the final PNT service user) and still a conservative estimate.

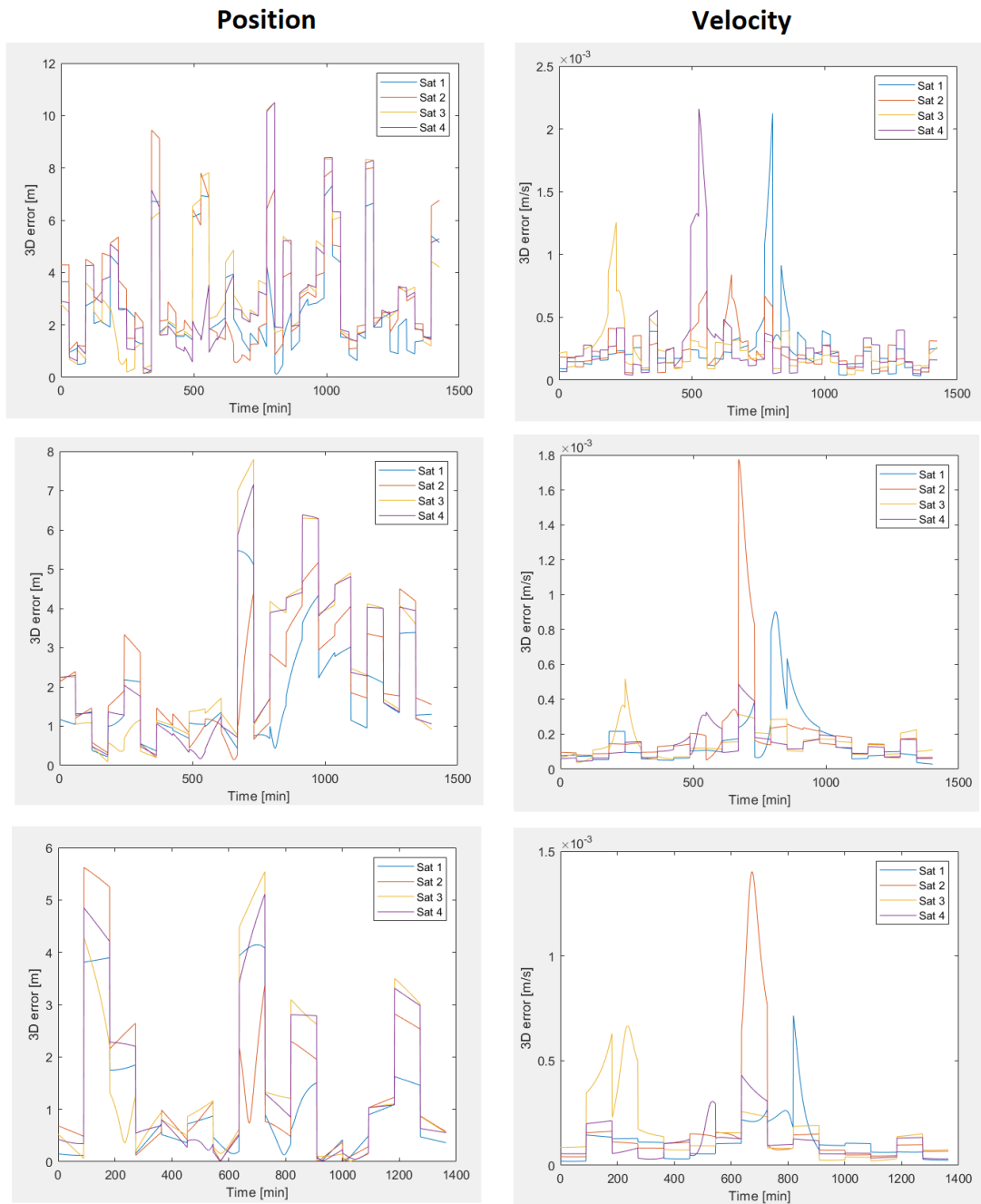


**Figure 4.20:** 3D position and velocity errors for the Keplerian scenario with 3 beacons, ISL and altimeter with long arch OD algorithm for 24 hours of simulation, 1 batch of observables per minute and increasing time span from top to the bottom (30, 60 and 90 minutes)

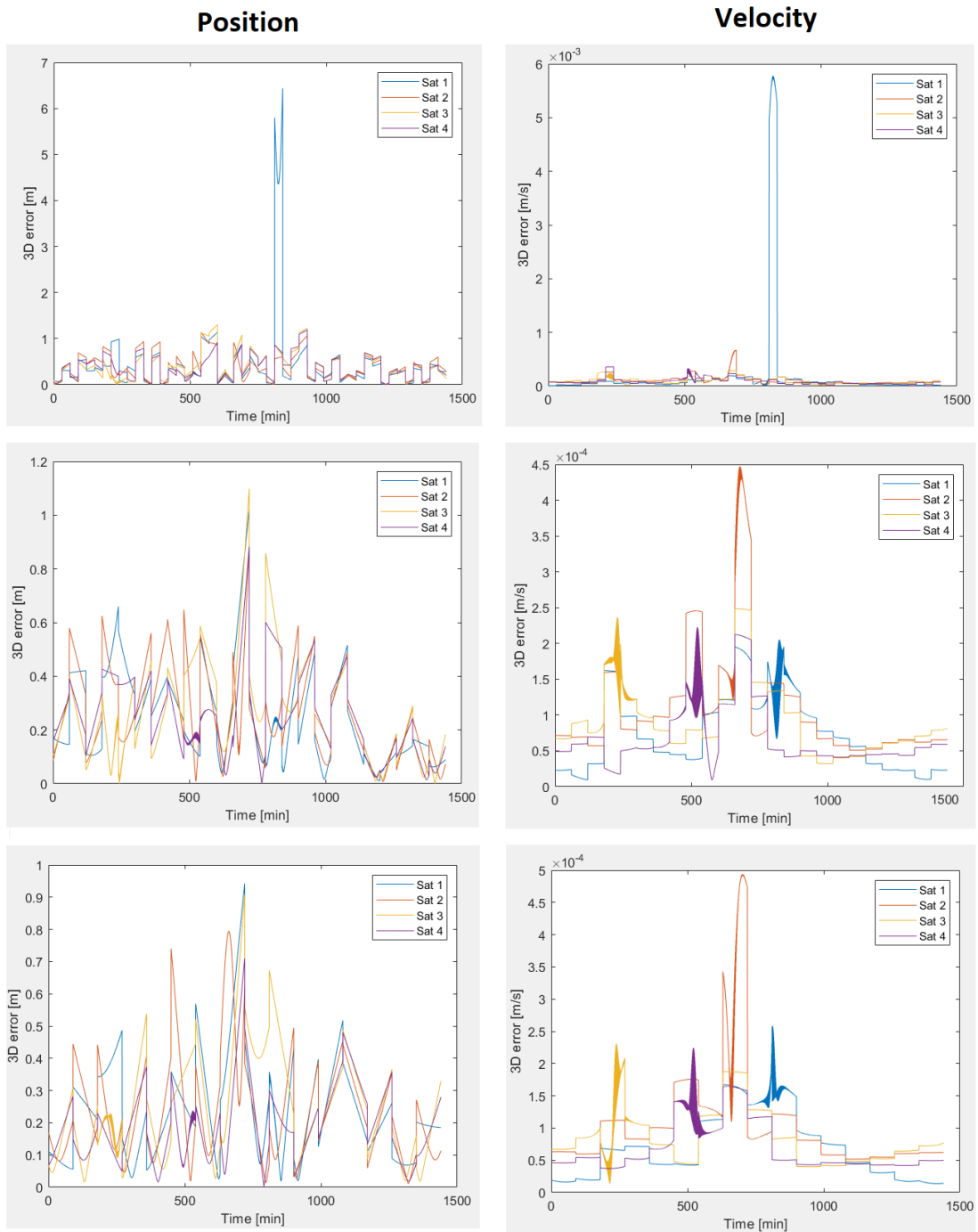


**Figure 4.21:** 3D position and velocity errors for the Keplerian scenario with 3 beacons, ISL and altimeter with long arch OD algorithm for 24 hours of simulation, 1 batch of observables per second and increasing time span from top to the bottom (30, 60 and 90 minutes)

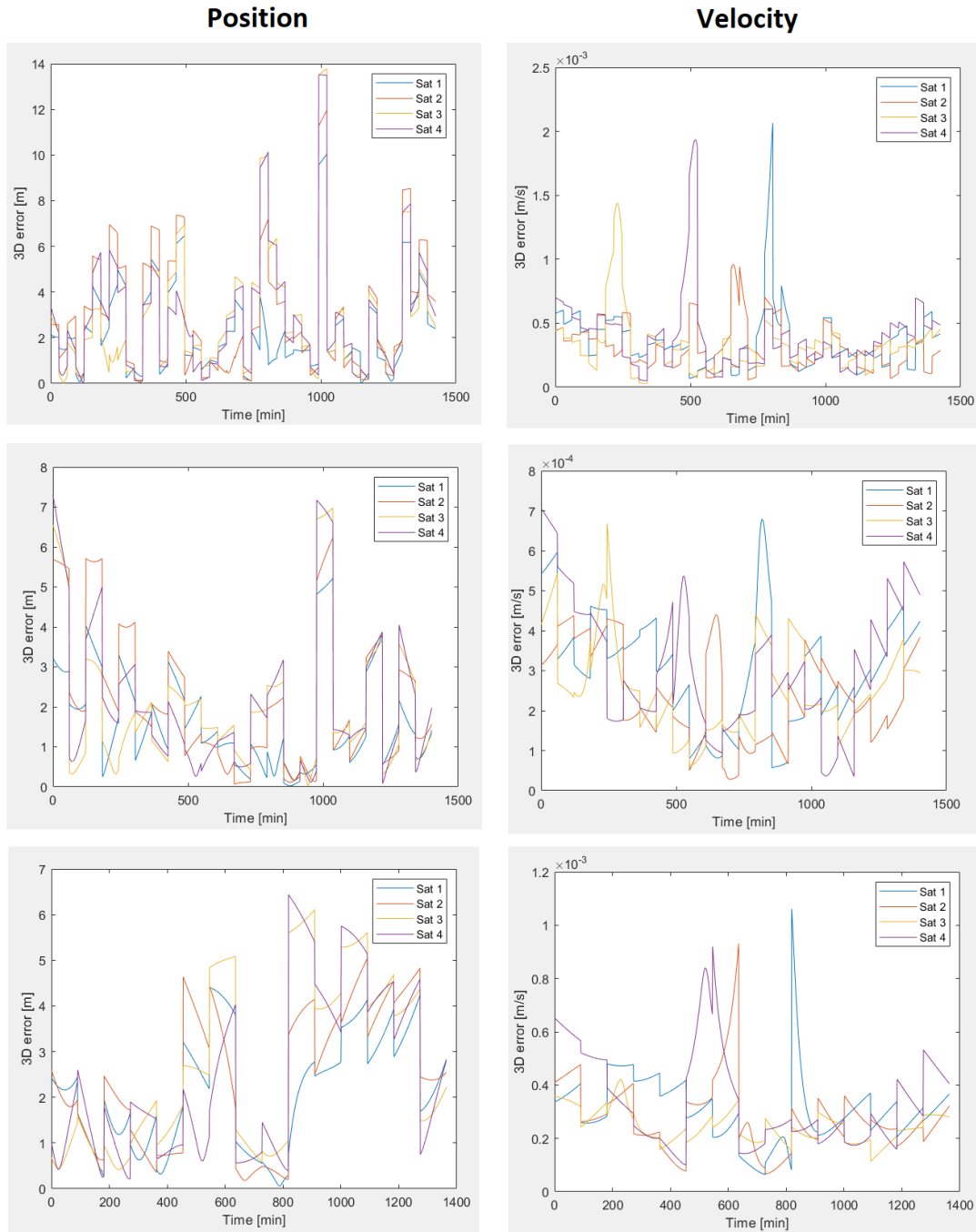


**Figure 4.22:** 3D position and velocity errors for the perturbed scenario (dynamical model known) with 3 beacons, ISL and altimeter with long arch OD algorithm for 24 hours of simulation, 1 batch of observables per minute and increasing time span from top to the bottom (30, 60 and 90 minutes)

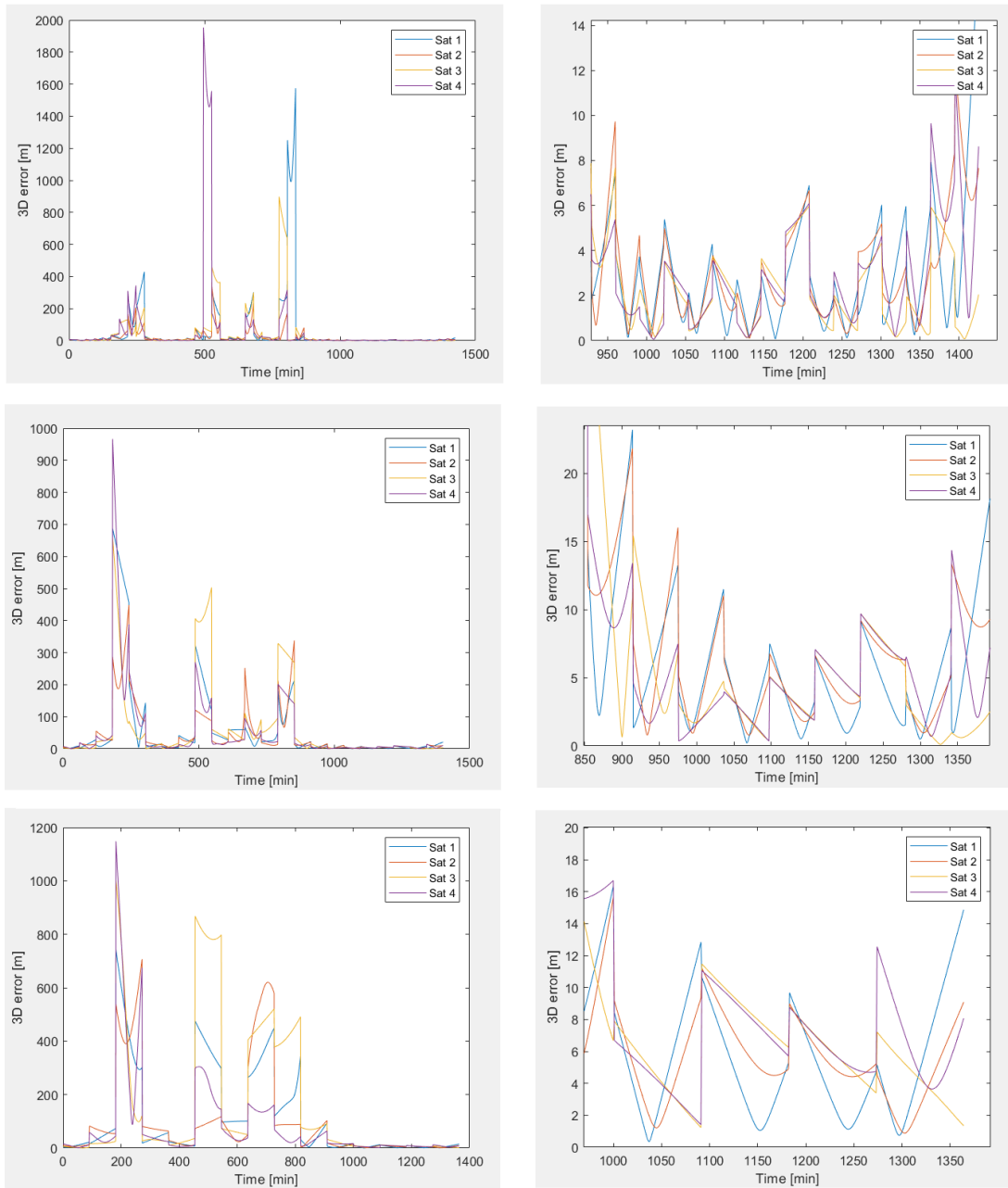


**Figure 4.23:** 3D position error (left) and detail(right) for real perturbed scenario (limited knowledge of dynamical model) with 3 beacons, ISL and altimeter, long arch OD algorithm, 1 batch of observables per minute and increasing time span from top to the bottom (30, 60 and 90 minutes), 24h of simulation

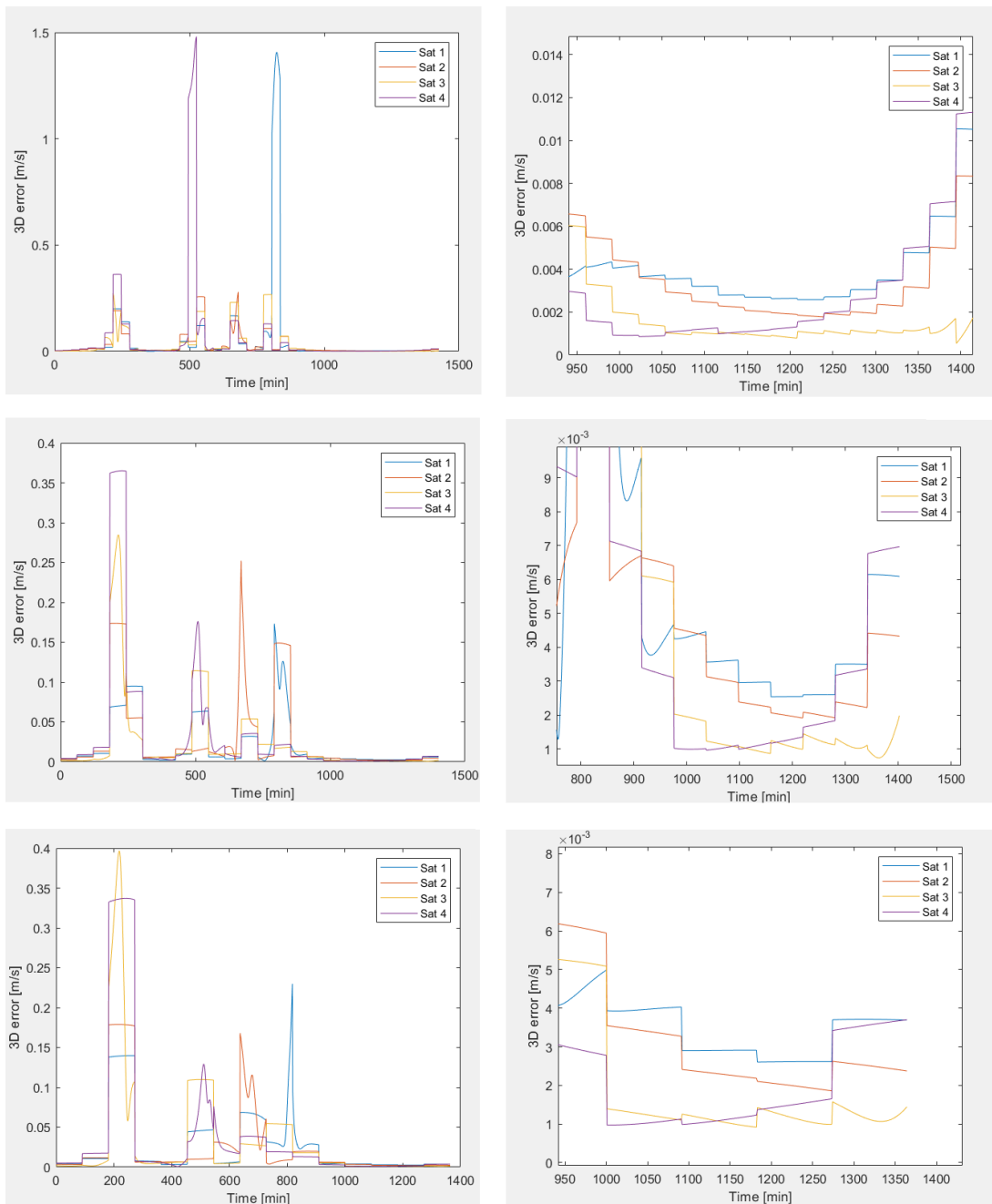


**Figure 4.24:** 3D velocity error (left) and detail(right) for real perturbed scenario (limited knowledge of dynamical model) with 3 beacons, ISL and altimeter, long arch OD algorithm, 1 batch of observables per minute and increasing time span from top to the bottom (30, 60 and 90 minutes), 24h of simulation

## 4.4 Lunar beacons, DSN, ISL and Altimeter

This scenario is the one with the highest number of observables available. Three beacons provide 24 measurements and 24 as well are from the three DSN antennas, while the on-board altimeters and the 4 ISL contacts provide 12 observables. In total, 60 measurements are theoretically available at most. In practise, as for section 4.1, it is clearly impossible to have all three DSN stations in view, which means that the maximum number of observables simultaneously available is 52 (60-8 from one DSN station). The least number corresponds to two satellites temporarily lacking LOS with the beacons during a period when DSN is not tracking the constellation, and it is 24 as shown in Figure 4.25 below, where the availability of measurements is reported overtime. Clearly, one of the two satellites is going towards the lunar North Pole, while the other has just overflown it and it is directed at its aposelene. Since these two satellites do not generally use the ISL to communicate with each other, all cross-linking data are still available. Note that the pattern in Figure 4.25 is not periodic as it is derived from the perturbed ELFOs. The standard deviations of measurement noise for beacons and ISL are the same as for previous scenarios:  $\sigma_{range-ISL} = 5cm, \sigma_{range-rate-ISL} = 0.03mm/s, \sigma_{range-beacons} = 5cm, \sigma_{range-rate-beacons} = 0.03mm/s$ ; instead, being a very high number of observables available, it was decided to increase the noise on DSN and altimeter data to  $\sigma_{range-DSN} = 1m, \sigma_{range-rate-DSN} = 0.1mm/s$  and  $\sigma_{range-altimeter} = 0.2m$  to assess the capability of the algorithm to handle these noises.

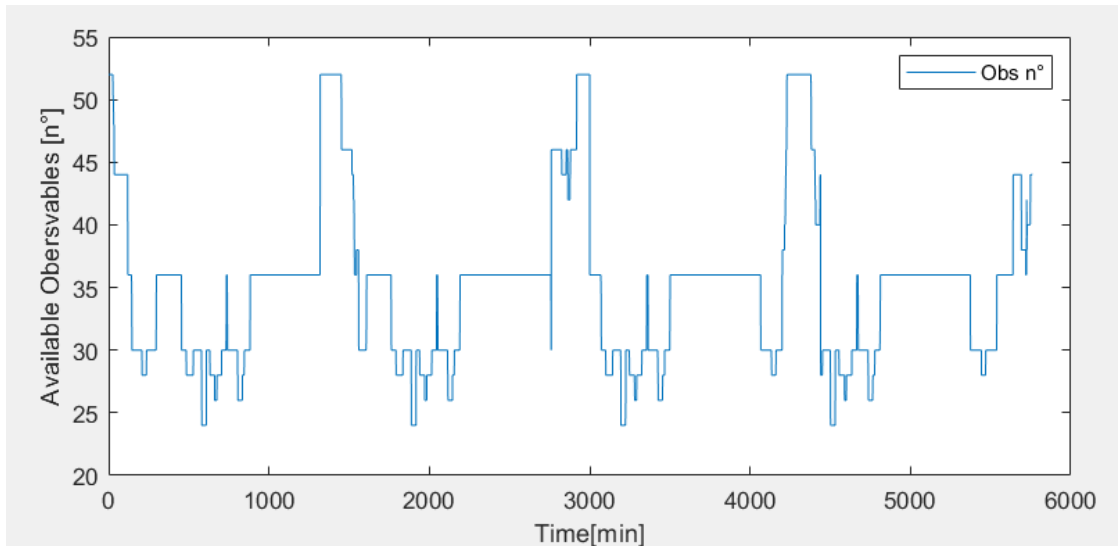


**Figure 4.25:** Number of observables available overtime for the scenario with three beacons, ISL, DSN and altimeter (perturbed scenario)

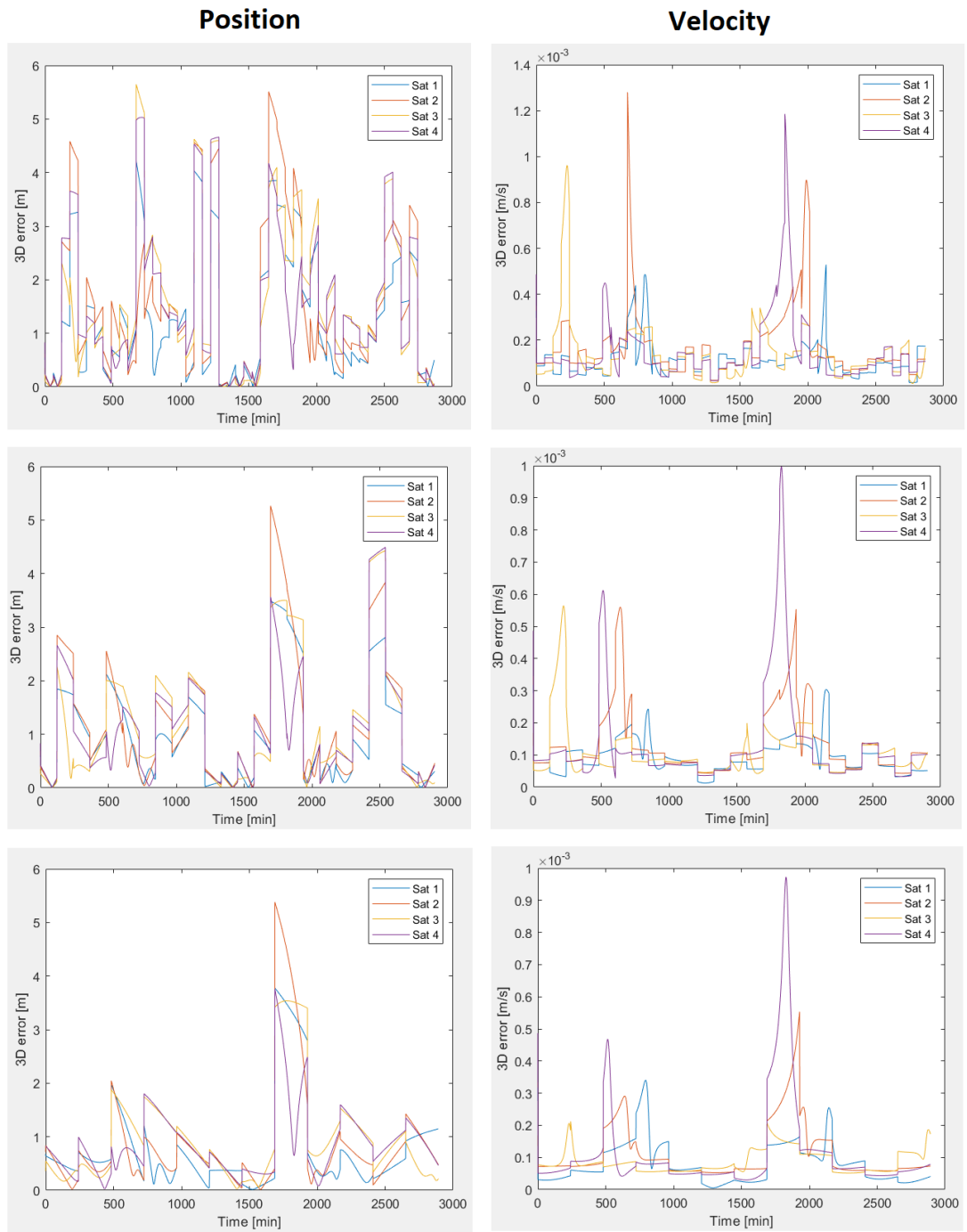


**Figure 4.26:** 3D position and velocity error for Keplerian scenario with 3 beacons, ISL, DSN and altimeter, long arch OD algorithm, 1 batch of observables per minute and increasing time span from top to the bottom (1, 2 and 4 hours), 48h of simulation

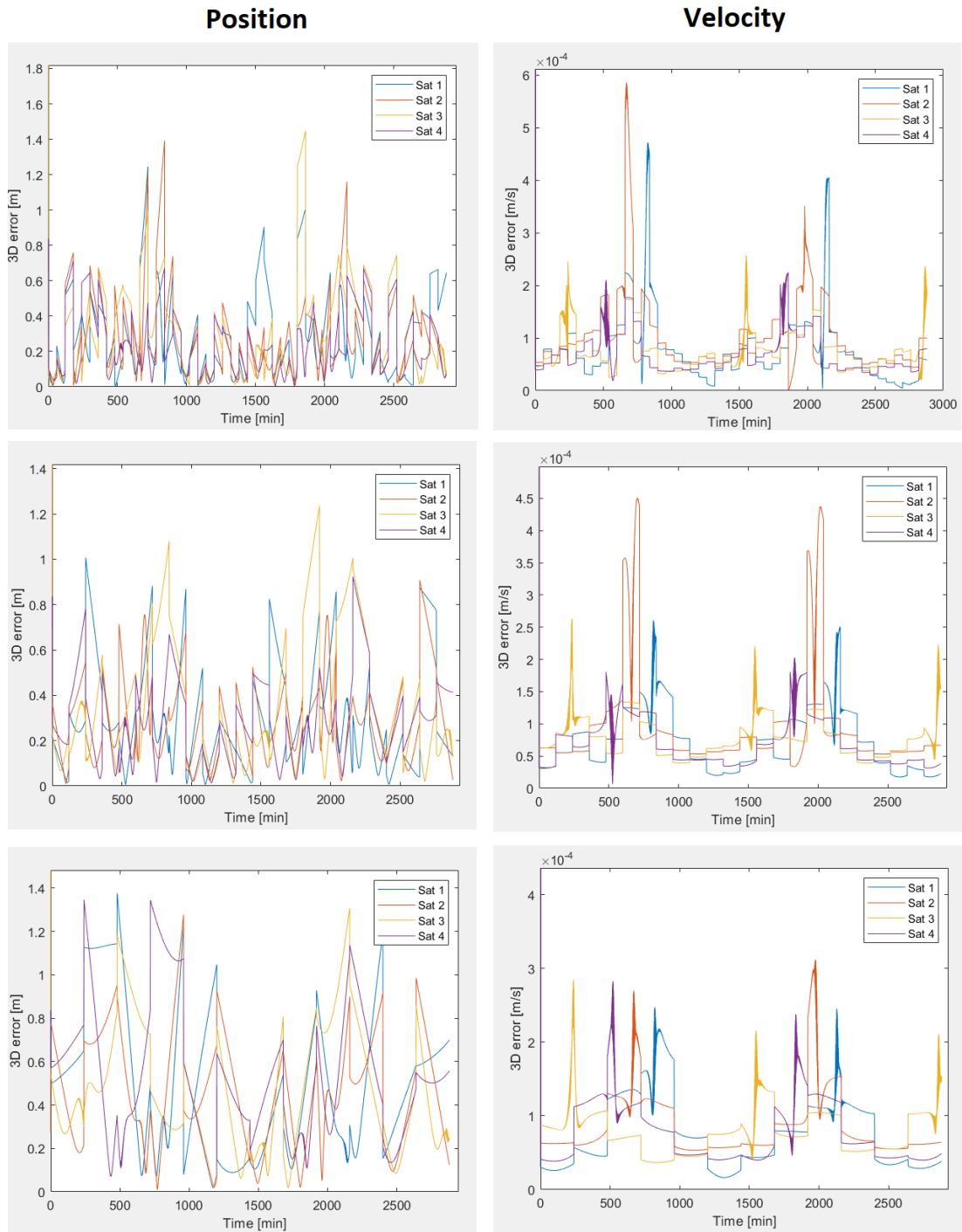


**Figure 4.27:** 3D position and velocity error for Keplerian scenario with 3 beacons, ISL, DSN and altimeter, long arch OD algorithm, 1 batch of observables per second and increasing time span from top to the bottom (1, 2 and 4 hours), 48h of simulation

Figure 4.26 illustrates the 3D error in position and velocity for the present scenario for increasing time span of 1, 2 and 4 hours and 1 batch of observables per minute. What is clearly noticeable is how during the tracking passes with the DSN, which, for this scenario, have been set to two 2-hours windows per day, the error is very low, well under 50cm.

Simulations for the same time spans were conducted for a higher data rate of 1 batch per second and are reported in Figure 4.27. As for the previous scenario without the DSN, a dramatic increase in the OD accuracy is observed with one batch of observables per second but in this latter case a lower time span yields slightly better results, but this should be confirmed with further statistical analysis like Monte Carlo simulations. Table 4.6 below resumes the 3D mean and maximum error for these time spans and data rates.

3D error		Position [m]		Velocity [mm/s]	
Data Rate	Time Span	Mean	Max	Mean	Max
1 batch/minute	1 h	1.49	5.64	0.14	1.19
	2 h	1.13	5.26	0.12	1.00
	4 h	0.85	5.37	0.09	0.97
1 batch/second	1 h	0.28	1.39	0.08	0.61
	2 h	0.30	1.31	0.08	0.46
	4 h	0.48	1.38	0.08	0.32

**Table 4.6:** 3D position and velocity errors comparison for different time spans and data rates for the scenario with 3 beacons, ISL, DSN and altimeter

In spite of the already good performances with the previous time spans, additional simulations were conducted to find a time span that would result in a more stable error, eliminating the peaks even with lower data rates. The strategy used was to select a time span sufficiently long so that it always included a DSN tracking window. With two 2-hours windows per day, this means having at least a time span of 12h. Simulations were conducted for 12h and 24h both for data rates of 1 batch per minute and 1 per second. As it can be seen from Figure 4.28 and 4.29 and from Table 4.7, increasing the data rate does not improve the OD accuracy, and the reason is that when such longer time spans are used, the effect of the variation of the geometry of the constellation overtime is vastly predominant over the increased number of observables in terms of benefit on the OD accuracy.

From all the results of the present section, it follows that a careful trade-off between computational effort, both in terms of execution time of the algorithm and memory required, and accuracy of the OD has to be carried out for the present

scenario.

3D error		Position [m]		Velocity [mm/s]	
Data Rate	Time Span	Mean	Max	Mean	Max
1 batch/minute	12 h	1.25	3.79	0.09	0.49
	24 h	0.91	2.00	0.08	0.62
1 batch/second	12 h	1.19	3.78	0.08	0.49
	24 h	0.91	1.99	0.08	0.49

**Table 4.7:** 3D position and velocity errors comparison for different time spans and data rates for the scenario with 3 beacons, ISL, DSN and altimeter

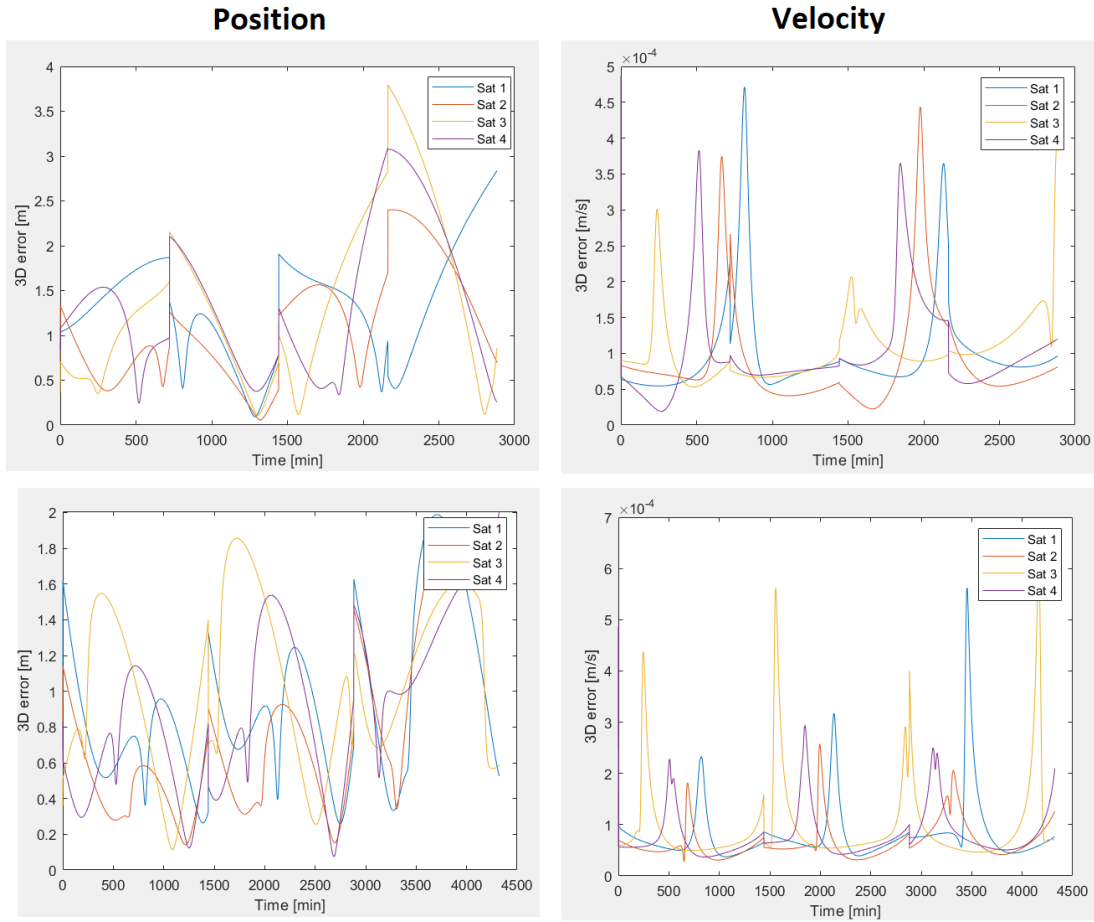


**Figure 4.28:** 3D position and velocity error for Keplerian scenario with 3 beacons, ISL, DSN and altimeter, long arch OD algorithm, 1 batch of observables per minute and increasing time span from top to the bottom (12 and 24h), 72h of simulation

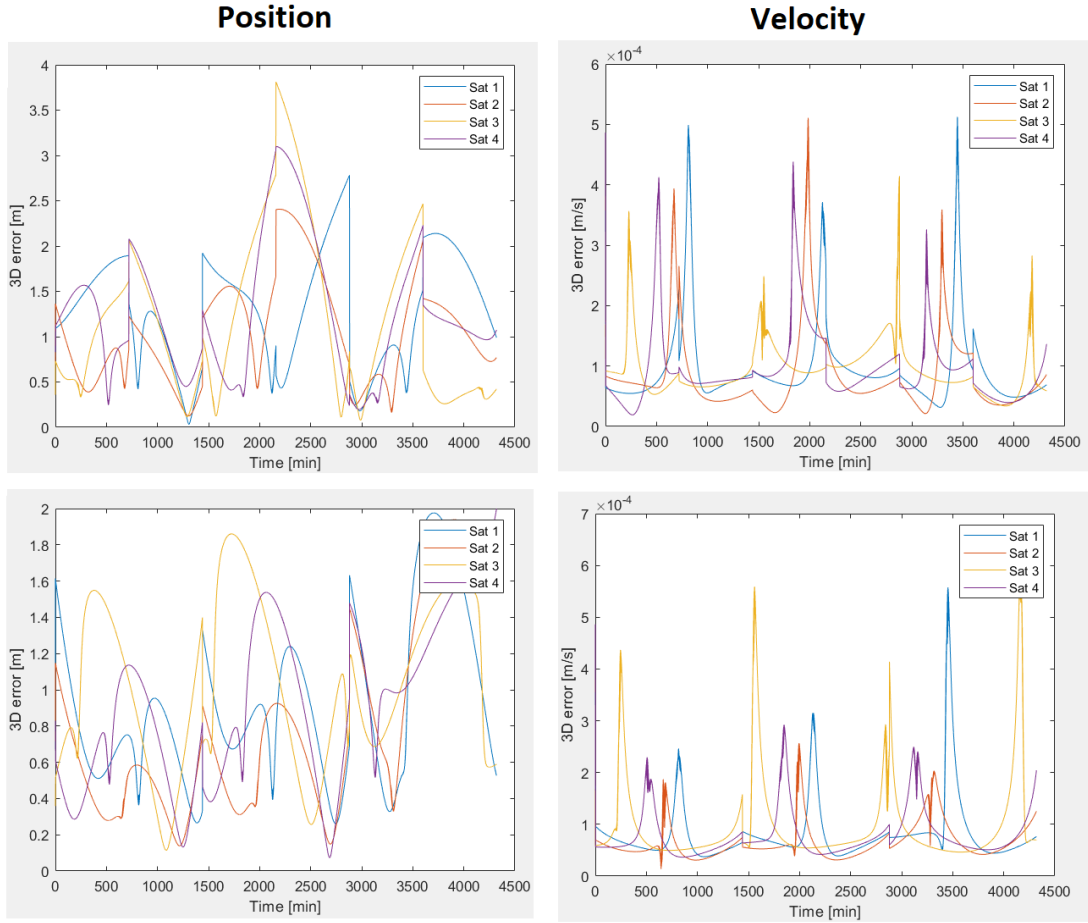


**Figure 4.29:** 3D position and velocity error for Keplerian scenario with 3 beacons, ISL, DSN and altimeter, long arch OD algorithm, 1 batch of observables per second and increasing time span from top to the bottom (12 and 24h), 72h of simulation

As expected, a more stable trend for the 3D error can be seen with the 24h time span, but it is worth to point out from the previous results that a slight increase in the data rate could provide the same error behavior (or even a more stable one) with time spans as short as 1 or 2 hours, providing a more frequent update for the trajectories at an overall restrained cost. This is further analyzed in chapter 5.

The same mission architecture was simulated for the perturbed scenario, using HPOP as propagator in the OD algorithm as for previous sections. The addition of DSN slightly improves the performances with respect to the previous scenario with the beacons, the cross-links and the altimeters when using the same time span. The 3D error in position and velocity for the present scenario is reported in Figure 4.30 for different time spans.

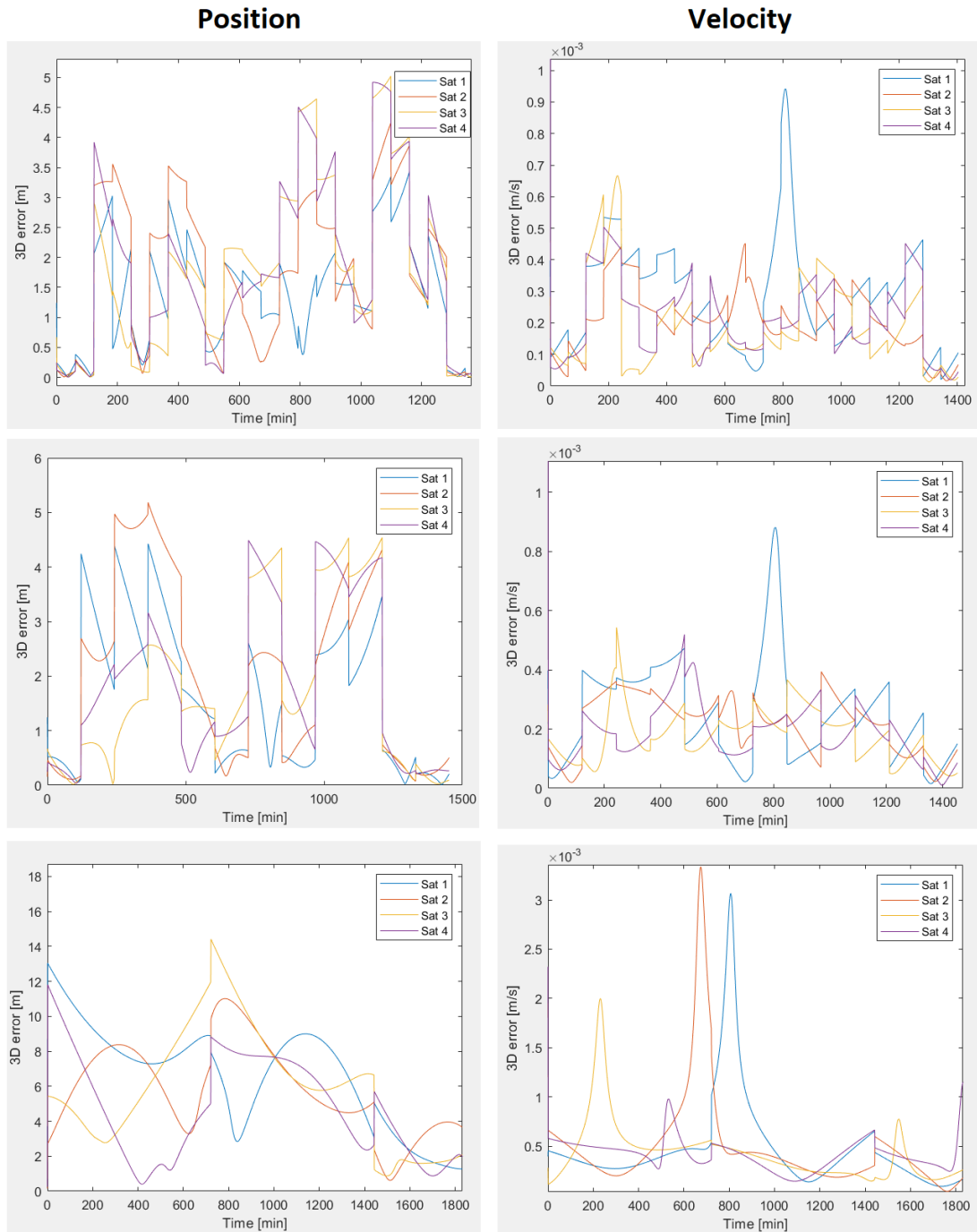


**Figure 4.30:** 3D position and velocity error for the perturbed scenario (dynamical model known) with 3 beacons, ISL, DSN and altimeter, long arch OD algorithm, 1 batch of observables per minute and increasing time span from top to the bottom (1h,2h and 12h), 24h of simulation

While all the perturbed scenarios were not simulated with higher data rates due to excessive computational effort ( which is also to be considered as a driver when implementing a high-fidelity dynamical model in the algorithm ), it is clear from 4.30 that, in this case, even better results could be obtained with 1 batch of observables per second. Indeed, this latter data rate would result in 3600 batches collected in an hour instead of only 60, averaging out the effects of noise while being only slightly influenced by the variation of the geometry of the constellation. The 3D errors in position and velocity for the present case are resumed in Table 4.8 below.

3D error		Position [m]		Velocity [mm/s]	
Data Rate	Time Span	Mean	Max	Mean	Max
1 batch/minute	1 h	1.65	5.02	0.22	0.95
	2 h	1.82	5.18	0.21	0.90
	12 h	7.14	14.8	0.47	3.34

**Table 4.8:** 3D position and velocity errors for different time spans for the perturbed scenario with 3 beacons, ISL, DSN and altimeter

As for all the mission architectures, with the perturbed ELFOs, short time spans lead to more accurate results, though it is worth to notice that in this last scenario, in spite of having a greater mean and maximum 3D error, the 12h time span case exhibits an overall more stable trend, which can be traced back to having at least one DSN tracking window per time span.

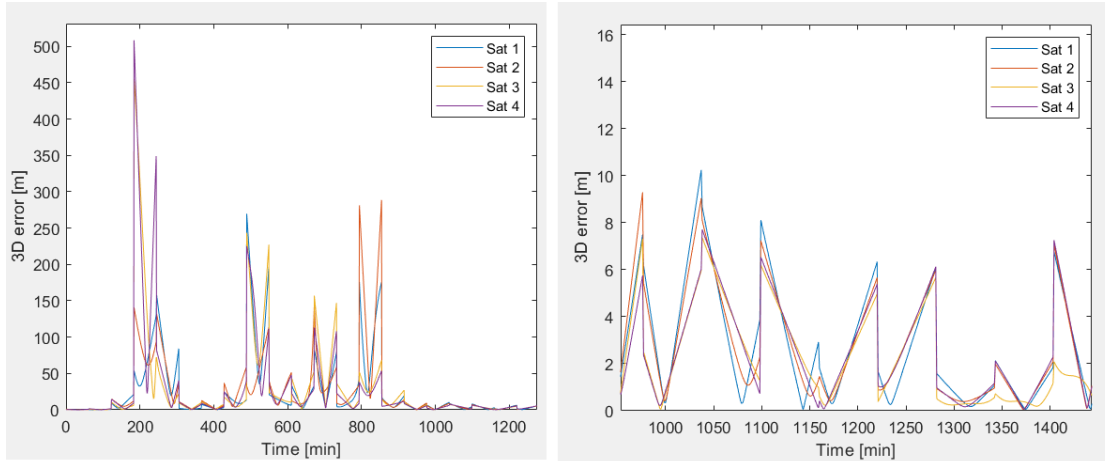


**Figure 4.31:** 3D position error (left) and detail (right) for the perturbed scenario (limited knowledge of dynamical model) with 3 beacons, ISL, DSN and altimeter, 1 batch of observables per minute , 24h of simulation

To conclude this section, as for the previous one the 3D error in position when limited knowledge of the dynamical model is known is reported in 4.31 above for completeness. A 60 minutes time span was selected taking into account the considerations of the precedent section. Indeed, the addition of DSN data yields better results with respect to the previous case, halving the peaks and maintaining a 3.5m mean error when many observables are available.

## 4.5 The use of GNSS

While the importance of the possibility of using GNSS for lunar navigation was illustrated both in chapter 1 and briefly in 3, the results of the simulations following from the hypothesis and assumption of section 3.4.2 are presented hereafter.

### 4.5.1 GNSS and altimeter

In the first simulated scenario from this section, in addition to the use of GNSS signals, the satellites exploited the on-board altimeter. The maximum number of observables available in thus is 8, with 4 ranges from the GNSS and 4 altimetric measurements. Instead, the minimum is 7, corresponding to one satellite losing direct LOS with Earth as reported in Figure 4.32. It is worth remembering that, for simplicity, the GNSS signals were simulated as a single observable collected by each lunar satellite as it was coming from a point source. This means that Moon's occultation is the only cause of loss of observables. The exclusion of the unavailable measurements has been carried out starting with the same procedure as for satellite-to-satellite LOS visibility from section 3.4.1 (Figure 3.4).

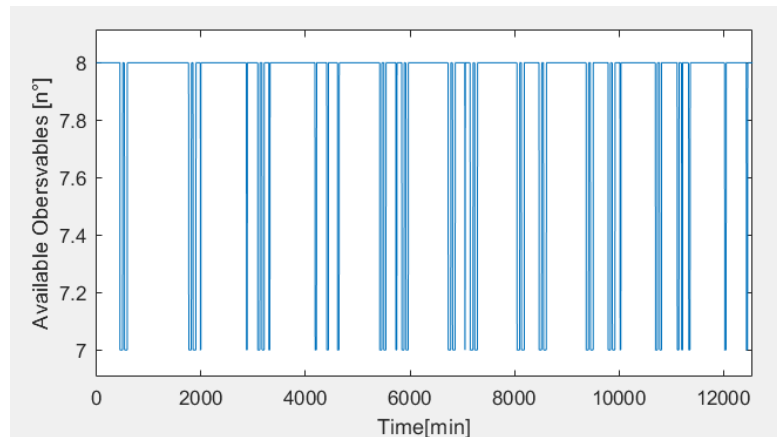


**Figure 4.32:** Number of observables available overtime for the scenario with Earth's GNSS and the on-board altimeter

The first simulations were conducted for the Keplerian case. Since the main source of observables available is the GNSS and considering the high distance from Earth, low data rates and long time spans were selected for the OD algorithm. Particularly, time spans of 24h, 48h and 72h were simulated with 1 batch of observables per second. Two different levels of noise were considered to assess the capabilities of the algorithm to handle them: firstly, lower standard deviations as  $\sigma_{altimeter} = 10cm$  and  $\sigma_{GNSS} = 1m$ , then higher ones as  $\sigma_{altimeter} = 20cm$  and  $\sigma_{GNSS} = 2m$ . The former case corresponds to the results in Figure 4.33, while the latter to the ones reported in Figure 4.34.

From these simulations, two main features of the OD algorithm can be inferred: first of all, as for the DSN and altimeter scenario, the longer the time span, the lower the 3D error and the more stable its trend; secondly, both qualitatively and quantitatively, as far as such long time spans are concerned, the increase in measurement noise does not worsen the OD performances. This is further clarified with the resume in Table 4.9 below.

3D error		Position [m]		Velocity [mm/s]	
Measurement noise	Time Span	Mean	Max	Mean	Max
$\sigma_{altimeter} = 10cm$ $\sigma_{GNSS} = 1m$	24 h	4.91	35.4	0.32	6.90
	48 h	2.09	7.98	0.18	2.25
	72 h	1.71	4.55	0.15	1.32
$\sigma_{altimeter} = 20cm$ $\sigma_{GNSS} = 2m$	24h	5.17	32.8	0.33	6.84
	48 h	2.04	7.83	0.18	2.12
	72 h	1.73	4.78	0.15	1.27

**Table 4.9:** 3D position and velocity errors comparison for different time spans and noise levels for the Keplerian scenario with the GNSS and altimeter. Data rate is set at 1 batch of observables per minute.

Following that, Figure 4.35 illustrates the 3D error in position and velocity for the perturbed scenario when using HPOP in the OD algorithm, i.e., being the dynamical model known. Quite high both medium and maximum errors can be observed in position and velocity as well and the variation of the performances with the time spans does not show a clear pattern. Indeed, in the previous sections it was shown that with the perturbed ELFOs shorter time spans worked better, but in the present scenario that strategy could not be followed: in fact, as for the DSN, GNSS signals, due to the large distance of their source, need longer time spans to allow the geometry of the lunar constellation to change enough to diversify the batches of data and yield a good estimate.

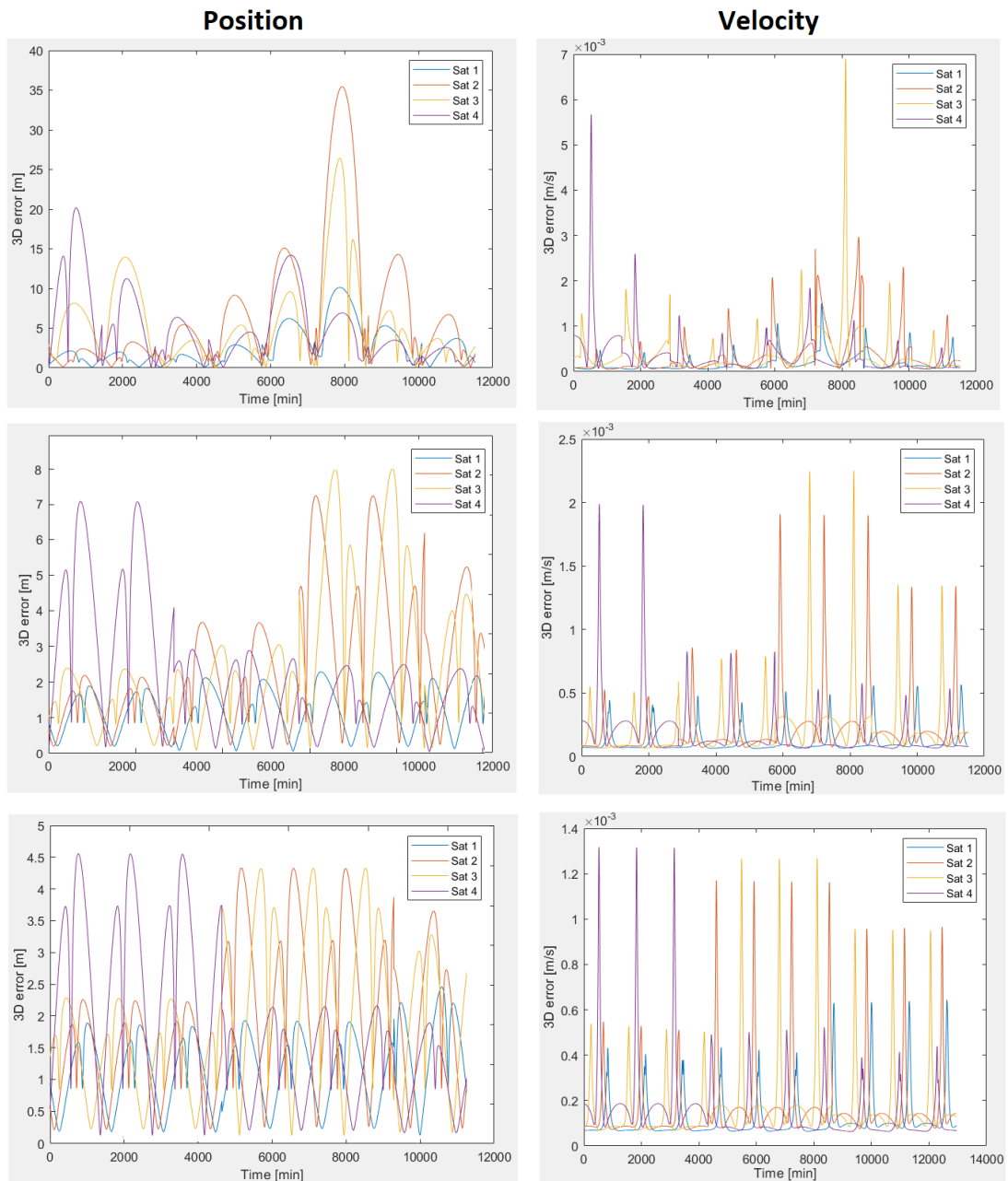


**Figure 4.33:** 3D position and velocity error for Keplerian scenario with GNSS and altimeter, long arch OD algorithm, 1 batch of observables per minute and increasing time span from top to the bottom (24, 48 and 72 hours), 8 days of simulation. Lower level of noise.

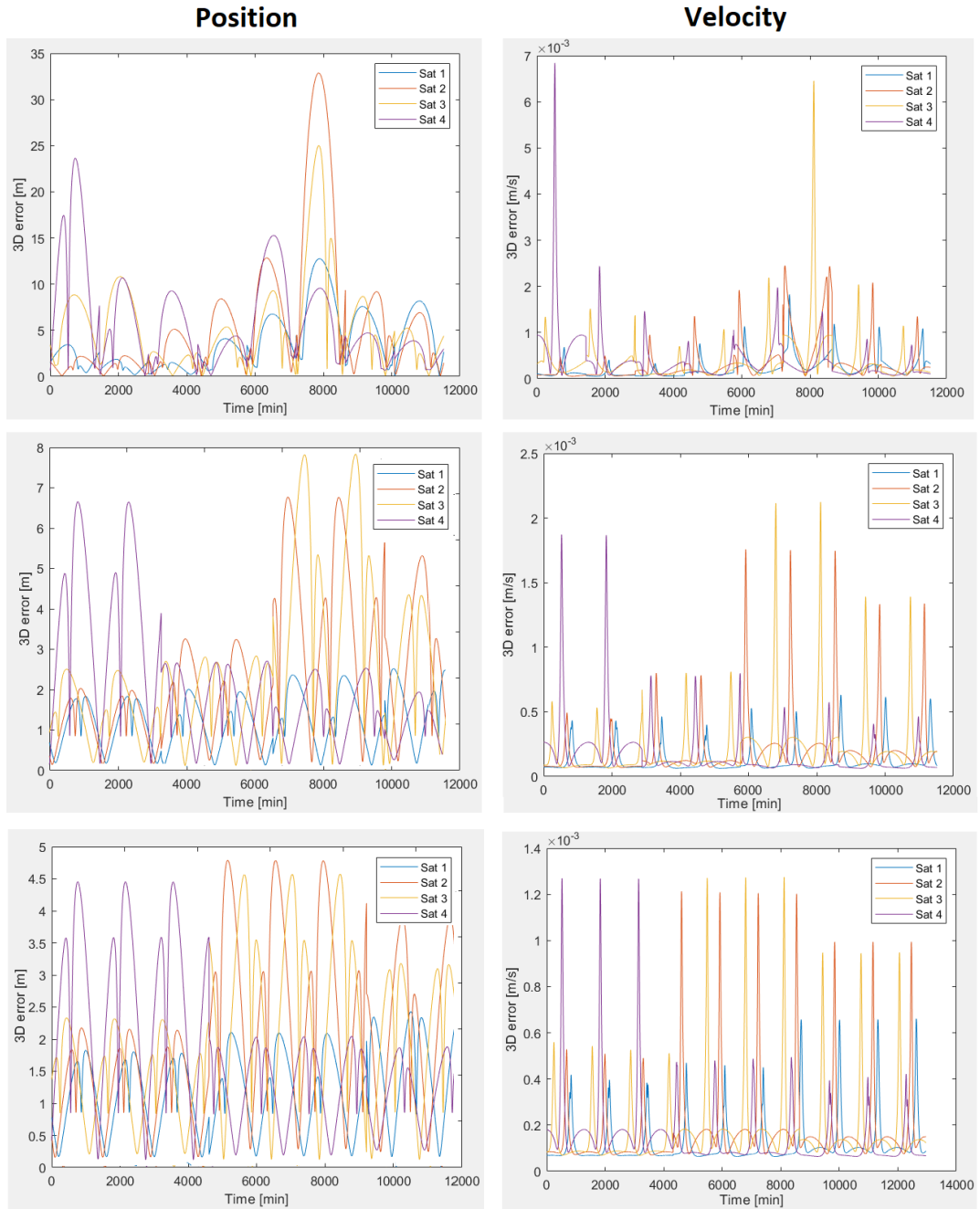


**Figure 4.34:** 3D position and velocity error for Keplerian scenario with GNSS and altimeter, long arch OD algorithm, 1 batch of observables per minute and increasing time span from top to the bottom (24, 48 and 72 hours), 8 days of simulation. Higher level of noise.

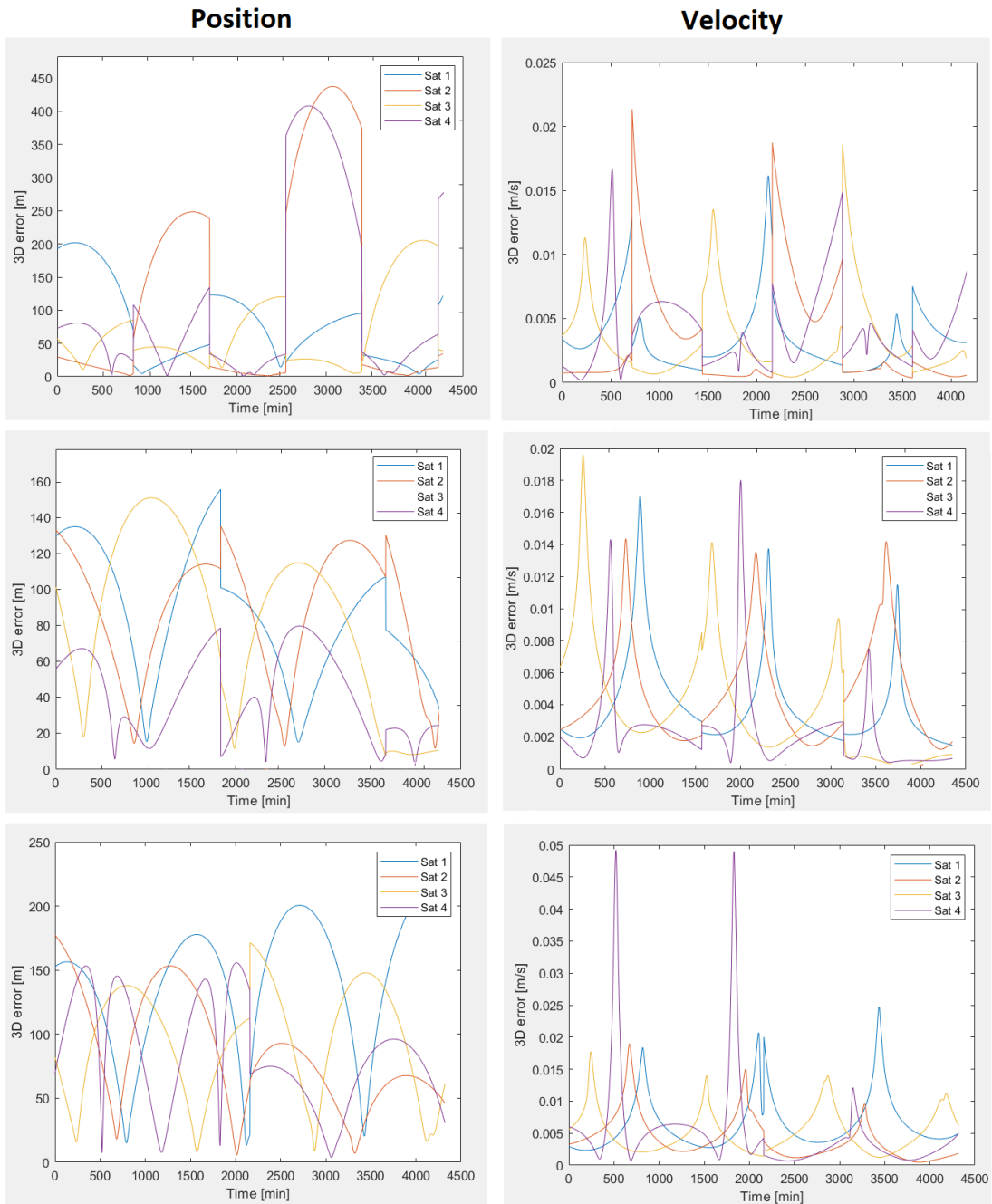


**Figure 4.35:** 3D position and velocity error for the perturbed scenario with GNSS and altimeter (dynamical model known), long arch OD algorithm, 1 batch of observables per minute and increasing time span from top to the bottom (12, 24 and 36 hours), 3 days of simulation.

The issue with this last perturbed case is in the time span as anticipated. Since the dynamical model is known though, one could expect to see a similar trend as for the unperturbed scenario. The fundamental difference here lies in the properties of the ELFOs. In the previous chapters, particularly in section 1.3.2, the stability of these orbits under the effect of perturbations was illustrated referring to several precedent researches, particularly from Ely's work [20]. What these studies point out is that a fine tuning of the initial Keplerian parameters has to be carried out in order to have a frozen orbit. Being the initial guess in position and velocity quite inaccurate, this results in a reference trajectory rather different from the real one, which implies a rapid divergence of the two due to the unbalanced perturbations. In turn, this makes the algorithm diverge quickly for an excessively long time span.

In spite of this, the addition of more observables tends to increase the OD performances as the geometry of the constellation changes. This leads to an optimal time span of around 24h as a trade-off between these two opposed influences.

#### **4.5.2 GNSS, DSN and Altimeter**

While the Keplerian scenario with GNSS and altimeter yielded accurate results, the perturbed scenario demonstrated a high sensitivity to both initial guess and variation of constellation geometry. This led to the further addition of the DSN stations in the simulated environment in order to try to mitigate these influences. Firstly, Figure 4.37 reports the 3D error in position and velocity for the Keplerian case when adding the DSN, then Figure 4.38 illustrates the perturbed case when using HPOP as dynamical propagator.

What is clear from both those figures is that the addition of the DSN does not solve the issue of the previous section. Two main factors come into play. First of all, DSN is only limited to two 2-hours windows of tracking per day, which means that a 24h time span would be needed at minimum to collect observables from two passes, which generally improves a lot the OD but in the perturbed case it suffers from the rapid divergence of the reference trajectory from the true one. On the other hand, there is a subtle downside coming from the GNSS modelization, following from the assumptions and hypothesis of this work, when using it alongside the DSN: the GNSS signals were simulated as coming from a point source placed in Earth's center of mass and only providing range data; since the DSN antennas are located on Earth's surface and the distance between Earth and the Moon is far greater than the one between Earth's center of mass and the DSN antennas, the range data from the DSN stations is numerically very close to the range data from the GNSS. This means that the addition of the DSN provides only unique range-rate measurements and worsen the conditioning of the  $\Lambda$  matrix due to the presence of almost equal rows

in the observations-state relation matrix  $H$  corresponding to GNSS and DSN ranges.

It is important to point out that these conclusions only come from the hypothesis and assumptions of the present work. Indeed, using a complete model of the GNSS constellations and considering the clock errors for all the observables, would yield different results: a complete model of the GNSS constellations would largely diversify the observables collected in lunar environment, making unique range-rate data available for OD which were not modelled in the present work and furthermore increasing the relative distance between the GNSS signal sources and the DSN antennas of thousands of kilometers as the real GNSS orbits are Medium Earth Orbit (MEO) with an altitude of around 20.000km, improving the quality of the range measurements as well as they diversify between the two sources; on the other hand, clock errors for the GNSS would be extremely worse than the ones from DSN, this latter exploiting a two-way ranging while the former being one-way. Therefore, a clear advantage should be got from adding the DSN when compared to the GNSS and altimeter only scenario, but this is not noticeable with the present assumptions.

Moreover, high levels of noise are to be expected from GNSS signals with the side lobes of the pattern of their antennas not being developed for navigation purposes at altitudes as high as Moon's, thus the standard deviations of measurement noise considered in the present work may be rather optimistic.

Finally, Figure 4.36 below illustrates the number of observables collected overtime for the present scenario. The maximum amount of measurements simultaneously available per epoch is 24, corresponding to data from two DSN stations (16), the GNSS (4) and the on-board altimeters (4), while the minimum is 7 as for the previous case when the DSN is not tracking the constellation.

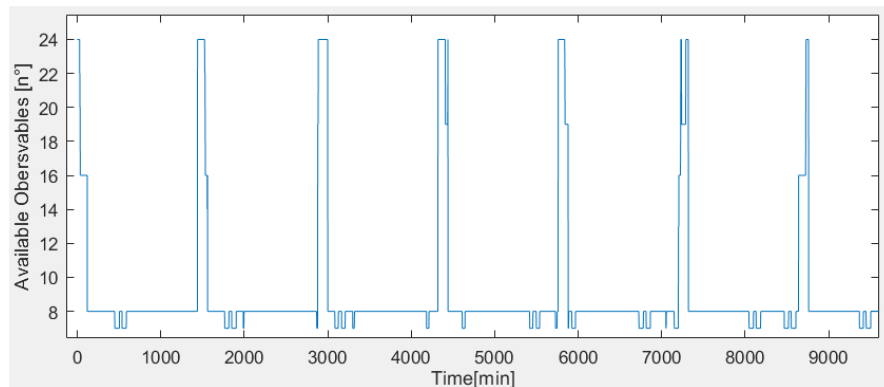


**Figure 4.36:** Number of observables available overtime for the scenario with Earth's GNSS, DSN and the on-board altimeter

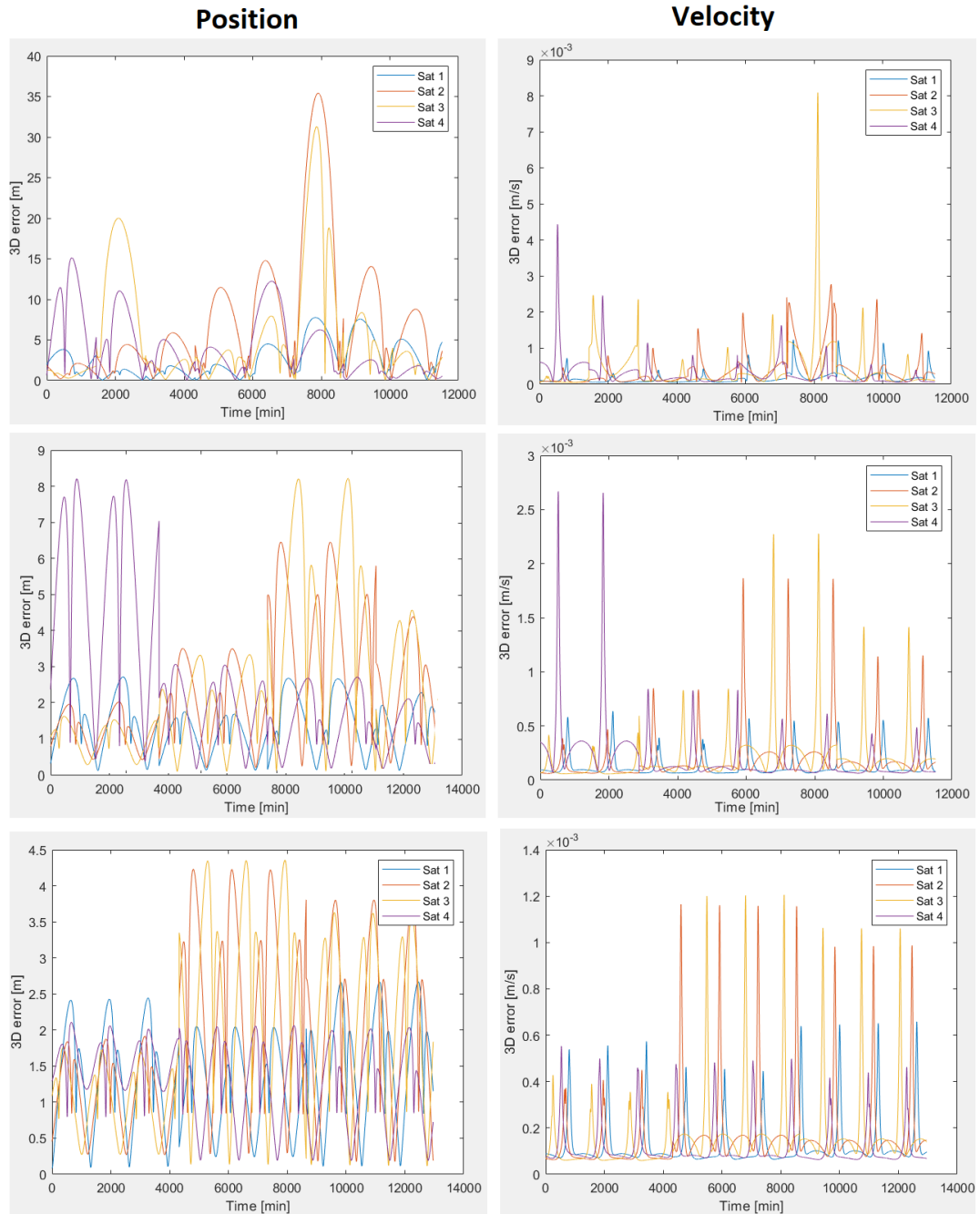


**Figure 4.37:** 3D position and velocity error for Keplerian scenario with GNSS, DSN and altimeter, long arch OD algorithm, 1 batch of observables per minute and increasing time span from top to the bottom (24, 48 and 72 hours). 8 days of simulation.

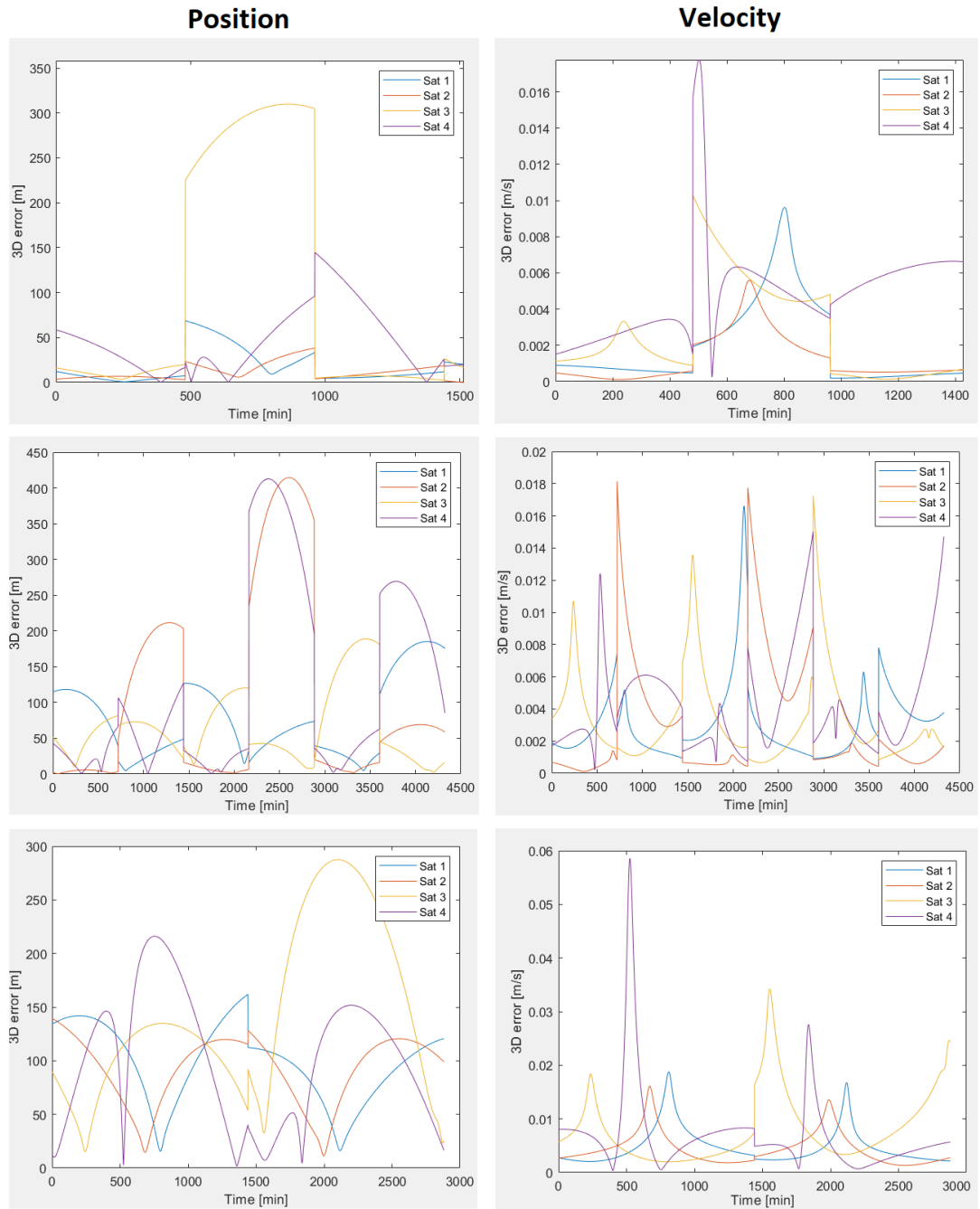


**Figure 4.38:** 3D position and velocity error for perturbed scenario with GNSS, DSN and altimeter, long arch OD algorithm, 1 batch of observables per minute and increasing time span from top to the bottom (8, 12 and 24 hours). 8 days of simulation.

For this last scenario, the standard deviations of measurement noise was set as follows:  $\sigma_{altimeter} = 10cm$ ,  $\sigma_{GNSS} = 1m$ ,  $\sigma_{DSN-range} = 0.6m$   $\sigma_{DSN-range-rate} = 0.03mm/s$ .

Table 4.10 below resumes the 3D errors in position and velocity of the present scenario for both the Keplerian and the perturbed cases.

3D error		Position [m]		Velocity [mm/s]	
Measurement noise	Time Span	Mean	Max	Mean	Max
Keplerian	24 h	4.84	35.4	0.32	8.09
	48 h	2.15	8.21	0.18	2.67
	72 h	1.62	4.35	0.14	1.21
Perturbed	8h	66.5	686.6	2.78	14.6
	12h	91.7	414.6	3.36	18.2
	24h	108.1	287.4	6.03	58.6

**Table 4.10:** 3D position and velocity errors comparison for Keplerian and perturbed scenarios with GNSS, DSN and altimeter. Data rate is set at 1 batch of observables per minute.

# Chapter 5

## Trade-off analysis

While the different implementations of the present work followed the scalability logic of the lunar PNT system from ESA's roadmap, several aspects have to be considered and traded-off in the design of the optimal architecture for a lunar satellite navigation system.

The following indicators are considered fundamental drivers:

- Orbit determination accuracy
- System complexity
- Algorithm complexity

The OD accuracy is clearly cardinal. The final purpose of the lunar PNT system is to provide a final user with navigation messages containing the ephemerides of the constellation in order to allow them to autonomously calculate their position and clock informations. The better the OD accuracy, the more precise the final user position will be. Since various maneuvers like rendez-vous, docking and landing and most of the manned operations require high positioning precision, it is necessary to accurately know the constellation state vector from the orbit determination process. Key performance indicators like the 3D error considered in this study, both in terms of mean and maximum entity, overall trend and stability, are primary to assess the feasibility of the algorithms for the considered architecture.

Generally, the more complex a system becomes, the most performing it will be. While this is true for most of the cases, a high increase in complexity does not necessarily correspond to a high increase in performance since the more elaborated a system gets, the harder it is to further improve it. This generally leads to a trade-off. For the present case, the mission architecture could range from as simple

as based on DSN tracking only to the most complete configuration with lunar beacons, inter-satellite links, on-board altimeters and even eventual ranging from the Lunar Gateway (this latter not considered here for the reasons explained in 3.4). The choice of the data rates and orbit update intervals also contribute to the complexity of system design.

The choice of the parameters of the algorithm that has to perform the OD is also to be traded-off. Implementing complex dynamical models for example, though yielding more accurate results, could dramatically increase the computational effort and time (most of which is related to the ODE integration). Likewise, batches from high data rates could require large memory occupation and since it is not clear what the actual final OD computational processor will be, the effective specifications and complexity of the algorithm are yet to be determined.

## 5.1 DSN tracking

When performing OD with deep space antennas tracking the lunar navigation constellation, as explained in the previous chapters, the algorithm performances do not change with higher data rates due to longer periods required for a variation in the geometry of the constellation as seen from the tracking stations. This, in turns, implies that longer time spans are mandatory using a batched least squares algorithm, the duration of which is highly dependent on the tracking windows availability from the DSN/ESTRACK.

The results of section 4.1 and 4.2 tells that it is preferable to have shorter tracking windows distributed overtime with respect to longer but infrequent ones. This is not due to lower 3D errors when using the same time span but because rather accurate OD can be performed within fewer days as Table 4.2 demonstrates.

Another way to interpret this latter consideration is that if the update of the orbits is needed to be performed only as infrequently as every 6 or 7 days, there is no advantage in using so many shorter tracking windows that would only result in much more memory and time consuming computations while not improving the OD performances.

It is worth noticing though that when considering a perturbed scenario, as seen in section 4.5, shorter time spans benefit from limited drift of reference trajectories from true orbits, meaning the optimal solution for this case is in fact using several shorter tracking windows that result in both adequate OD performances and more frequent orbit update capabilities.

## 5.2 The autonomous lunar navigation system

A crucial step in the PNT roadmap implementation is the conversion of the lunar navigation system in an autonomous architecture independent of Earth's support. This phase of the Moonlight initiative is likely to be reached with the introduction of surface beacons and exploitation of satellite cross-linking.

In section 4.3 and 4.4 detailed analysis of the OD algorithm performances were carried out together with an assessment on the influence of initial guess, time spans, data rates, observability and dynamical models. Taking all the results into account, the following conclusions can be inferred on the mission architecture:

- If the altimeter will be present on-board as expected, there is not a significant quantitative nor qualitative advantage in having three beacons at the Moon's South Pole instead of two from an OD accuracy point of view. The state vector is observable in both cases and the mean and maximum 3D errors are of the same magnitude. It is worth to point out though that from a system redundancy standpoint, the more the beacons, the most reliable the system. That being considered, in a phase 2 PNT implementation as from ESA's roadmap, two beacons could allow adequate OD performance, while in a phase 3 full autonomous and established PNT system, three beacons would provide additional robustness to the system.
- If a third beacon could be placed far from the South Pole, an important increase in the performances of the OD process are likely to be reached as from the analysis in 4.3, which is to be evaluated in detail. Besides the difficulties in the collocation process, a major drawback would clearly be the servicing logistic as the lunar surface base would be far from it.
- The addition of the DSN tracking to the autonomous navigation system composed of beacons, ISL and altimeters, does not significantly improve the OD performances. While DSN or ESTRACK support will be paramount in the first phases of Artemis, both as primary navigation mean or eventually complementing GNSS-based navigation, once the lunar autonomous system will be established, Earth's based assets like DSN antennas could become secondary, relaxing tracking scheduling requirements. Nevertheless, as earlier mentioned, in spite of hypothesizing that dual one-way ranging techniques could be used in the satellite cross-links, clock errors would play a key role in the OD&TS process and performances, making two-way ranging from Earth's deep space antennas a reliable source of clock-free observables that could effectively improve the navigation accuracy.

The time span influence was explored in detail in Chapter 4. To summarize

it, in the Keplerian scenario the OD performances would generally increase with longer time spans, while in the perturbed cases an optimal time span would result from a trade-off between reference trajectory divergence from the real one and increasing amount of observables with longer time spans. That being considered, the following aspects are worth pointing out:

- The optimal time span to use in the algorithm must respect PNT service requirements including maximum orbit update intervals depending on maximum ephemeris validity time. For instance, it is assessed in [84] that for the Galileo constellation "The maximum nominal broadcast period of a healthy navigation message data set is currently 4 h". For a lunar navigation constellation this parameter is yet to be defined and will pose an important constraint on the maximum time span for OD.
- Since longer time spans would imply higher computational effort, their duration should be traded-off considering effective memory capabilities and calculation time in a detailed quantitative analysis.

For what concerns the data rates to be used, it is clear from the results of 4.3 that higher rates yield more accurate results, but they carry a high computational cost, both in terms of memory required for storing and processing numerous batches of observables and effective computational time. When OD is performed using beacons, ISL and altimeters, 20 to 30 cm of average 3D error are reached with rates as high as 1 batch of observables per second, while meter-level accuracy can be expected from data rates of 1 batch per minute. The following considerations can therefore be made:

- In the first phases of the PNT service implementation, lower data rates could be feasible and provide rather accurate trajectories at a significantly lower system complexity and computational effort. A compromise rate between 1 batch per minute and 1 batch per second should be further investigated in terms of advantages and drawbacks on the OD process. A third phase scenario instead would largely benefit from higher data rates for accuracy and reliability that could be paramount, for instance, in high precision landings or manned operations.
- The use of higher data rates can reduce the time span needed to achieve a certain OD accuracy. Indeed, considering for example 4.3 it is clear that a 30 minutes time span at 1 batch of observables per second, resulting in 1800 batches collected, provides more accurate results than a 90 minutes time span at 1 batch per minute (90 batches collected). The reasons why this could be important were previously explained.

### 5.3 About the use of GNSS

Due to the choice in the modeling of the observables from the Earth's GNSS, as pointed out in section 4.5.2, there is a certain equivalence in the considerations made for the DSN and the ones for the use of GNSS. Very similar performances are obtained in the Keplerian scenario with similar time spans in spite of the important difference between the availability of the two sources: GNSS is considered to provide observables at all times unless Moon's occultation come into place while DSN must respect scheduled tracking windows.

That being said, as anticipated for the DSN, since the data rates are irrelevant for what concerns OD accuracy, the only parameter to be traded off is the time span which was found to be optimal, for the specific perturbed scenario, at a value of around 24h.

Note that all the present and previous considerations directly follow from the hypothesis and assumptions of this work expressed in chapter 3 and do not consider all the possible constraints of the constellation design or different choices of the algorithm as further explained in the next chapter.

# Chapter 6

## Summary and conclusions

Several scenarios have been simulated trying to retrace ESA's PNT implementation roadmap in designing a scalable architecture for a lunar satellite navigation system. Insights were achieved into observability, measurement noise effect, importance of force models and into the relative importance and influence of different observables available in each scenario. The orbit determination algorithm implemented, based on a batched least squares solution, proved to efficiently handle initial guess errors and measurement noise and, even with simplified dynamical models, yielded accurate results in the non-Keplerian scenarios when sufficient observables were available.

### 6.1 Future work and recommendations

A critical aspect to further investigate is the OD when at least one satellite has no longer LOS communication with the others and with the beacons. Theoretically, it would be possible to change the ISL contacts so that the remaining three spacecrafts track each other when the fourth transit over the lunar North Pole: this way, considering for example a mission architecture with 3 beacons, ISL contacts and on-board altimeter, when one satellite reaches its periselene, the other three can still rely on 27 observables (18 from the beacons (6x3), 3 from the altimeters and 6 from the three cross-links) and solve for a reduced state vector of 18 unknown, corresponding to their position and velocities. The state vector of the fourth satellite could be propagated through the most accurate dynamical model available for the around 4 hours when it overflies the North Pole in order to provide a sufficiently accurate initial state vector guess for the successive OD with all satellites in view of the beacons. Further works will have to assess the feasibility of such a solution or propose others. Nevertheless, it is clear that using dual one-way ranging from ISL would not be an easy task even without changing the "order" of the links, thus may

not be possible, at least in the first phases of the Moon campaign, to have this technology readiness level.

It is also worth to point out that the orbit prediction phase following the determination of the state vector at some initial epoch was introduced to reduce the computational cost on the processor that will eventually execute the OD algorithm but, though having demonstrated good performances, it is not to be excluded that using a classical BLS exploiting batches of measurements to solve for every single epoch could improve the OD performances.

Furthermore, the use of a batched least squares, though feasible, may not be the best solution for the orbit determination of the lunar navigation system constellation. A sequential estimator based on an Extended Kalman Filter is certainly a good candidate for the future implementations. This latter could be extremely suitable for near real-time orbit estimation that could always guarantee updated trajectories to the final user of the navigation service. Again, a crucial point in this case would be handling the update when a satellite loses contact with the others and with the beacons.

Though hypothesis and assumptions were made regarding the clock free observables when using dual one way ranging with ISL, and using two-way ranging with DSN stations, further considerations and a detailed analysis of the validity of these assumptions have to be carried out to pinpoint the critical aspects of the time synchronization problem. Indeed, as it was already pointed out in section 4.5, differentiating one-way and two-way measurements with realistic clock errors would provide fundamental insights into the improvements of exploiting different sets of observables. It has to be considered as well that, besides clock errors, generally, some additional parameters, like gravitational spherical harmonics coefficients, has to be estimated in the OD&TS process with position and velocities of the constellation, meaning that increasing the observables (for instance, adding a third surface beacon) could be necessary to have observability of that extended state vector.

Another suggested topic for further improvements is to use covariance matrix analysis to achieve insight into the statistical behavior of the OD errors. This was not done in this work preferring to focus on the 3D error trend, being this latter the most direct way to assess OD performances. Monte Carlo analysis with different initial guesses and levels of measurement noise should also be considered for statistical purposes though being a very time consuming approach.

Moreover, as already explained in section 3.7, an evaluation of SISE is fundamental to determine the effective requirements of OD accuracy, since it is that error that ultimately has an impact on the performance of the PNT system.

From a numerical point of view, as suggested in section 4.3.1, an approach based on Tikhonov-Phillips regularization for the ill conditioned least squares problem could potentially lead some benefit in the OD solution both in terms of algorithm stability and overall accuracy.

Finally, while a detailed modelization of Earth's GNSS signals reaching the Moon was out of the scope of this work, some simulations were conducted to assess the possible effect of measurement noise when using those signal for OD purposes. If Lunar Pathfinder mission is successful, the use of Earth's GNSS for navigation purposes in lunar environment will be a reality. Given the importance of this source of observables, a further work will need to go deep into a detailed simulation of those signals and their impact on OD.

# Appendix A

## Software tools

The two main software used in the simulations and OD implementation are MATLAB and AGI's System Tool Kit (STK). While in sections 3.1, 3.2 and 3.3 some of the specifications and parameters used both in STK and in MATLAB environment were presented, a brief overview of the tools used from the two software is given hereafter. Figure A.2 illustrates the interconnections of the tools used in the present work: the true (simulated) positions and velocities of the ELFOs were generated through STK as well as the timetables for the locations of the lunar beacons and of the DSN antennas; those were provided to a MATLAB routine which generated the observables and then performed the OD exploiting Moon's HPOP from STK. The performances were eventually assessed comparing the trajectories calculated in MATLAB and the simulated ones from STK.

### A.1 STK

STK is a software for complex 3D simulations and analysis of ground, air, space and sea platforms. Dynamical models and geometric evolution overtime are at the core of the software.

For the present work, a reduced Solar System with the Earth, the Sun and the Moon as main bodies was simulated. The four satellites of the lunar navigation system were simulated through Moon's HPOP, a precise dynamic propagator whose specifications were given in section 3.3. HPOP was also exported to MATLAB environment to be used in the OD algorithm. The positions and velocities of the DSN stations on Earth and of the three beacons at the Moon's South Pole were also propagated in the Moon Inertial reference frame and extracted as timetables to be imported in MATLAB. Even though the observables could be directly derived from STK, it was preferred to calculate them time by time in MATLAB through

user-defined functions to both avoid continuous and time consuming data import and export between the two software and have a fast and complete control over all the simulated parameters like measurement noise.

## A.2 MATLAB

MATLAB is a programming and computing software used in engineering and science and many other fields. Its most important feature is providing hundreds of built-in functions ranging from simple stationary point research to complex Fourier transform.

To give an overview of some of the built-in functions used for the present work: the data import from STK time tables was carried out through MATLAB's "readmatrix"; preliminary integration tests of the equations of motion were conducted with "ode45" routine, based on the Dormand-Prince method; "chol" function was used for the Cholesky decomposition of the least squares normal equations; the backslash operator for solving linear systems of equations was used to calculate the state deviation vector (this powerful tool analyses the system coefficient matrix and exploit different solution methods accordingly); as explained in section 3.4.6, measurement noise was generated through "Randn" routine which generates normally distributed random numbers with mean zero and variance and standard deviation equal to one. Nevertheless, most of the functions used in the algorithm were specially defined for the case study as the ones for eliminating the unavailable observables described in section 3.4. An example of these latter is given in Figure A.1 for the rise-set function evaluation as presented in section 3.4.1.

```

%% Satellite-to-satellite visibility
function [vis] = sat_to_sat_vis(X1,X2) %X1 and X2 being the state vectors
m=length(X1(:,1));
S=1738; %Mean lunar radius
R=zeros(1,m);
    for i=1:m
        r1=X1(i,1:3); %Position vector of satellite 1
        r2=X2(i,1:3); %Position vector of satellite 2
        R(i) = dot(r1,r2)^2-norm(r1)^2*norm(r2)^2+(norm(r1)^2+norm(r2)^2)*S^2 ...
            -2*S^2*dot(r1,r2); %Rise-set function evaluation
    end
vis=R<0; % Satellites have clear LOS if R<0
end

```

**Figure A.1:** Implementation of the rise-set function of section 3.4.1

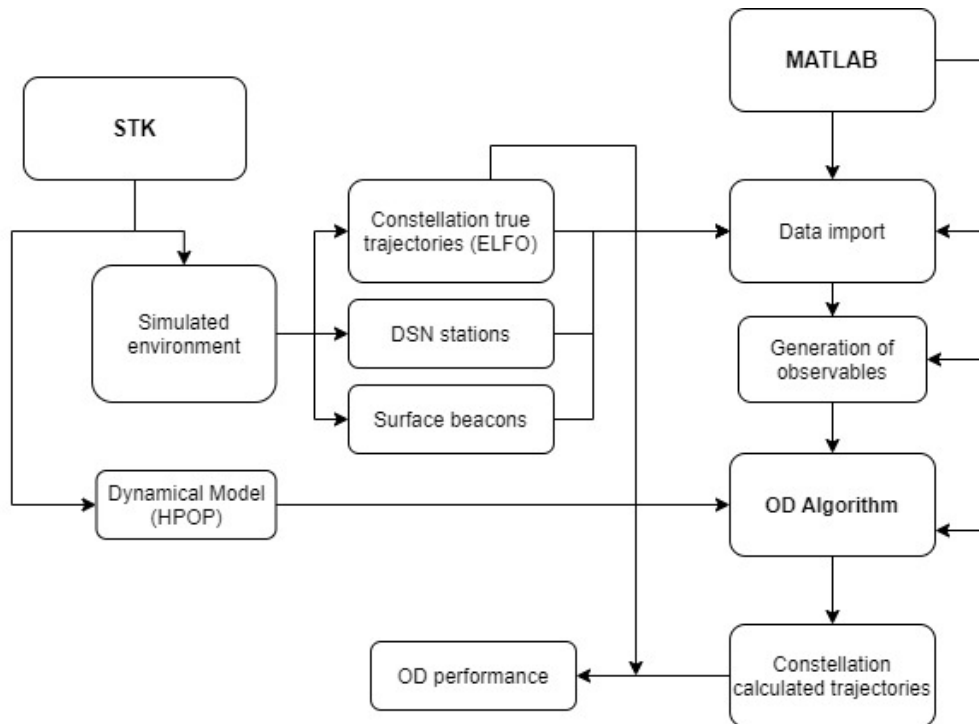


**Figure A.2:** STK and MATLAB interconnections in the present work

# Appendix B

## The State Transition Matrix

In section 2.3.1 the state transition matrix was introduced as a differential operator used for mapping deviations in the state vector  $X$  from one epoch to another. Recalling its definition from (2.3.12):

$$\Phi(t, t_0) = \left[ \frac{\partial X(t)}{\partial X_0} \right]$$

the following properties can be demonstrated [25]:

$$\Phi(t_k, t_k) = I \tag{B.0.1}$$

$$\Phi(t_i, t_k) = \Phi(t_i, t_j)\Phi(t_j, t_k) \tag{B.0.2}$$

$$\Phi(t_i, t_k) = \Phi^{-1}(t_k, t_i) \tag{B.0.3}$$

### B.1 Analytical solution for the perturbed case

As pointed out in (2.3.17), in the most general case  $\Phi$  must be solved for with the dynamical model matrix  $A$  defined in (2.3.6). Nevertheless, as anticipated, an analytical solution for the state transition matrix was proposed in [33] for the perturbed case that could take into account J2 effect. The reason behind this approach is trying to avoid the high computational cost of solving the (2.3.17) which, for example, for the present work, consists in solving 600 coupled ODE (24x24 elements of the state transition matrix coupled with the 24 equations of motion). This is clearly extremely limiting in terms of computational time when using complex dynamical models in which numerical approximations of the Jacobian

matrix has to be calculated. The analytical solution proposed in [33] is the following:

$$\Phi(t, t_0) \approx \begin{bmatrix} \Phi_{rr} & \Phi_{rv} \\ \Phi_{vr} & \Phi_{vv} \end{bmatrix} \quad (\text{B.1.1})$$

with the following definitions:

$$\begin{aligned} \Phi_{rr} &= I + (2G_0 + G) \frac{(\Delta t)^2}{6} \\ \Phi_{rv} &= I \Delta t + (G_0 + G) \frac{(\Delta t)^3}{12} \\ \Phi_{vr} &= (G_0 + G) \frac{\Delta t}{2} \\ \Phi_{vv} &= I + (G_0 + 2G) \frac{(\Delta t)^2}{6} \end{aligned}$$

and:

$$\begin{aligned} \Delta t &= t - t_0 \\ G_0 &= G(t_0) \end{aligned}$$

where  $I$  is the 3x3 identity matrix and  $G$  is the gradient matrix of partial derivatives of the total acceleration acting on the satellite and it is defined as:

$$G(t) = \frac{\partial a(r, t)}{\partial r} = \begin{bmatrix} \frac{\partial a_x}{\partial x} & \frac{\partial a_x}{\partial y} & \frac{\partial a_x}{\partial z} \\ \frac{\partial a_y}{\partial x} & \frac{\partial a_y}{\partial y} & \frac{\partial a_y}{\partial z} \\ \frac{\partial a_z}{\partial x} & \frac{\partial a_z}{\partial y} & \frac{\partial a_z}{\partial z} \end{bmatrix} \quad (\text{B.1.2})$$

The spherical harmonics coefficients can then be introduced in these partial derivatives. For instance, considering J2 effect, the expression of  $G(1,1)$  becomes [90]:

$$\frac{\partial a_x}{\partial x} = \frac{-\mu x}{r^3} \left[ 1 + \frac{3J_2 r_e^2}{2r^2} \left( 1 - \frac{5z^2}{r^2} \right) \right] \quad (\text{B.1.3})$$

These matrices in B.1.1 can easily be calculated since only the state vectors at times  $t_0$  and  $t$  are necessary to compute  $G$  and this latter state must be calculated during the data processing to evaluate the difference between the real measurements and the calculated ones from the observable model (i.e., to evaluate the observation deviation vector  $y$  of (2.3.4) ).

Furthermore, a practical approach feasible for short time spans would be propagating the state vector with a complete force model and compute the state transition matrix as in (B.1.1) from the gradient matrix of (B.1.2).

# Bibliography

- [1] International Space Exploration Coordination Group. *The Global Exploration Roadmap*. Jan. 2018. URL: [https://www.nasa.gov/sites/default/files/atoms/files/ger\\_2018\\_small\\_mobile.pdf](https://www.nasa.gov/sites/default/files/atoms/files/ger_2018_small_mobile.pdf) (cit. on pp. 1, 2).
- [2] Shuai Li, Paul G Lucey, Ralph E Milliken, Paul O Hayne, Elizabeth Fisher, Jean-Pierre Williams, Dana M Hurley, and Richard C Elphic. «Direct evidence of surface exposed water ice in the lunar polar regions». In: *Proceedings of the National Academy of Sciences* 115.36 (2018), pp. 8907–8912 (cit. on p. 1).
- [3] W C Feldman, S Maurice, AB Binder, BL Barraclough, RC Elphic, and DJ Lawrence. «Fluxes of fast and epithermal neutrons from Lunar Prospector: Evidence for water ice at the lunar poles». In: *Science* 281.5382 (1998), pp. 1496–1500 (cit. on p. 1).
- [4] Miriam Schonfeldt, Antoine Grenier, Anais DelEpaut, Pietro Giordano, Richard Swinden, and Javier Ventura-Traveset. «Across the Lunar Landscape: Towards a Dedicated Lunar PNT System». In: *Inside GNSS* (2020) (cit. on pp. 1, 6, 9, 26).
- [5] WT Huntress, VI Moroz, and IL Shevarev. «Lunar and planetary robotic exploration missions in the 20th century». In: *Space science reviews* 107.3 (2003), pp. 541–649 (cit. on p. 2).
- [6] BH Foing et al. «SMART-1 mission to the moon: Technology and science goals». In: *Advances in Space Research* 31.11 (2003), pp. 2323–2333 (cit. on p. 3).
- [7] Arup Roy Chowdhury et al. «Terrain mapping camera-2 onboard chandrayaan-2 orbiter». In: *Current Science* 118.4 (2020), p. 566 (cit. on p. 3).
- [8] Yuqi Qian, Long Xiao, James W Head, Carolyn H van der Bogert, Harald Hiesinger, and Lionel Wilson. «Young lunar mare basalts in the Chang’e-5 sample return region, northern Oceanus Procellarum». In: *Earth and Planetary Science Letters* 555 (2021), p. 116702 (cit. on p. 3).
- [9] Namrata Goswami. «India’s Space Program, Ambitions, and Activities». In: *Asia Policy* 27.2 (2020), pp. 43–49 (cit. on p. 3).

- [10] Elizabeth Gibney. «UAE ramps up space ambitions with Arab world’s first Moon mission». In: *Nature* 587.7833 (2020), pp. 186–187 (cit. on p. 3).
- [11] Cihan Ercan and İzzet Kale. «Historical space steps of Turkey: It is high time to establish the Turkish space agency». In: *Acta Astronautica* 130 (2017), pp. 67–74 (cit. on p. 3).
- [12] Rodrigo Leonardi and Adriana Elysa Alimandro Corrêa. «An Overview of Small Satellite Initiatives in Brazil». In: *Handbook of Small Satellites: Technology, Design, Manufacture, Applications, Economics and Regulation* (2020), pp. 1–14 (cit. on p. 4).
- [13] Spencer Kaplan. «Eyes on the Prize». In: *The Strategic Implications of Cislunar S* (2020) (cit. on p. 4).
- [14] Julie Michelle Klinger. *China, Africa, and the Rest: Recent Trends in Space Science, Technology, and Satellite Development*. Tech. rep. Working Paper, 2020 (cit. on p. 4).
- [15] NASA. *Past, present and future Moon Missions*. Dec. 2020. URL: <https://nssdc.gsfc.nasa.gov/planetary/planets/moonpage.html> (cit. on p. 4).
- [16] R Broucke. «Traveling between the Lagrange points and the Moon». In: *Journal of Guidance and Control* 2.4 (1979), pp. 257–263 (cit. on p. 4).
- [17] NASA. *The Artemis Plan*. Sept. 2020. URL: [https://www.nasa.gov/sites/default/files/atoms/files/artemis\\_plan-20200921.pdf](https://www.nasa.gov/sites/default/files/atoms/files/artemis_plan-20200921.pdf) (cit. on pp. 4–6).
- [18] ESA. *Lunar Satellites - ESA Moonlight*. Dec. 2020. URL: [https://www.esa.int/Applications/Telecommunications\\_Integrated\\_Applications/Lunar\\_satellites](https://www.esa.int/Applications/Telecommunications_Integrated_Applications/Lunar_satellites) (cit. on p. 6).
- [19] Anais Delepaut, Pietro Giordano, Javier Ventura-Traveset, Daniel Blonski, Miriam Schonfeldt, Philippe Schoonejans, Sarmad Aziz, and Roger Walker. «Use of GNSS for lunar missions and plans for lunar in-orbit development». In: *Advances in Space Research* 66.12 (2020), pp. 2739–2756 (cit. on pp. 7, 34).
- [20] Todd A Ely. «Stable constellations of frozen elliptical inclined lunar orbits». In: *the Journal of the Astronautical Sciences* 53.3 (2005), pp. 301–316 (cit. on pp. 8, 9, 87).
- [21] Todd A Ely and Erica Lieb. «Constellations of elliptical inclined lunar orbits providing polar and global coverage». In: *the Journal of the Astronautical Sciences* 54.1 (2006), pp. 53–67 (cit. on p. 8).
- [22] Tao Nie and Pini Gurfil. «Lunar frozen orbits revisited». In: *Celestial Mechanics and Dynamical Astronomy* 130.10 (2018), pp. 1–35 (cit. on p. 8).

- [23] Miriam Schonfeldt, Antoine Grenier, Anais Delepaut, Pietro Giordano, Richard Swinden, Javier Ventura-Traveset, Daniel Blonski, and Jorg Hahn. «A System Study about a Lunar Navigation Satellite Transmitter System». In: *2020 European Navigation Conference (ENC)*. IEEE. 2020, pp. 1–10 (cit. on p. 9).
- [24] Jerome R Vetter. «Fifty years of orbit determination». In: *Johns Hopkins APL technical digest 27.3* (2007), p. 239 (cit. on p. 11).
- [25] Bob Schutz, Byron Tapley, and George H Born. *Statistical orbit determination*. Elsevier, 2004 (cit. on pp. 11, 13–16, 19, 20, 22, 23, 39, 42, 103).
- [26] Oscar Sheynin. «Gauss and the Method of the Least Squares». In: *Journal of Economics and Statistics (Jahrbuecher fuer Nationaloekonomie und Statistik)* 219 (Sept. 1999), pp. 458–467. DOI: 10.15611/sps.2014.12.01 (cit. on p. 13).
- [27] International DORIS Service. *Doris tracking network: station management*. July 2019. URL: <https://ids-doris.org/doris-system/tracking-network/doris-station.html> (cit. on p. 13).
- [28] Oliver Montenbruck, Eberhard Gill, and Fh Lutze. «Satellite orbits: models, methods, and applications». In: *Appl. Mech. Rev.* 55.2 (2002), B27–B28 (cit. on pp. 14, 15, 19, 39).
- [29] PB Phung, VS Guedeney, and J Teles. «Tracking and Data Relay Satellite System (TDRSS) Range and Doppler Tracking System Observation Measurement and Modeling». In: *Goddard Space Flight Center, Greenbelt, Maryland, X-572-80-26* (1980) (cit. on p. 14).
- [30] NASA’s Goddard Space Flight Center. *Tracking and Data Relay Satellite (TDRS)*. Mar. 2019. URL: [https://www.nasa.gov/directorates/heo/scan/services/networks/tdrs\\_main](https://www.nasa.gov/directorates/heo/scan/services/networks/tdrs_main) (cit. on p. 14).
- [31] GPS.gov. *GPS Control Segment*. May 2017. URL: <https://www.gps.gov/systems/gps/control/> (cit. on p. 14).
- [32] Keric A Hill. «Autonomous navigation in libration point orbits». PhD thesis. University of Colorado at Boulder, 2007 (cit. on pp. 17, 22, 26, 36).
- [33] Ana Paula Marins Chiaradia, Helio Koiti Kuga, and Antonio Fernando Bertachini de Almeida Prado. «Comparison between two methods to calculate the transition matrix of orbit motion». In: *Mathematical Problems in Engineering* 2012 (2012) (cit. on pp. 17, 103, 104).
- [34] Gim J Der. «An elegant state transition matrix». In: *The Journal of the astronautical sciences* 45.4 (1997), pp. 371–390 (cit. on p. 17).
- [35] Stanley W Shepperd. «Universal Keplerian state transition matrix». In: *Celestial Mechanics* 35.2 (1985), pp. 129–144 (cit. on p. 17).

- [36] Mohinder S Grewal and Angus P Andrews. «Applications of Kalman filtering in aerospace 1960 to the present [historical perspectives]». In: *IEEE Control Systems Magazine* 30.3 (2010), pp. 69–78 (cit. on p. 18).
- [37] Peter S Maybeck. *Stochastic models, estimation, and control*. Academic press, 1982 (cit. on p. 18).
- [38] Arthur Gelb. *Applied optimal estimation*. MIT press, 1974 (cit. on p. 18).
- [39] Pablo Garcia, Diego Escobar, Alberto Agueda, and Francisco Martinez. «Covariance determination, propagation and interpolation techniques for space surveillance». In: *European Space Surveillance Conference, Madrid, Spain*. 2011 (cit. on p. 18).
- [40] Shashikala Achyut Gangal. «Simplified orbit determination algorithm for low earth orbit satellites using spaceborne gps navigation sensor». In: *Artificial Satellites* 49.2 (2014), pp. 81–99 (cit. on p. 18).
- [41] Xiucong Sun, Pei Chen, Christophe Macabiau, and Chao Han. «Autonomous orbit determination via Kalman filtering of gravity gradients». In: *IEEE Transactions on Aerospace and Electronic Systems* 52.5 (2016), pp. 2436–2451 (cit. on p. 18).
- [42] Quang Lam, Daniel Junker, David Anhalt, and David Vallado. «Analysis of an extended Kalman filter based orbit determination system». In: *AIAA Guidance, Navigation, and Control Conference*. 2010, p. 7600 (cit. on p. 18).
- [43] Catherine L Thornton and James S Border. *Radiometric tracking techniques for deep-space navigation*. John Wiley & Sons, 2003 (cit. on pp. 20, 21, 24, 39).
- [44] Erhu Wei, Xuechuan Li, Shuanggen Jin, and Jingnan Liu. «Effect of lunar gravity models on Chang’E-2 orbit determination using VLBI tracking data». In: *Geodesy and Geodynamics* 7.6 (2016), pp. 406–415 (cit. on p. 20).
- [45] Dmitry A Duev, G Molera Calvés, Sergei V Pogrebenko, Leonid I Gurvits, Giuseppe Cimo, and T Bocanegra Bahamon. «Spacecraft VLBI and Doppler tracking: algorithms and implementation». In: *Astronomy & Astrophysics* 541 (2012), A43 (cit. on p. 21).
- [46] Justin Kruger and Simone D’Amico. «Autonomous Angles-Only Multi-Target Tracking for Spacecraft Swarms». In: *arXiv preprint arXiv:2002.08881* (2020) (cit. on p. 22).
- [47] Joshua Sullivan and Simone D’Amico. «Nonlinear Kalman filtering for improved angles-only navigation using relative orbital elements». In: *Journal of Guidance, Control, and Dynamics* 40.9 (2017), pp. 2183–2200 (cit. on p. 22).

- [48] XU Jiuling, ZHANG Chaojie, WANG Chunhui, and JIN Xiaojun. «Approach to inter-satellite time synchronization for micro-satellite cluster». In: *Journal of Systems Engineering and Electronics* 29.4 (2018), pp. 805–815 (cit. on p. 23).
- [49] Gregory L Weaver, Mihran Miranian, and Jeffrey F Garstecki. «Composite USO/CSAC timekeeping system». In: *2012 IEEE Aerospace Conference*. IEEE, 2012, pp. 1–9 (cit. on p. 23).
- [50] Neil Ashby. «Relativistic effects in the global positioning system». In: *Journal of systems engineering and electronics* 6.4 (1995), pp. 199–237 (cit. on p. 23).
- [51] Tomasz Kur, Tomasz Liwosz, and Maciej Kalarus. «The application of inter-satellite links connectivity schemes in various satellite navigation systems for orbit and clock corrections determination: simulation study». In: *Acta Geodaetica et Geophysica* 56.1 (2021), pp. 1–28 (cit. on p. 23).
- [52] Yifei Lv, Tao Geng, Qile Zhao, Xin Xie, Feng Zhang, and Xing Wang. «Evaluation of BDS-3 Orbit Determination Strategies Using Ground-Tracking and Inter-Satellite Link Observation». In: *Remote Sensing* 12.16 (2020), p. 2647 (cit. on p. 23).
- [53] Daoning Yang, Jun Yang, Gang Li, Yifan Zhou, and ChengPan Tang. «Globalization highlight: orbit determination using BeiDou inter-satellite ranging measurements». In: *GPS Solutions* 21.3 (2017), pp. 1395–1404 (cit. on p. 23).
- [54] M. Y. Shin, C. Park, and S. J. Lee. «Atomic clock error modeling for GNSS software platform». In: *2008 IEEE/ION Position, Location and Navigation Symposium*. 2008, pp. 71–76. DOI: 10.1109/PLANS.2008.4570008 (cit. on p. 24).
- [55] Lauren Rose Chung. *Orbit determination methods for deep space drag-free controlled laser interferometry missions*. University of Maryland, College Park, 2006 (cit. on pp. 24, 41).
- [56] Mariano Vergara, Matteo Sgammini, Steffen Thoelet, Christoph Enneking, Yuji Zhu, and Felix Antreich. «Tracking error modeling in presence of satellite imperfections». In: *NAVIGATION, Journal of the Institute of Navigation* 63.1 (2016), pp. 3–13 (cit. on p. 24).
- [57] WL Sjogren, Donald W Trask, Charles J Vegos, and Wilbur R Wollenhaupt. «Physical constants as determined from radio tracking of the Ranger lunar probes». In: (1966) (cit. on p. 25).
- [58] W Wollenhaupt. «Apollo orbit determination and navigation». In: *8th Aerospace Sciences Meeting*. 1970, p. 27 (cit. on p. 25).

- [59] Erwan Mazarico, Gregory A Neumann, Michael K Barker, Sander Goossens, David E Smith, and Maria T Zuber. «Orbit determination of the Lunar Reconnaissance Orbiter: Status after seven years». In: *Planetary and space science* 162 (2018), pp. 2–19 (cit. on pp. 26, 49).
- [60] Jonathon Smith, Theodore Drain, Shyam Bhaskaran, and Tomas Martin-Mur. «Monte for Orbit Determination». In: (2017) (cit. on p. 26).
- [61] Tung-Han You et al. «Gravity Recovery and Interior Laboratory Mission (GRAIL) Orbit Determination». In: (2012) (cit. on p. 26).
- [62] Young-Rok Kim, Young-Joo Song, Jae-ik Park, Donghun Lee, Jonghee Bae, SeungBum Hong, Dae-Kwan Kim, and Sang-Ryool Lee. «Ground Tracking Support Condition Effect on Orbit Determination for Korea Pathfinder Lunar Orbiter (KPLLO) in Lunar Orbit». In: *Journal of Astronomy and Space Sciences* 37.4 (2020), pp. 237–247 (cit. on pp. 26, 32).
- [63] Jia Wang et al. «Localization of the Chang’e-5 Lander Using Radio-Tracking and Image-Based Methods». In: *Remote Sensing* 13.4 (2021), p. 590 (cit. on p. 26).
- [64] Shanhong Liu, Jianguo Yan, Jianfeng Cao, Mao Ye, Xie Li, Fei Li, and Jean-Pierre Barriot. «Review of the precise orbit determination for Chinese lunar exploration projects». In: *Earth and Space Science* 8.4 (2021), e2020EA001361 (cit. on p. 26).
- [65] Bradley Cheetham. «Cislunar Autonomous Positioning System Technology Operations and Navigation Experiment (CAPSTONE)». In: *ASCEND 2020*. 2020, p. 4140 (cit. on p. 26).
- [66] BW Cheetham. «Development of Mission Enabling Infrastructure—Cislunar Autonomous Positioning System (CAPS)». In: *2017 Annual Meeting of the Lunar Exploration Analysis Group*. Vol. 2041. 2017, p. 5064 (cit. on p. 26).
- [67] Siamak G Hesar, Jeffrey S Parker, Jason M Leonard, Ryan M McGranaghan, and George H Born. «Lunar far side surface navigation using linked autonomous interplanetary satellite orbit navigation (LiAISON)». In: *Acta Astronautica* 117 (2015), pp. 116–129 (cit. on p. 26).
- [68] Brent Allen Archinal et al. «Report of the IAU working group on cartographic coordinates and rotational elements: 2009». In: *Celestial Mechanics and Dynamical Astronomy* 109.2 (2011), pp. 101–135 (cit. on p. 28).
- [69] AGI. *Technical Notes for Central Bodies - Configuration Settings, Shapes, Ephemerides, and Coordinate Systems (Reference Frames)*. Sept. 2016. URL: <https://help.agi.com/stk/11.0.1/Content/stk/AstroComps.htm#moonInertial> (cit. on p. 28).

- [70] Angel Rocha. «Numerical Methods and Tolerance Analysis for Orbit Propagation». PhD thesis. San José State University, 2018 (cit. on p. 30).
- [71] Bradley J Clement and Mark D Johnston. «The deep space network scheduling problem». In: (2005) (cit. on p. 32).
- [72] William A Mahoney, Susan Comeau, Lisa J Garcia, Douglas B McElroy, David S Mittman, JoAnn C O’Linger, and Steven R Tyler. «Spitzer Scheduling Challenges: cold and warm». In: *Observatory Operations: Strategies, Processes, and Systems II*. Vol. 7016. International Society for Optics and Photonics. 2008, 70161W (cit. on p. 32).
- [73] Mark Woodard, Daniel Cosgrove, Patrick Morinelli, Jeff Marchese, Brandon Owens, and David Folta. «Orbit determination of spacecraft in Earth-Moon L1 and L2 libration point orbits». In: (2011) (cit. on p. 32).
- [74] Stuart Demcak, Brian Young, Try Lam, Nikolas Trawny, Clifford Lee, Rodney Anderson, Stephen Broschart, et al. «Navigation challenges in the MAVEN science phase». In: (2012) (cit. on p. 32).
- [75] Mark D Johnston, Daniel Tran, Belinda Arroyo, Sugi Sorensen, Peter Tay, Butch Carruth, Adam Coffman, and Mike Wallace. «Automated scheduling for NASA’s deep space network». In: *AI Magazine* 35.4 (2014), pp. 7–25 (cit. on p. 32).
- [76] M A Sharaf, Z M Hayman, and M E Awad. «Satellite to satellite visibility». In: *The Open Astronomy Journal* 5.1 (2012) (cit. on p. 32).
- [77] Chao Han, XiaoJie Gao, and XiuCong Sun. «Rapid satellite-to-site visibility determination based on self-adaptive interpolation technique». In: *Science China Technological Sciences* 60.2 (2017), pp. 264–270 (cit. on p. 33).
- [78] Jennifer E Donaldson, Joel JK Parker, Michael C Moreau, Dolan E Highsmith, and Philip D Martzen. «Characterization of on-orbit GPS transmit antenna patterns for space users». In: *NAVIGATION, Journal of the Institute of Navigation* 67.2 (2020), pp. 411–438 (cit. on p. 34).
- [79] United Nation Office for Outer Space Affairs. *The Interoperable Global Navigation Satellite Systems Space Volume*. June 2018. URL: [https://www.unoosa.org/res/oosadoc/data/documents/2018/stspace/stspace75\\_0\\_html/st\\_space\\_75E.pdf](https://www.unoosa.org/res/oosadoc/data/documents/2018/stspace/stspace75_0_html/st_space_75E.pdf) (cit. on p. 34).
- [80] Ashish Sharma, Gaurav Ghodke, and Murugesh TS Prabhu. «Monitoring volume fluctuations of Indian reservoirs from space». In: *International Journal of Geomatics and Geosciences* 4.2 (2013), p. 342 (cit. on p. 35).

- [81] Herwig Zech, Philipp Biller, Frank Heine, and Matthias Motzigemba. «Optical intersatellite links for navigation constellations». In: *International Conference on Space Optics—ICSO 2018*. Vol. 11180. International Society for Optics and Photonics. 2019, 111800Z (cit. on p. 35).
- [82] MathWorks. *Randn-Normally distributed random numbers*. Jan. 2021. URL: <https://it.mathworks.com/help/matlab/ref/randn.html> (cit. on p. 38).
- [83] David A Vallado. *Fundamentals of astrodynamics and applications*. Vol. 12. Springer Science & Business Media, 2001 (cit. on p. 40).
- [84] European Union Agency for Space Programme. *Galileo - Open Service - Service Definition Document*. May 2019. URL: [https://www.gsc-europa.eu/sites/default/files/sites/all/files/Galileo-OS-SDD\\_v1.1.pdf](https://www.gsc-europa.eu/sites/default/files/sites/all/files/Galileo-OS-SDD_v1.1.pdf) (cit. on pp. 43, 95).
- [85] Umberto Robustelli, Guido Benassai, and Giovanni Pugliano. «Signal in space error and ephemeris validity time evaluation of milena and doresa galileo satellites». In: *Sensors* 19.8 (2019), p. 1786 (cit. on p. 43).
- [86] Craig C Douglas, Long Lee, and Man-Chung Yeung. «On solving ill conditioned linear systems». In: *Procedia Computer Science* 80 (2016), pp. 941–950 (cit. on p. 56).
- [87] Bofeng Li, Yunzhong Shen, and Yanming Feng. «Fast GNSS ambiguity resolution as an ill-posed problem». In: *Journal of geodesy* 84.11 (2010), pp. 683–698 (cit. on p. 56).
- [88] Xingsheng Deng, Liangbo Yin, Sichun Peng, and Meiqing Ding. «An iterative algorithm for solving ill-conditioned linear least squares problems». In: *Geodesy and Geodynamics* 6.6 (2015), pp. 453–459 (cit. on pp. 56, 58).
- [89] Erik F Kaasschieter. «Preconditioned conjugate gradients for solving singular systems». In: *Journal of Computational and Applied mathematics* 24.1-2 (1988), pp. 265–275 (cit. on p. 58).
- [90] HK Kuga. «Adaptive orbit estimation applied to low altitude satellites». In: *Masters Thesis* (1982), p. 7 (cit. on p. 104).